REVIEWS OF MODERN PHYSICS, VOLUME 74, APRIL 2002

Modern optical astronomy: technology and impact of interferometry

Swapan K. Saha

Indian Institute of Astrophysics, Koramangala, Bangalore 560 034, India

(Published 22 May 2002)

The present "state of the art" and the path to future progress in high-spatial-resolution imaging interferometry is reviewed. The review begins with a treatment of the fundamentals of stellar optical interferometry, the origin, properties, and optical effects of turbulence in the Earth's atmosphere, the passive methods such as speckle interferometry that are applied on a single telescope to overcome atmospheric image degradation, and various other techniques. These topics include differential speckle interferometry, speckle spectroscopy and polarimetry, phase diversity, wave-front shearing interferometry, phase-closure methods, dark speckle imaging, as well as the limitations imposed by the detectors on the performance of speckle imaging. A brief account is given of the technological innovation of adaptive optics to compensate for atmospheric effects on the image in real time. A major advancement involves the transition from single-aperture to dilute-aperture interferometry using multiple telescopes. Therefore the review deals with recent developments involving ground-based and space-based optical arrays. Emphasis is placed on the problems specific to delay lines, beam recombination, polarization, dispersion, fringe tracking, bootstrapping, coherencing and cophasing, and recovery of the visibility functions. The role of adaptive optics in enhancing visibilities is also discussed. The applications of interferometry, such as imaging, astrometry, and nulling, are described. The mathematical intricacies of the various "postdetection" image-processing techniques are examined critically. The review concludes with a discussion of the astrophysical importance and the prospects of interferometry.

CONTENTS

I. INTRODUCTION

Optical interferometry provides physicists and astronomers with an exquisite set of probes of the microcosmos and macrocosmos. From the laboratory to the observatory over the past few decades, there has been a surge of activity in developing new tools for ground-based optical astronomy, of which interferometry is one of the most powerful.

An optical interferometer is a device that combines two or more light waves emitted from the same source at the same time to produce interference fringes. The implementation of interferometry in optical astronomy began more than a century ago with the work of Fizeau (1868). Michelson and Pease (1921) successfully measured the angular diameter of Alpha Orionis (α Ori) using an interferometer based on two flat mirrors, which allowed them to measure the fringe visibility in the interference pattern formed by starlight at the detector plane. However, progress was hindered by the severe image degradation produced by atmospheric turbulence in the optical spectrum. The field remained dormant until the development of intensity interferometry by Hanbury Brown and Twiss (1958), a technique that employs two adjacent sets of mirrors and photoelectric correlation.

Turbulence and the concomitant development of thermal convection in the atmosphere distort the phase and amplitude of an incoming wave front of starlight. The longer the path, the greater the degradation that the image suffers. Light reaching the entrance pupil of an imaging system is coherent only within patches of diameters of order r_0, Fried's parameter (Fried, 1966). This limited coherence causes blurring of the image, which is modeled by a convolution with the point-spread function. Both the sharpness of astronomical images and the signal-to-noise (S/N) ratio (hence the faintness of the objects that can be studied) depend on angular resolution, the latter because noise comes from as much of the sky as is in the resolution element. Thus reducing the beamwidth from, say, 1 to 0.5 arcsec reduces sky noise by a factor of 4. Two physical phenomena limit the minimum resolvable angle at optical and infrared (IR) wavelengths—the diameter of the collecting area and turbulence in the atmosphere. The crossover between domination by aperture size (λ/aperture diameter) and domination by atmospheric turbulence ("seeing") occurs when the aperture becomes larger than the size of a characteristic turbulent element.

The image of a star obtained through a large telescope looks "speckled" or grainy because different parts of the image are blurred by small areas of turbulence in the Earth's atmosphere. Labeyrie (1970) proposed *speckle interferometry* (SI), a process that deciphers the diffraction-limited Fourier spectrum and image features of stellar objects by taking a large number of very-short-exposure images of the same field. Computer assistance is then used to reconstruct from these many images a single image that is free of turbulent areas—in essence, an image of the object as it might appear from space.

The success of speckle interferometry in measuring the diameters of stars encouraged astronomers to develop further image-processing techniques. These techniques are, for the most part, postdetection processes. Recent advances in technology have produced the hardware to compensate for wave-front distortion in real time. *Adaptive optics* (AO; Babcock, 1953; Rousset *et al.*, 1990) is based on this hardware-oriented approach, which sharpens telescope images blurred by the Earth's atmosphere. It employs a combination of deformation of reflecting surfaces (i.e., flexible mirrors) and postdetection image restoration (Roddier, 1999). One of its most successful applications has been in the imaging of Neptune's ring arcs. Adaptive optics imaging systems have been treated in depth in the review of Roggemann *et al.* (1997), which includes a discussion of wave-front compensation devices, wave-front sensors, control systems, the performance of AO systems, and representative experimental results. It also deals with the characterization of atmospheric turbulence, the SI technique, and deconvolution techniques for wave-front sensing.

Long-baseline optical interferometry uses two or more optical telescopes to synthesize the angular resolution of a much larger aperture (aperture synthesis) than would be possible with a single telescope. Labeyrie (1975) extended the concept of speckle interferometry to a pair of telescopes in a north-south baseline configuration, and subsequently astronomers have created larger ground-based arrays. A few of these arrays, e.g., the Keck Interferometer and the Very Large Telescope Interferometer (VLTI), employ large telescopes fitted with AO systems.

The combination of long-baseline interferometry, mimicking a wide aperture, and AO techniques to improve the images offers the best of both approaches and shows great promise for applications such as the search for extrasolar planets. At this point it seems clear that interferometry and AO are complementary, and neither can reach its full potential without the other.

The present review addresses the aims, methods, scientific achievements, and future prospects of long-baseline interferometry at optical and infrared wavelengths, carried out with two or more apertures separated by distances greater than their own sizes. In order to embark on such a subject, we first review the basic principles of interferometry and its applications, the theoretical aspects of SI as a statistical analysis of a speckle pattern, and the limitations imposed by the atmosphere and the detectors on the performance of single-aperture diffraction-limited imaging. Other related concerns, such as the relationship between image-plane techniques and pupil-plane interferometry, phase-closure methods, and dark speckle imaging, will also be treated. Adaptive optics as a predetection compensation technique is described in brief, as are the strengths and weaknesses of predetection and postdetection.

The final part of this review deals with the applications of multiple-telescope interferometry in imaging, astrometry, and nulling. These applications entail specific problems having to do with delay lines, beam recombination, polarization, dispersion, fringe tracking, and the recovery of visibility functions. Various image restoration techniques are discussed as well, with emphasis on the deconvolution methods used in aperture-synthesis mapping.

II. BASIC PRINCIPLES

Astronomical sources emit incoherent light consisting of the random superposition of numerous successive short-lived waves sent out from many elementary emitters, and therefore the optical coherence is related to the various forms of correlations of the random process. For a monochromatic wave field, the amplitude of vibration at any point is constant and the phase varies linearly with time. Conversely, the amplitude and phase in the case of a quasimonochromatic wave field undergo irregular fluctuations (Born and Wolf, 1984). The rapidity of fluctuations depends on the light crossing time of the emitting region. Interferometers based on wave-front division (Young's experiment, which is sensitive to the size and bandwidth of the source), are generally used to measure spatial coherence, while interferometers based on amplitude division (Michelson's interferometer) are used to measure temporal coherence. In what follows, some of the fundamental mathematical steps pertinent to interferometry are illustrated.

A. Mathematical framework

A monochromatic plane wave $V(\mathbf{r},t)$ at a point $\mathbf{r}$ is expressed as

$$V(\mathbf{r},t)=\mathrm{Re}\{a(\mathbf{r})e^{-i[2\pi\nu_0 t-\psi_j(\mathbf{r})]}\}. \tag{1}$$

Here Re means the "real part of"; $\mathbf{r}$ is the position vector of a point (x,y,z); $a(\mathbf{r})$ is the amplitude of the wave; t is the time; ν_0, the frequency of the wave; and $\psi_j(\mathbf{r})$ are the phase functions of the form $\mathbf{k}\cdot\mathbf{r}-\delta_j$, in which $\mathbf{k}$ is the propagation vector and δ_j are the phase constants that specify the state of polarization. When the complex vector function of position is denoted by $\Psi(\mathbf{r})=a(\mathbf{r})e^{i\psi_j(\mathbf{r})}$, the complex representation of the analytic signal, $\mathcal{U}(\mathbf{r},t)$, associated with $V(\mathbf{r},t)$ becomes

$$\mathcal{U}(\mathbf{r},t)=a(\mathbf{r})e^{-i[2\pi\nu_0 t-\psi_j(\mathbf{r})]} \tag{2}$$

$$=\Psi(\mathbf{r})e^{-i2\pi\nu_0 t}. \tag{3}$$

This complex representation is preferred for linear time-invariant systems, because the eigenfunctions of such systems are of the form $e^{-i\omega_0 t}$, where $\omega_0=2\pi\nu_0$ is the angular frequency. From Eqs. (1) and (2), the relationship translates into

$$V(\mathbf{r},t)=\mathrm{Re}\{\Psi(\mathbf{r})e^{-i\omega_0 t}\}$$

$$=\frac{1}{2}[\Psi(\mathbf{r})e^{-i\omega_0 t}+\Psi^*(\mathbf{r})e^{i\omega_0 t}]. \tag{4}$$

The intensity of light is defined as the time average of the amount of energy; therefore, when the latter is taken over an interval much greater than the period ($\mathsf{T}_0=2\pi/\omega_0$), the intensity $\mathcal{I}$ at the same point is calculated as

$$\mathcal{I}\propto\langle V^2\rangle=\frac{1}{2}\Psi\Psi^*, \tag{5}$$

where $\langle\ \rangle$ stands for the ensemble average of the quantity within the brackets and Ψ^* represents the complex conjugate of Ψ.

Since the complex amplitude is a constant phasor in the monochromatic case, the Fourier transform of the complex representation of the signal, $\mathcal{U}(\mathbf{r},t)$, is given by

$$\hat{\mathcal{U}}(\mathbf{r},\nu)=a(\mathbf{r})e^{i\psi}\delta(\nu-\nu_0). \tag{6}$$

It is equal to twice the positive part of the instantaneous spectrum $\hat{V}(\mathbf{r},\nu)$. In the polychromatic case, the complex amplitude becomes

$$\mathcal{U}(\mathbf{r},t)=2\int_0^\infty \hat{V}(\mathbf{r},\nu)e^{-i2\pi\nu t}d\nu. \tag{7}$$

The disturbance produced by a real physical source is calculated by the integration of the monochromatic signals over an optical bandpass. In the case of a quasimonochromatic approximation (if the width of the spectrum $\Delta\nu$ is much less than ν_0), the expression is modified to

$$\mathcal{U}(\mathbf{r},t)=|\Psi(\mathbf{r},t)|e^{i[\psi(t)-2\pi\nu_0 t]}, \tag{8}$$

where the field is characterized by the complex amplitude $\Psi(\mathbf{r},t)$, i.e.,

$$\Psi(\mathbf{r},t)=|\Psi(\mathbf{r},t)|e^{i\psi(t)}. \tag{9}$$

This phasor is time dependent, although it varies slowly with respect to $e^{-i2\pi\nu_0 t}$.

The complex amplitude $\Psi(\boldsymbol{\alpha})$ diffracted at angle $\boldsymbol{\alpha}$ in the telescope's focal plane is given by

$$\Psi(\boldsymbol{\alpha}) \propto \int \mathcal{P}_0(\mathbf{x})\Psi_0(\mathbf{x})e^{-i2\pi\boldsymbol{\alpha}\cdot\mathbf{x}/\lambda}d\mathbf{x}, \tag{10}$$

where $\boldsymbol{\alpha}=(\mathbf{x}/f)$ is a two-dimensional (2D) space vector, f is the focal length, $\Psi_0(\mathbf{x})$ is the complex amplitude at the telescope aperture, and $\mathcal{P}_0(\mathbf{x})$ is the pupil transmission function of the telescope aperture. For an ideal telescope, we have $\mathcal{P}_0(\mathbf{x})=1$ inside the aperture and $\mathcal{P}_0(\mathbf{x})=0$ outside the aperture. In the space-invariant case,

$$\Psi(\boldsymbol{\alpha}) \propto \int \mathcal{P}(\mathbf{u})\Psi(\mathbf{u})e^{-i2\pi\boldsymbol{\alpha}\mathbf{u}}d\mathbf{u}, \tag{11}$$

$$= \mathcal{F}[\Psi(\mathbf{u})\cdot\mathcal{P}(\mathbf{u})], \tag{12}$$

where $\mathcal{F}$ represents the complex Fourier transform and the dimensionless variable $\mathbf{u}$ is equal to $\mathbf{x}/\lambda$; hence $\Psi(\mathbf{u})$ can be replaced by $\Psi_0(\lambda\mathbf{u})$ and $\mathcal{P}(\mathbf{u})$ by $\mathcal{P}_0(\lambda\mathbf{u})$. The irradiance diffracted in the direction $\boldsymbol{\alpha}$ is the point-spread function of the telescope and the atmosphere and its Fourier transform $\hat{\mathcal{S}}(\mathbf{f})$ is the *optical transfer function*:

$$\hat{\mathcal{S}}(\mathbf{f}) = \int \mathcal{S}(\boldsymbol{\alpha})e^{[-2i\pi\boldsymbol{\alpha}\cdot\mathbf{f}]}d\boldsymbol{\alpha}, \tag{13}$$

where $\mathbf{f}$ is the spatial frequency expressed in rad^{-1} and $|\hat{\mathcal{S}}(\mathbf{f})|$ is the *modulation transfer function*.

1. Convolution

The convolution of two functions describes phenomena such as blurring of a photograph that may be caused by various reasons, e.g., poor focus or motion of the photographer during the exposure. In such a blurred picture each point of the object is replaced by a spread function. For a 2D incoherent source, the complex amplitude in the image plane is the convolution of the complex amplitude of the pupil plane and the pupil transmission function,

$$\mathcal{S}(\boldsymbol{\alpha}) = \mathcal{P}(\boldsymbol{\alpha}) \star \Psi(\boldsymbol{\alpha}). \tag{14}$$

In the Fourier plane, the effect of the convolution becomes a point-by-point multiplication of the optical transfer function of the pupil, $\mathcal{P}(\mathbf{u})$, with the transform of the object $\Psi(\mathbf{u})$, i.e.,

$$\hat{\mathcal{S}}(\mathbf{f}) = \mathcal{P}(\mathbf{u})\cdot\Psi(\mathbf{u}). \tag{15}$$

The illumination at the focal plane of the telescope observed as a function of image plane is

$$\mathcal{S}(\boldsymbol{\alpha}) = \langle \Psi(\boldsymbol{\alpha},t)\Psi^*(\boldsymbol{\alpha},t)\rangle \tag{16}$$

$$\propto |\mathcal{F}[\Psi(\mathbf{u})\cdot\Psi^*(\mathbf{u})]|^2. \tag{17}$$

The autocorrelation of this function is expressed as

$$\mathcal{F}[\mathcal{S}(\boldsymbol{\alpha})\otimes\mathcal{S}(\boldsymbol{\alpha})] = \hat{\mathcal{S}}(\mathbf{f})\hat{\mathcal{S}}^*(\mathbf{f}) = |\hat{\mathcal{S}}(\mathbf{f})|^2, \tag{18}$$

where $\otimes$ stands for correlation.

2. Resolution

In ideal conditions, the resolution $\mathcal{R}$ that can be achieved in an imaging experiment is limited only by the imperfections in the optical system, and according to Strehl's criterion, the resolving power $\mathcal{R}$ of any telescope of diameter D is given by the integral of its transfer function,

$$\mathcal{R} = \int \hat{\mathcal{S}}(\mathbf{u})d\mathbf{u}. \tag{19}$$

Therefore $\mathcal{R}=\mathcal{S}(\mathbf{0})$. The *Strehl ratio* $\mathcal{S}_r$ is defined as the ratio of the intensity at the centroid of the observed point-spread function, $\mathcal{S}(\mathbf{0})$, to the intensity of the peak of the diffraction-limited image or "Airy spike," $\mathcal{S}(\mathbf{0})_{\mathcal{A}s}$, i.e.,

$$\mathcal{S}_r = \frac{\mathcal{S}(\mathbf{0})}{\mathcal{S}(\mathbf{0})_{\mathcal{A}s}} \approx e^{-k^2\sigma_{OPD}^2}, \tag{20}$$

where $k=2\pi/\lambda$ is the wave number and σ_{OPD} the rms *optical path difference* (OPD) error. Typical ground-based observations with large telescopes in the visible wavelength range are made with a Strehl ratio $\leqslant 0.01$ (Babcock, 1990), while a diffraction-limited telescope would by definition have a Strehl ratio of 1.

B. Principles of interference and its applications

When two light beams from a single source are superposed, the intensity at the place of superposition varies from point to point between maxima, which exceed the sum of the intensities in the beams, and minima, which may be zero. This sum or difference is known as interference; the correlated fluctuation can be partially or completely coherent (Born and Wolf, 1984).

Let the two monochromatic waves $V_1(\mathbf{r},t)$ and $V_2(\mathbf{r},t)$ be superposed at the recombination point. The correlator sums the instantaneous amplitudes of the fields. The total field at the output is

$$V = V_1 + V_2, \tag{21}$$

$$V^2 = V_1^2 + V_2^2 + 2V_1\cdot V_2. \tag{22}$$

Then if Ψ_1 and Ψ_2 are the complex amplitudes of the two waves with the corresponding phases ψ_1 and ψ_2, these two waves are propagating in the z direction and linearly polarized with an electric-field vector in the x direction. (A general radiation field is generally described by four Stokes parameters, I, Q, U, and V, which specify intensity, degree of polarization, plane of polarization, and ellipticity of the radiation at each point and in any given direction, respectively). Therefore the total intensity [see Eq. (4)], at the same point can be determined as

$$\mathcal{I} = \mathcal{I}_1 + \mathcal{I}_2 + \mathcal{J}_{12} = \mathcal{I}_1 + \mathcal{I}_2 + \frac{1}{2}(\Psi_1\Psi_2^* + \Psi_1^*\Psi_2)$$

$$= \mathcal{I}_1 + \mathcal{I}_2 + 2\sqrt{\mathcal{I}_1\mathcal{I}_2}\cos\delta, \tag{23}$$

where $\mathcal{I}_1=\langle V_1^2\rangle$ and $\mathcal{I}_2=\langle V_2^2\rangle$ are the intensities of the two terms, and $\mathcal{J}_{12}=2\langle V_1\cdot V_2\rangle=2\sqrt{\mathcal{I}_1\mathcal{I}_2}$ is the interference term, which depends on the amplitude components as well as on the phase difference between the two waves, $\delta=2\pi\Delta\varphi/\lambda_0$. Here $\Delta\varphi$ is the OPD between the two waves from the common source to the intersecting point, and λ_0 is the wavelength in vacuum. In general, two light beams are not correlated, but the correlation term $\Psi_1\Psi_2^*$ takes on significant values for a short period of time and $\langle\Psi_1\Psi_2^*\rangle=0$. Time variations of $\Psi(\mathbf{r})$ are statistical in nature (Mendel and Wolf, 1995). Hence one seeks a statistical description of the field (correlations), as the field is due to a partially coherent source. Depending upon the correlations between the phasor amplitudes at different object points, one would expect a definite correlation between the two points of the field emitted by the object. The maximum intensity occurs when $|\delta|=0,2\pi,4\pi$ and the minimum when $|\delta|=\pi,3\pi,5\pi$. If $\mathcal{I}_1=\mathcal{I}_2=\mathcal{I}$, the intensity varies between $4\mathcal{I}$ and 0.

In the case of a quasimonochromatic wave, the analytical signal $\mathcal{U}(t)$ obtained at the observation point is expressed as

$$\mathcal{U}(t)=K_1\mathcal{U}(r_1,t-\tau_1)+K_2\mathcal{U}(r_2,t-\tau_2), \tag{24}$$

where K_j are constants and r_j are the positions of two pinholes in the wave field. The times τ_j are the transit times from the pinholes to the intersection point, $\tau_j=s_j/c$.

If the pinholes are small and the diffracted fields are considered to be uniform, the values $|K_j|$ satisfy $K_1^*K_2=K_1K_2^*=K_1K_2$. Noting that $\mathcal{I}_j=|K_j|^2\langle|\mathcal{U}(r_j,t-\tau_j)|^2\rangle$, we therefore find the intensity at the output to be

$$\mathcal{I}=\mathcal{I}_1+\mathcal{I}_2+2K_1K_2\,\mathrm{Re}\left[\mathbf{\Gamma}_{12}\left(\frac{s_2-s_1}{c}\right)\right]. \tag{25}$$

where $s_i=\tau_i/c$. The Van Cittert–Zernike theorem states that the modulus of the complex degree of coherence (which describes the correlation of vibrations at a fixed point and a variable point) in a plane illuminated by an incoherent quasimonochromatic source is equal to the modulus of the normalized spatial Fourier transform of its brightness distribution (Born and Wolf, 1984; Mendel and Wolf, 1995). The observed image is the Fourier transform of the mutual coherence function or the correlation function. The complex degree of (mutual) coherence, $\boldsymbol{\gamma}_{12}(\tau)$, of the observed source is defined as

$$\boldsymbol{\gamma}_{12}(\tau)=\frac{\mathbf{\Gamma}_{12}(\tau)}{\sqrt{\mathbf{\Gamma}_{11}(0)\mathbf{\Gamma}_{22}(0)}}=\frac{\mathbf{\Gamma}_{12}(\tau)}{\sqrt{\mathcal{I}_1\mathcal{I}_2}}, \tag{26}$$

where $\mathcal{I}_1=K_1^2\mathbf{\Gamma}_{11}(0)$ and $\mathcal{I}_2=K_2^2\mathbf{\Gamma}_{22}(0)$. The function $\mathbf{\Gamma}_{ij}(\tau)=\langle\mathcal{U}(r_i,t+\tau)\mathcal{U}^*(r_j,t)\rangle$ is measured at two points. At a point where both the points coincide, the self-coherence $\mathbf{\Gamma}_{11}(\tau)=\langle\mathcal{U}(r_1,t+\tau)\mathcal{U}^*(r_1,t)\rangle$ reduces to ordinary intensity. When $\tau=0,\mathbf{\Gamma}_{11}(0)=\mathcal{I}_1;\ \mathbf{\Gamma}_{22}(0)=\mathcal{I}_2$. The ensemble average can be replaced by a time average due to the assumed ergodicity (a random process that is strictly stationary) of the fields. If both the fields are directed on a quadratic detector, it yields the desired cross term (time average due to the finite time response). The measured intensity at the detector would be

$$\mathcal{I}=\mathcal{I}_1+\mathcal{I}_2+2\sqrt{\mathcal{I}_1\cdot\mathcal{I}_2}\,\mathrm{Re}\left[\boldsymbol{\gamma}_{12}\left(\frac{s_2-s_1}{c}\right)\right]. \tag{27}$$

In order to keep the time correlation close to unity, the delay τ must be limited to a small fraction of the temporal width or coherence time, $\tau_c=1/\Delta\nu$; here $\Delta\nu$ is the spectral width. The relative coherence of the two beams diminishes as the difference in path length increases, culminating in a drop in the visibility (a dimensionless number between zero and one that indicates the extent to which a source is resolved on the baseline being used) of the fringes. For $\tau\ll\tau_c$, the function $\boldsymbol{\gamma}_{12}(\tau)$ can be approximated as $\boldsymbol{\gamma}_{12}(0)e^{-2\pi i\nu_0\tau}$. The exponential term is nearly constant, and $\boldsymbol{\gamma}_{12}(0)$ measures the spatial coherence. Let ψ_{12} be the argument of $\boldsymbol{\gamma}_{12}(\tau)$; then

$$\mathcal{I}=\mathcal{I}_1+\mathcal{I}_2+2\sqrt{\mathcal{I}_1,\mathcal{I}_2}\,\mathrm{Re}[|\boldsymbol{\gamma}_{12}(0)|e^{i(\psi_{12}-2\pi\nu_0\tau)}]. \tag{28}$$

The measured intensity at a distance x from the origin (point at zero OPD) on a screen at a distance z from the apertures is

$$\mathcal{I}(x)=\mathcal{I}_1+\mathcal{I}_2+2\sqrt{\mathcal{I}_1,\mathcal{I}_2}|\boldsymbol{\gamma}_{12}(0)|\cos\left\{\frac{2\pi d(x)}{\lambda}-\psi_{12}\right\}, \tag{29}$$

where $d(x)=bx/z$ is the OPD corresponding to x, and b is the distance between the two apertures.

The modulus of the fringe visibility is estimated as the ratio of high-frequency to low-frequency energy in the average spectral density; the visibility of fringes, $\mathcal{V}$, is estimated to be

$$\mathcal{V}=\frac{\mathcal{I}_{\max}-\mathcal{I}_{\min}}{\mathcal{I}_{\max}+\mathcal{I}_{\min}}=|\boldsymbol{\gamma}_{12}(0)|\frac{2\sqrt{\mathcal{I}_1\mathcal{I}_2}}{\mathcal{I}_1+\mathcal{I}_2}. \tag{30}$$

1. Fizeau interferometer

Fizeau (1868) suggested that installing a screen with two holes in front of a telescope would allow measurements of stellar diameters with diffraction-limited resolution. In this setup, the beams are diffracted by the subapertures and the telescope acts as both collector and correlator. Therefore temporal coherence is automatically obtained due to the built-in zero OPD. The spatial modulation frequency, as well as the required sampling of the image, changes with the separation of subapertures. The maximum resolution in this case depends on the separation between the subapertures; the maximum number of spacings that can be explored is limited by the physical diameter of the telescope. The number of stellar sources for measuring diameters is also limited. One of the first significant results was the measurement of the diameter of the satellites of Jupiter with a Fizeau interferometer on the 40-in. Yerkes refractor by Michelson (1891). With the 100-in. telescope on Mt. Wilson, Anderson (1920) determined the angular separation (ρ) of the spectroscopic binary star Capella.

2. Michelson interferometer

Results from the classical Michelson interferometer were used to formulate special relativity. They are also being used in gravity-wave detection. Gravitational radiation produced by coalescing binaries or exploding stars, for example, changes the metric of spacetime. This effect causes a differential change in the path length of the arms of the interferometer, thereby introducing a phase shift. Today, several ground-based long-baseline laser-interferometric detectors based on this principle are under construction, and within the next several years these detectors should be in operation (Robertson, 2000). The proposed Laser Interferometer Space Antenna, consisting of three satellites in formation about 50 million kilometers above the Earth in a heliocentric orbit, may detect gravitational waves by measuring fluctuations in the distances between test masses carried by the satellites.

The essence of Michelson's stellar interferometer was to determine the covariance $\langle \Psi_1 \Psi_2 \rangle$ of the complex amplitudes Ψ_1, Ψ_2 at two different points of the wave fronts. This interferometer was equipped with four flat mirrors that folded the beams by installing a 7-m steel beam on top of the Mt. Wilson 100-in. telescope. Michelson and Pease (1921) resolved the supergiant α Ori and a few other stars. In this case, the spatial modulation frequency in the focal plane was independent of the distance between the collectors. In the Fizeau mode, the ratio of aperture diameter to separation is constant from light collection to recombination in the image plane (homothetic pupil). In the Michelson mode, this ratio is not constant since the collimated beams have the same diameter from the output of the telescope to the recombination lens. The distance between pupils is equal to the baseline at the collection mirrors (the resolution is limited by the baseline) and to a much smaller value just before the recombination lens. The disadvantage of the Michelson mode is a very narrow field of view compared to the Fizeau mode. Unfortunately, this stellar interferometer project was abandoned due to various difficulties, including (i) the effect of atmospheric turbulence, (ii) variations of refractive index above the small subaperture, (iii) inadequate separation of the outer mirrors, and (iv) mechanical instability.

3. Intensity interferometer

Intensity interferometry considers the quantum theory of photon detection and correlation. It computes the fluctuations of the intensities $\mathcal{I}_1$ and $\mathcal{I}_2$ at two different points of the wave fronts. The fluctuations of the electrical signals from the two detectors are compared by a multiplier. The current output of each photoelectric detector is proportional to the instantaneous intensity $\mathcal{I}$ of the incident light, which is the squared modulus of the amplitude Ψ. The fluctuation of the current output is proportional to $\Delta\mathcal{I} = |\Psi|^2 - \langle |\Psi|^2 \rangle$. The covariance of the fluctuations, according to Goodman (1985), can be expressed as

$$\langle \Delta\mathcal{I}_1 \Delta\mathcal{I}_2 \rangle = \langle |\Psi_1 \Psi_2^*|^2 \rangle. \tag{31}$$

This expression indicates that the covariance of the intensity fluctuations is the squared modulus of the covariance of the complex amplitude.

Having completed an intensity interferometer that operated at radio wavelengths (Hanbury Brown *et al.*, 1952), Hanbury Brown and Twiss (1958) demonstrated its potential at optical wavelengths by measuring the angular diameter of Sirius. Subsequent development with a pair of 6.5-m light collectors on a circular railway track spanning 188 m provided measurements of 32 southern binary stars (Hanbury Brown, 1974) with an angular resolution limit of 0.5 milliarcseconds (mas). In this arrangement, starlight collected by two concave mirrors is focused onto two photoelectric cells, and the correlation of fluctuations in the photocurrents is measured as a function of mirror separation. The advantages of such a system over the Michelson interferometer are that it does not require high mechanical stability and remains unaffected by seeing. Another noted advantage is that the alignment tolerances are extremely relaxed, since the path lengths need to be maintained to a fraction of c/b_e, where b_e is the electrical bandwidth of the post-detection electronics. The significant effect comes from scintillation induced by the atmosphere. The sensitivity of this interferometer was found to be very low; it was limited by the narrow bandwidth filters that are used to increase the speckle lifetime. Correlated fluctuations can be obtained if the detectors are spaced by less than a speckle width. Theoretical calculations (Roddier, 1988) show that the limiting visual magnitude (mag) m_v that can be observed with such a system is of the order of 2. (The faintest stars visible to the naked eye are sixth magnitude. The magnitude scale is defined as $m_1 - m_2 = -2.5 \log F_1/F_2$, where m_1 and m_2 are the apparent magnitudes of two objects of fluxes F_1 and F_2, respectively.)

III. ATMOSPHERIC TURBULENCE

The density inhomogeneities appear to be created and maintained by the parameters that produce atmospheric turbulence and therefore refractive index inhomogeneities, viz., thermal gradients, humidity fluctuations, and wind shear. The gradients caused by these environmental parameters warp the wave front incident on the telescope pupil. The image quality is directly related to the statistics of the perturbations of the incoming wave front. The theory of seeing combines the theory of atmospheric turbulence with that of optical physics to predict the modifications to the diffraction-limited image that the refractive index gradients produce (Young, 1974; Roddier, 1981; Coulman, 1985). Atmospheric turbulence has a significant effect on the propagation of radio waves and sound waves, as well as on the flight of aircraft. This section is devoted to descriptions of atmospheric turbulence theory, the metrology of seeing, and its impact on stellar images.

A. Formation of eddies

Random fluctuations in the motion of the atmosphere occur predominantly due to (i) friction encountered by the air flow at the Earth's surface and consequent formation of a wind-velocity profile with large vertical gradients, (ii) differential heating of different portions of the Earth's surface and the concomitant development of thermal convection, (iii) processes associated with formation of clouds involving release of heat (condensation and crystallization) and subsequent changes in the nature of temperature and wind-velocity fields, (iv) convergence and interaction of air masses with various atmospheric fronts, and (v) obstruction of air flows by mountain barriers that generate wavelike disturbances and rotor motions on their leeside.

The atmosphere is difficult to study due to the high Reynolds number ($\mathrm{Re}\sim 10^6$), a dimensionless quantity, that characterizes the turbulence. When the average velocity v_a of a viscous fluid of characteristic size l is gradually increased, two distinct states of fluid motion are observed (Tatarski, 1967; Ishimaru, 1978), viz., (i) laminar (regular and smooth in space and time) at very low v_a, and (ii) unstable and random at v_a greater than some critical value. The Reynolds number, obtained by equating the inertial and viscous forces, is given by

$$\mathrm{Re}=v_a l/\nu_v, \tag{32}$$

where Re is a function of the flow geometry, v_a, l, and the kinematic viscosity of the fluid, ν_v. When Re exceeds critical value in a pipe (depending on its geometry), a transition of the flow from laminar to turbulent or chaotic occurs. Between these two extreme conditions, the flow passes through a series of unstable states. High Re turbulence is chaotic in both space and time and exhibits considerable spatial structure.

The velocity fluctuations occur on a wide range of space and time scales. According to which atmospheric turbulence model one uses (Taylor, 1921; Kolmogorov, 1941b, 1941c), the energy enters the flow at low frequencies at scale length L_0 and spatial frequency $k_{L_0}=2\pi/L_0$ as a direct result of the nonlinearity of the Navier-Stokes equation governing fluid motion. The size of large-scale fluctuations, referred to as large eddies, can be characterized by their outer scale length L_0. These eddies are not universal with respect to flow geometry; they vary according to the local conditions. Conan *et al.* (2000) derived a mean value $L_0=24$ m for a von Kármán spectrum from the data obtained at Cerro Paranal, Chile.

The energy is transported to smaller and smaller lossless eddies until, at a small enough Reynolds number, the kinetic energy of the flow is converted into heat by viscous dissipation, resulting in a rapid drop in power spectral density, $\Phi_n(\mathbf{k})$ for $k>k_0$, where k_0 is the critical wave number. These changes are characterized by the inner scale length l_0 and spatial frequency $k_{l_0}=2\pi/l_0$, where l_0 varies from a few millimeters near the ground to a centimeter high in the atmosphere. The small-scale fluctuations with sizes $l_0<r<L_0$, known as the inertial subrange, where r is the magnitude of $\mathbf{r}$, have universal statistics (scale-invariant behavior) independent of the flow geometry. The value of the inertial subrange would be different at various locations on the site. The statistical distribution of the size and number of these eddies is characterized by the spectral density $\Phi_n(\mathbf{k})$ of $n_1(\mathbf{r},t)$, where $n_1(\mathbf{r},t)$ is a randomly fluctuating term, and t is the time. The dependence of the refractive index of air, $n(\mathbf{r},t)$, upon pressure P (millibar) and temperature T (kelvin) at optical wavelengths is given by $n_1\cong n-1=77.6\times 10^{-6}P/T$ (Ishimaru, 1978).

B. Kolmogorov turbulence model

The optically important property of the Kolmogorov law is that refractive index fluctuations are largest for the largest turbulent elements up to the outer scale of the turbulence. At sizes below the outer scale, the one-dimensional (1D) power spectrum of the refractive index fluctuations falls off with the 5/3 power of frequency and is independent of the direction along which the fluctuations are measured, i.e., the small-scale fluctuations are isotropic (Young, 1974). The three-dimensional (3D) power spectrum Φ_n for the wave number $k>k_0$ in the case of an inertial subrange can be equated as

$$\Phi_n(\mathbf{k})=0.033\mathcal{C}_n^2 k^{-11/3}, \tag{33}$$

where $\mathcal{C}_n^2$ is known as the structure constant of the refractive index fluctuations.

This Kolmogorov-Obukhov model of turbulence, describing a power-law spectrum for the inertial intervals of wave numbers, is valid within the inertial subrange and is widely used for astronomical purposes (Tatarski, 1993). The refractive index structure function $\mathcal{D}_n(\mathbf{r})$ is defined as

$$\mathcal{D}_n(\mathbf{r})=\langle|n(\boldsymbol{\rho}+\mathbf{r})-n(\boldsymbol{\rho})|^2\rangle, \tag{34}$$

which expresses its variance at two points, r_1 and r_2.

The structure functions are related to the covariance function $\mathcal{B}_n(\mathbf{r})$ through

$$\mathcal{D}_n(\mathbf{r})=2[\mathcal{B}_n(\mathbf{0})-\mathcal{B}_n(\mathbf{r})], \tag{35}$$

where $\mathcal{B}_n(\mathbf{r})=\langle n(\boldsymbol{\rho})n(\boldsymbol{\rho}+\mathbf{r})\rangle$ and the covariance is the 3D Fourier transform of the power spectral density $\Phi_n(\mathbf{k})$ (Roddier, 1981). The structure function in the inertial range (homogeneous and isotropic random field) according to Kolmogorov (1941a) depends on the magnitude of $\mathbf{r}$, as well as on the rate of production or dissipation of turbulent energy ϵ_0 and the rate of production or dissipation of temperature inhomogeneities η_0.

The refractive index n is a function of the temperature T and humidity $\mathcal{H}$, that is, $n(T,\mathcal{H})$. Therefore the expectation value of the mean-square fluctuations about the average of the refractive index is given by

$$\langle dn\rangle^2=\left(\frac{\partial n}{\partial T}\right)^2\langle dT\rangle^2+2\left(\frac{\partial n}{\partial T}\right)\left(\frac{\partial n}{\partial \mathcal{H}}\right)\langle dT\rangle\langle d\mathcal{H}\rangle+\left(\frac{\partial n}{\partial \mathcal{H}}\right)^2\langle d\mathcal{H}\rangle^2. \tag{36}$$

It has been argued that the last term is negligible in optical propagation, and that the second term is negligible for most astronomical observations. It could be significant, however, in a high-humidity situation, e.g., a marine boundary layer (Roddier, 1981). Most treatments ignore the contribution from humidity and express the refractive index structure function (Tatarski, 1967) as

$$\mathcal{D}_n(\mathbf{r}) = \mathcal{C}_n^2 r^{2/3}. \tag{37}$$

Similarly, the velocity structure function $\mathcal{D}_v(\mathbf{r}) = \mathcal{C}_v^2 r^{2/3}$ and temperature structure function $\mathcal{D}_T(\mathbf{r}) = \mathcal{C}_T^2 r^{2/3}$ can also be derived; the same form holds for the humidity structure function. The two structure coefficients $\mathcal{C}_n$ and $\mathcal{C}_T$ are related by $\mathcal{C}_n = (\partial n/\partial T)\mathcal{C}_T$, and assuming pressure equilibrium, $\mathcal{C}_n = 80 \times (P/T^2)\mathcal{C}_T$ (Roddier, 1981).

Several experiments confirm this two-thirds power law in the atmosphere (Wyngaard *et al.*, 1971; Coulman, 1974; Hartley *et al.*, 1981; Lopez, 1991). Robbe *et al.* (1997) reported on observations using a long-baseline optical interferometer, the Interféromètre à Deux Télescopes (I2T; Labeyrie, 1975), that most of the measured temporal spectra of the angle of arrival exhibited a behavior compatible with the power law. Davis and Tango (1996) measured an atmospheric coherence time that varied between ~ 1 and ~ 7 ms with the Sydney University Stellar Interferometer (SUSI).

The value of $\mathcal{C}_n^2$ [in Eq. (33)] depends on local conditions as well as on the planetary boundary layer. The significant scale lengths in the case of the former depend on local objects that introduce changes primarily in the inertial subrange and temperature differentials. The latter can be attributed to (i) the surface boundary layer due to ground convection, extending up to a few kilometers into the atmosphere ($\mathcal{C}_T^2 \propto z^{-2/3}$), (ii) the free convection layer associated with orographic disturbances, where the scale lengths are height dependent ($\mathcal{C}_T^2 \propto z^{-4/3}$), and (iii) turbulence in the tropopause and above due to wind shear as the temperature gradient vanishes slowly. In real turbulent flows, turbulence is usually generated at solid boundaries. Near the boundaries, shear is the dominant source (Nelkin, 2000), and scale lengths are roughly constant. In an experiment conducted by Cadot *et al.* (1997), it was found that Kolmogorov scaling is a good approximation for the energy dissipation as well as for the torque due to viscous stress. They measured the energy dissipation and the torque for a circular Couette flow with and without small vanes attached to the cylinders to break up the boundary layer. The theory of turbulent flow in the neighborhood of a flat surface applies to the atmospheric surface layer. Masciadri *et al.* (1999) noticed that the value of $\mathcal{C}_n^2$ increased about 11 km over Mt. Paranal, Chile. The turbulence was concentrated in a thin layer of 100–200 m in thickness, where the value of $\mathcal{C}_n^2$ increased by more than an order of magnitude over its background level.

C. Wave propagation through turbulence

The spatial correlational properties of turbulence-induced field perturbations are evaluated by combining basic turbulence theory with the stratification and phase screen approximations. The variance of a ray can be translated into the variance of the phase fluctuations. For such a calculation, Roddier (1981) used the correlation properties for propagation through a single (thin) turbulence layer and then extended the procedure to account for many such layers. Several investigators (Goodman, 1985; Troxel *et al.*, 1994) have argued that individual layers can be treated as independent provided that the separation of the layer centers is chosen large enough so that the fluctuations of the log amplitude and phase introduced by different layers are uncorrelated.

1. Effect of turbulent layers

Let a monochromatic plane wave of wavelength λ from a distant star at the zenith propagate towards the ground-based observer; the complex amplitude at coordinate $(\mathbf{x},h)$ is given by

$$\Psi_h(\mathbf{x}) = |\Psi_h(\mathbf{x})| e^{i\psi_h(\mathbf{x})}. \tag{38}$$

The average value of the phase is $\langle \psi_h(\mathbf{x}) \rangle = 0$ for height h, and the unperturbed complex amplitude outside the atmosphere is normalized to unity $[\Psi_\infty(\mathbf{x}) = 1]$. When this wave is allowed to pass through a thin layer of turbulent air of thickness δh_j, which is considered to be large compared to the scale of turbulent eddies but small enough for the phase screen approximation (diffraction effects are negligible over the distance δh_j), the complex amplitude of the plane wave front after passing through the layer is expressed as

$$\Psi_j(\mathbf{x}) = e^{i\psi_j(\mathbf{x})}. \tag{39}$$

Here the phase shift $\psi_j(\mathbf{x})$ introduced by the refractive index fluctuations $n(x,z)$ inside the layer can be written as

$$\psi_j(\mathbf{x}) = k \int_{h_j}^{h_j + \delta h_j} n(x,z)\, dz. \tag{40}$$

In this case, the rest of the atmosphere is assumed to be calm and homogeneous.

At the layer output, the coherence function of the complex amplitude, $\langle \Psi_j(\mathbf{x}) \Psi_j^*(\mathbf{x}+\boldsymbol{\xi}) \rangle$, leads to

$$\mathcal{B}_j(\boldsymbol{\xi}) = \langle e^{i[\psi_j(\mathbf{x}) - \psi_j(\mathbf{x}+\boldsymbol{\xi})]} \rangle. \tag{41}$$

The quantity $\psi_j(\mathbf{x})$ can be considered to be the sum of a large number of independent variables and therefore has Gaussian statistics. This equation is similar to the Fourier transform of the probability density function at unit frequency; therefore

$$\mathcal{B}_j(\boldsymbol{\xi}) = e^{-(1/2)\mathcal{D}_{\psi_j}(\boldsymbol{\xi})}. \tag{42}$$

The term $\mathcal{D}_{\psi_j}(\boldsymbol{\xi})$ is the 2D structure function of the phase $\psi_j(\mathbf{x})$ that can be read as (Fried, 1966)

$$\mathcal{D}_{\psi_j}(\boldsymbol{\xi}) = \langle |\psi_j(\mathbf{x}) - \psi_j(\mathbf{x}+\boldsymbol{\xi})|^2 \rangle. \tag{43}$$

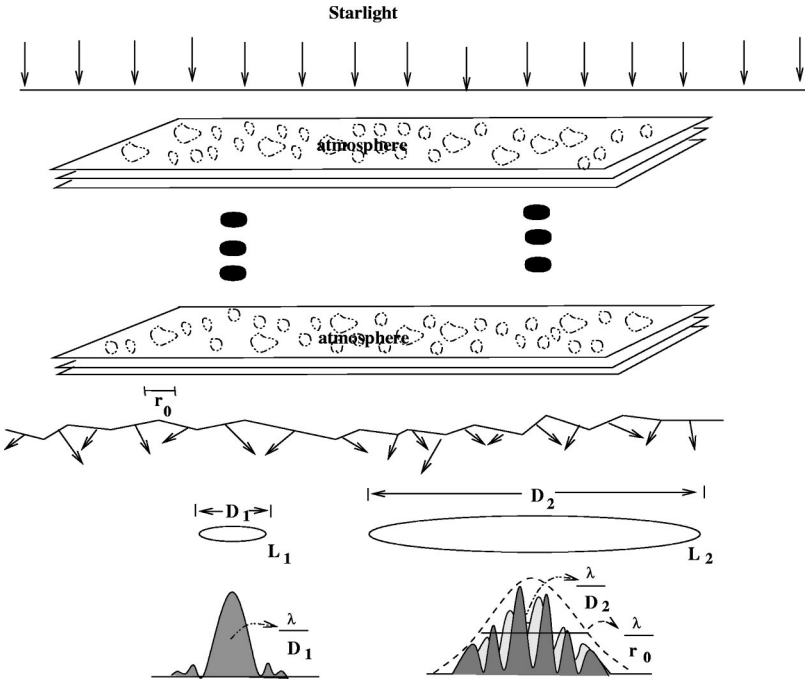

FIG. 1. Plane-wave propagation through multiple turbulent layers. L_1 and L_2 represent small and large telescopes with respective diameters D_1 and D_2.

2. Computation of phase structure function

Let the covariance of the phase $\mathcal{B}_{\psi_j}(\boldsymbol{\xi})$ be defined as

$$\mathcal{B}_{\psi_j}(\boldsymbol{\xi}) = \langle \psi_j(\mathbf{x})\psi_j(\mathbf{x}+\boldsymbol{\xi})\rangle. \tag{44}$$

By replacing $\psi_j(\mathbf{x})$, we obtain

$$\mathcal{B}_{\psi_j}(\boldsymbol{\xi}) = k^2 \int_{h_j}^{h_j+\delta h_j} dz \int_{h_j-z}^{h_j+\delta h_j-z} \mathcal{B}_n(\boldsymbol{\xi},\zeta)\, d\zeta, \tag{45}$$

where $\zeta = z' - z$ and the 3D refractive index covariance is

$$\mathcal{B}_n(\boldsymbol{\xi},\zeta) = \langle n(\mathbf{x},z)n(\mathbf{x}+\boldsymbol{\xi},z')\rangle. \tag{46}$$

Since the thickness of the layer, δh_j, is large compared to the correlation scale of the turbulence, the integration over ζ from $-\infty$ *to* $+\infty$ leads to

$$\mathcal{B}_{\psi_j}(\boldsymbol{\xi}) = k^2 \delta h_j \int \mathcal{B}_n(\boldsymbol{\xi},\zeta)\, d\zeta. \tag{47}$$

The phase structure function is related to its covariance [Eq. (35)]; therefore

$$\mathcal{D}_{\psi_j}(\boldsymbol{\xi}) = 2k^2 \delta h_j \int [\mathcal{B}_n(\mathbf{0},\zeta) - \mathcal{B}_n(\boldsymbol{\xi},\zeta)]\, d\zeta. \tag{48}$$

The refractive index structure function defined in Eq. (37) is evaluated as

$$\mathcal{D}_n(\boldsymbol{\xi},\zeta) = \mathcal{C}_n^2(\xi^2+\zeta^2)^{1/3}. \tag{49}$$

Equation (48) can be integrated using Eq. (35) to yield

$$\mathcal{D}_{\psi_j}(\boldsymbol{\xi}) = 2.91k^2\mathcal{C}_n^2\xi^{5/3}\delta h_j. \tag{50}$$

The covariance of the phase is deduced by substituting Eq. (50) in Eq. (42):

$$\mathcal{B}_{h_j}(\boldsymbol{\xi}) = e^{-(1/2)(2.91k^2\mathcal{C}_n^2\xi^{5/3}\delta h_j)}. \tag{51}$$

Using the Fresnel approximation, we find that the covariance of the phase at ground level due to a thin layer of turbulence at some height off the ground is given by

$$\mathcal{B}_0(\boldsymbol{\xi}) = \mathcal{B}_{h_j}(\boldsymbol{\xi}). \tag{52}$$

For high-altitude layers the complex field will fluctuate both in phase and in amplitude (scintillation), and therefore the wave structure function $\mathcal{D}_{\psi_j}(\boldsymbol{\xi})$ is not strictly true as at the ground level. The turbulent layer acts like a diffracting screen; however, correction in the case of astronomical observation remains small (Roddier, 1981).

The wave structure function after passing through N layers can be expressed as the sum of the N wave structure functions associated with the individual layers. For each layer, the coherence function is multiplied by the term $e^{-(1/2)[2.91k^2\mathcal{C}_n^2(h_j)\xi^{5/3}\delta h_j]}$; therefore the coherence function at ground level is given by

$$\begin{aligned}\mathcal{B}_0(\boldsymbol{\xi}) &= \prod_{j=1}^{N} e^{-(1/2)[2.91k^2\mathcal{C}_n^2(h_j)\xi^{5/3}\delta h_j]} \\ &= e^{-(1/2)[2.91k^2\xi^{5/3}\sum_{j=1}^{N}\mathcal{C}_n^2(h_j)\delta h_j]}.\end{aligned} \tag{53}$$

This expression may be generalized for a star at an angular distance γ away from the zenith viewed through all of the turbulent atmosphere:

$$\mathcal{B}_0(\boldsymbol{\xi}) = \exp\left(-(1/2)\left[2.91k^2\xi^{5/3}\sec\gamma \int \mathcal{C}_n^2(z)\, dz\right]\right). \tag{54}$$

3. Seeing-limited images

The term "seeing" refers to the total effect of distortion in the path of starlight through different contributing layers of the atmosphere up to the detector placed at the focus of the telescope. Let the modulation transfer function of the atmosphere and a telescope together be

described as in Fig. 1. The long-exposure point-spread function is defined by the ensemble average $\langle \mathcal{S}(\mathbf{x}) \rangle$, which is independent of the direction. If the object emits incoherently, the average illumination $\langle \mathcal{I}(\mathbf{x}) \rangle$ of a resolved object $\mathcal{O}(\mathbf{x})$ obeys the convolution relationship

$$\langle \mathcal{I}(\mathbf{x}) \rangle = \mathcal{O}(\mathbf{x}) \star \langle \mathcal{S}(\mathbf{x}) \rangle. \tag{55}$$

Using the 2D Fourier transform, we can translate the above equation into

$$\langle \hat{\mathcal{I}}(\mathbf{u}) \rangle = \hat{\mathcal{O}}(\mathbf{u}) \cdot \langle \hat{\mathcal{S}}(\mathbf{u}) \rangle, \tag{56}$$

where $\langle \hat{\mathcal{S}}(\mathbf{u}) \rangle$ denotes the transfer function for long-exposure images, $\mathbf{u}$ the spatial frequency vector with magnitude u, and $\hat{\mathcal{O}}(\mathbf{u})$ the object spectrum. The argument of Eq. (56) is expressed as

$$\arg|\hat{\mathcal{I}}(\mathbf{u})| = \psi(\mathbf{u}) + \theta_1 - \theta_2, \tag{57}$$

where $\psi(\mathbf{u})$ is the Fourier phase at $\mathbf{u}$, arg|| stands for "the phase of," and θ_j respresent the apertures corresponding to the seeing cells. The transfer function is the product of the atmosphere transfer function (wave coherence function) $\mathcal{B}(\mathbf{u})$ and the telescope transfer function $\mathcal{T}(\mathbf{u})$:

$$\langle \hat{\mathcal{S}}(\mathbf{u}) \rangle = \mathcal{B}(\mathbf{u}) \cdot \mathcal{T}(\mathbf{u}). \tag{58}$$

For a long exposure through the atmosphere, the resolving power $\mathcal{R}$ of any optical telescope can be expressed as

$$\mathcal{R} = \int \mathcal{B}(\mathbf{u}) \cdot \mathcal{T}(\mathbf{u}) d\mathbf{u}. \tag{59}$$

It is limited either by the telescope or by the atmosphere, depending on the relative width of the two functions, $\mathcal{B}(\mathbf{u})$ and $\mathcal{T}(\mathbf{u})$:

$$\mathcal{R} = \begin{cases} \int \mathcal{T}(\mathbf{u}) d\mathbf{u} = \dfrac{\pi}{4}\left(\dfrac{D}{\lambda}\right)^2, & D \ll r_0 \quad (60) \\ \int \mathcal{B}(\mathbf{u}) d\mathbf{u} = \dfrac{\pi}{4}\left(\dfrac{r_0}{\lambda}\right)^2, & D \gg r_0. \quad (61) \end{cases}$$

a. Fried's parameter

According to Eq. (54), $\mathcal{B}(\mathbf{u})$ can be expressed as

$$\mathcal{B}(\mathbf{u}) = \mathcal{B}_0(\lambda \mathbf{u}) = \exp\left(-(1/2) \times \left[2.91 k^2 (\lambda u)^{5/3} \sec\gamma \int \mathcal{C}_n^2(z) dz \right] \right). \tag{62}$$

Therefore Eq. (61) translates into

$$\mathcal{R} = (6\pi/5)\left[\frac{1}{2}\left(2.91 k^2 \lambda^{5/3} \sec\gamma \int \mathcal{C}_n^2(z) dz \right) \right]^{-6/5} \Gamma(6/5). \tag{63}$$

Fried (1966) introduced the critical diameter r_0 for a telescope. When we place $D = r_0$ in Eq. (60), Eq. (62) takes the form

$$\mathcal{B}(\mathbf{u}) = e^{-3.44(\lambda u / r_0)^{5/3}}, \tag{64}$$

$$\mathcal{B}_0(\boldsymbol{\xi}) = e^{-3.44(\xi / r_0)^{5/3}}. \tag{65}$$

The phase structure function [Eq. (43)] across the telescope aperture (Fried, 1966) becomes

$$\mathcal{D}_\psi(\boldsymbol{\xi}) = 6.88\left(\frac{\xi}{r_0} \right)^{5/3}. \tag{66}$$

By replacing the value of $\mathcal{B}_0(\boldsymbol{\xi})$ in Eq. (54), we find an expression for r_0 in terms of the distribution of the turbulence in the atmosphere:

$$r_0 = \left[0.423 k^2 \sec\gamma \int \mathcal{C}_n^2(z) dz \right]^{-3/5}. \tag{67}$$

Fried's parameter may be thought of as the diameter of telescope that would produce the same diffraction-limited full width at half maximum (FWHM) of a point-source image as the atmospheric turbulence would with an infinite-sized mirror.

b. Seeing at the telescope site

The major sources of image degradation are predominantly thermal and aerodynamic disturbances in the atmosphere surrounding the telescope and its enclosure. These sources include (i) convection in and around the building and the dome, as well as off the surface of the telescope structure, (ii) thermal distortion of the primary and secondary mirrors when they are warmer than the ambient air, (iii) dissipation of heat by the secondary mirror (Zago, 1995), (iv) a rise in temperature at the primary mirror cell, and (v) a rise in temperature at the focal point causing a temperature gradient close to the detector. Degradation in image quality can occur due to optomechanical aberrations as well as mechanical vibrations of the optical system.

Various corrective measures have been proposed to improve seeing. These measures include (i) insulating the surface of the floors and walls, (ii) introducing an active cooling system to eliminate the heat produced by electric equipment on the telescope and elsewhere in the dome, and (iii) installing a ventilator to generate a downward air flow through the slit to counteract the upward action of the bubbles (Racine, 1984; Ryan and Wood, 1995). Floor-chilling systems to dampen the natural convection have been implemented to keep the temperature of the primary mirror closer to that of the surrounding air volume (Zago, 1995). Saha and Chinnappan (1999) found that the average observed r_0 is higher during the later part of the night than the earlier part. This change might indicate that the slowly cooling mirror creates thermal instabilities that decrease slowly during the night.

IV. SINGLE-APERTURE DIFFRACTION-LIMITED IMAGING

Ever since the development of the SI technique (Labeyrie, 1970), it has been widely employed in both the visible and the infrared (IR) bands at telescopes to decipher diffraction-limited information. The following

subsections deal with single-aperture and other related forms of speckle imaging, other techniques, AO imaging systems, dark speckle imaging, and high-resolution sensors.

A. Speckle imaging

If a point source is imaged through the telescope by using the pupil function, which consists of two subapertures (θ_1,θ_2) corresponding to the two seeing cells separated by a vector $\lambda\mathbf{u}$, a fringe pattern is produced with a narrow spatial frequency bandwidth that moves within a broad point-spread-function envelope. With increasing distance between the subapertures, the fringes move with an increasingly larger amplitude. The introduction of a third subaperture gives three pairs of subapertures and yields the appearance of three intersecting patterns of moving fringes. Covering the telescope aperture with r_0-sized subapertures synthesizes an interferometer with a filled aperture p_j (each p_n,p_m pair is separated by a baseline). The intensity at the focal plane $\mathcal{I}$, according to diffraction theory (Born and Wolf, 1984), is determined by the expression

$$\mathcal{I}=\sum_{n,m}\langle\Psi_n\Psi_m^*\rangle. \tag{68}$$

The term $\Psi_n\Psi_m^*$ is multiplied by $e^{i\psi}$, where ψ is the random instantaneous shift in the fringe pattern. Each subaperture is small enough for the field to be coherent over its extent. Atmospheric turbulence does not affect the contrast of the fringes produced but introduces phase delays. If the integration time is shorter than the evolution time of the phase inhomogeneities, the interference fringes are preserved but their phases are randomly distorted, which produces "speckles." (The formation of speckles stems from the summation of coherent vibrations having random characteristics. It can be modeled as a two-dimensional random walk with Fresnel's vector representation of vibrations.) Each speckle covers an area of the same order of magnitude as the Airy disk of the telescope. The number of correlation cells is proportional to the square of D/r_0, and the number of photons N_p per speckle is independent of its diameter. The lifetime of speckles is approximately $\tau_0\sim r_0/\Delta\nu$, where $\Delta\nu$ is the velocity dispersion in the turbulent seeing layers across the line of sight.

The structure of the speckle pattern changes randomly over a short interval of time. The sum of several such statistically uncorrelated patterns from a point source can result in a uniform patch of light a few arcseconds wide. Figures 2 and 3 depict the speckles of a binary star, HR4689, and the results of summing 128 specklegrams, respectively. When $\hat{\mathcal{I}}(\mathbf{u})$ is averaged over many frames, the result for frequencies greater than r_0/λ tends to zero because the phase difference, $\theta_1-\theta_2$, mod 2π, between the two apertures is distributed uniformly between $\pm\pi$, with zero mean. The Fourier component performs a random walk in the complex plane and averages to zero:

$$\langle\hat{\mathcal{I}}(\mathbf{u})\rangle=0,\quad u>r_0/\lambda. \tag{69}$$

In general, a high-quantum-efficiency detector is needed to record magnified short-exposure images for such an observation. To compensate for atmospherically induced dispersion at zenith angles larger than a few degrees, either a counter-rotating computer-controlled dispersion-correcting prism or a narrow-bandwidth filter is used.

1. Speckle interferometry

Speckle interferometry (SI) estimates a *power spectrum*, which is the ensemble average of the squared modulus of an ensemble of Fourier transform from a set of specklegrams, $\mathcal{I}_k(\mathbf{x})$, where $k=t_1,t_2,t_3,\ldots,t_M$. The intensity of the image, $\mathcal{I}(\mathbf{x})$, in the case of a quasimonochromatic incoherent source can be expressed as

$$\mathcal{I}(\mathbf{x})=\int\mathcal{O}(\mathbf{x}')\mathcal{S}(\mathbf{x}-\mathbf{x}')d\mathbf{x}', \tag{70}$$

where $\mathcal{O}(\mathbf{x}')$ is an object at a point anywhere in the field of view.

The variability of the corrugated wave front yields "speckle boiling" and is the source of speckle noise that arises from difference in registration between the evolving speckle pattern and the boundary of the point-spread function area in the focal plane. These specklegrams have additive noise contamination $\mathcal{N}_j(\mathbf{x})$, which includes all additive measurement of uncertainties. This may be in the form of (i) photon statistics noise and (ii) all distortions from the idealized isoplanatic model represented by the convolution of $\mathcal{O}(\mathbf{x})$ with $\mathcal{S}(\mathbf{x})$, such as nonlinear geometrical distortions arising from the optical trains of the telescope. For each of the short-exposure instantaneous records, the imaging equation applies:

$$\mathcal{I}(\mathbf{x})=\mathcal{O}(\mathbf{x})\star\mathcal{S}(\mathbf{x})+\mathcal{N}(\mathbf{x}). \tag{71}$$

Denoting the noise spectrum as $\hat{\mathcal{N}}(\mathbf{u})$, the Fourier space relationship between the object and the image is

$$\hat{\mathcal{I}}(\mathbf{u})=\hat{\mathcal{O}}(\mathbf{u})\cdot\hat{\mathcal{S}}(\mathbf{u})+\hat{\mathcal{N}}(\mathbf{u}). \tag{72}$$

Taking the modulus square of the expression and averaging over many frames, we find the average image power spectrum:

$$\langle|\hat{\mathcal{I}}(\mathbf{u})|^2\rangle=|\hat{\mathcal{O}}(\mathbf{u})|^2\cdot\langle|\hat{\mathcal{S}}(\mathbf{u})|^2\rangle+\langle|\hat{\mathcal{N}}(\mathbf{u})|^2\rangle. \tag{73}$$

Since $|\hat{\mathcal{S}}(\mathbf{u})|^2$ is a random function in which the detail is continuously changing, its ensemble average becomes smoother.

By the Wiener-Khintchine theorem (Mendel and Wolf, 1995), the inverse Fourier transform of Eq. (73) gives the autocorrelation of the object $\mathcal{A}[\mathcal{O}(\mathbf{x})]$,

$$\mathcal{A}[\mathcal{O}(\mathbf{x})]=\mathcal{F}^-[|\hat{\mathcal{O}}(\mathbf{u})|^2]. \tag{74}$$

In this technique, the atmospheric phase contribution is eliminated but the averaged signal is nonzero, i.e.,

$$\langle\hat{\mathcal{I}}^A(\mathbf{u})\rangle\neq0. \tag{75}$$

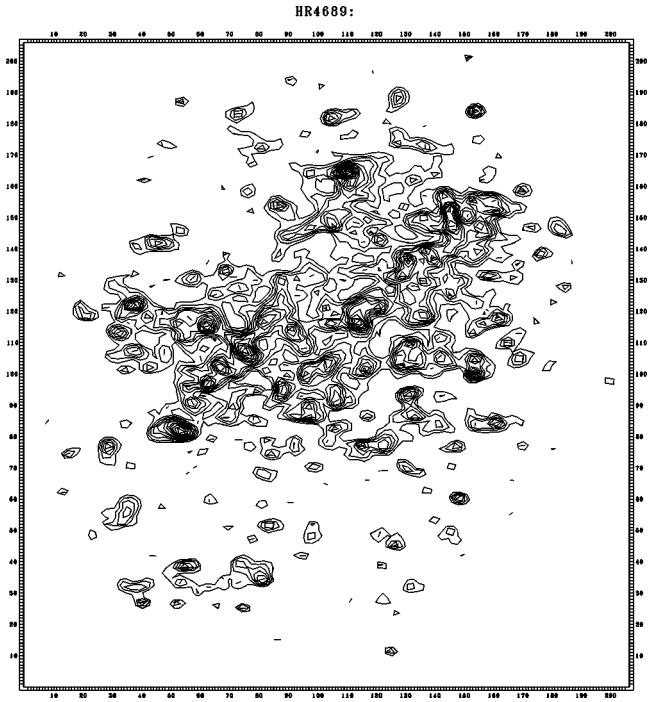

FIG. 2. Specklegram of a binary star, HR4689, obtained at the Vainu Bappu Telescope (VBT), Kavalur, India.

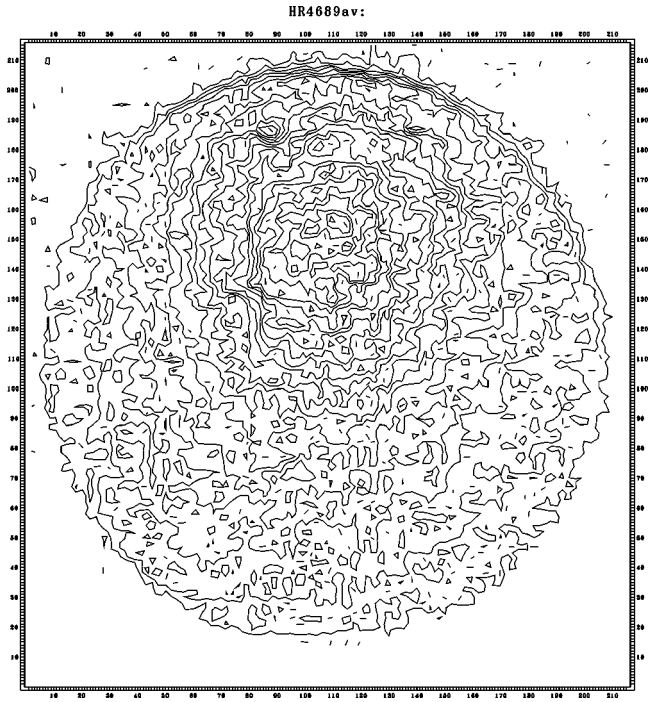

FIG. 3. The result of summing 128 specklegrams of HR4689, demonstrating the destruction of finer details of the image by atmospheric turbulence.

The argument of Eq. (72) is given by the expression

$$\arg|\hat{\mathcal{I}}(\mathbf{u})|^2=\psi(\mathbf{u})+\theta_1-\theta_2+\psi(-\mathbf{u})-\theta_1+\theta_2=0. \tag{76}$$

The transfer function of $\mathcal{S}(\mathbf{x})$ is generally estimated by calculating the power spectrum of the instantaneous intensity from an unresolved star. Saha and Maitra (2001) developed an algorithm in which a Wiener parameter w_1 is added to a point-spread-function power spectrum. The classic Wiener filter that resulted from electronic information theory, in which diffraction limits do not mean much, is meant to deal with signal-dependent "colored" noise. In practice, this term is usually just a constant, a noise control parameter whose scale is estimated from the noise power spectrum. In this case, it is assumed that the noise is white and that one can estimate its scale in regions of the power spectrum where the signal is zero (outside the diffraction limit for an imaging system):

$$|\hat{O}(\mathbf{u})|^2=\frac{\langle|\hat{I}(\mathbf{u})|^2\rangle}{[\langle|\hat{S}(\mathbf{u})|^2\rangle+w_1]}. \tag{77}$$

The SI technique in the case of the components in a group of stars retrieves the separation, the position angle with 180° ambiguity, and the relative magnitude difference at low light levels. Figure 4 depicts the autocorrelation of a binary system, HR4689. Another algorithm called the directed-vector autocorrelation method is found to be effective in eliminating the 180° ambiguity (Bagnuolo *et al.*, 1992).

2. Speckle holography

If a reference point source is available within the isoplanatic patch ($\sim$7 arcsec), it is used as a key to reconstruct the target in the same way that reference coherent beam is employed in holographic reconstruction (Liu and Lohmann, 1973). Let the point source be represented by a Dirac impulse $A_0\delta(\mathbf{x})$ at the origin and $\mathcal{O}_1(\mathbf{x})$ be the nearby object to be reconstructed. The intensity distribution in the field of view is

$$\mathcal{O}(\mathbf{x})=A_0\delta(\mathbf{x})+\mathcal{O}_1(\mathbf{x}). \tag{78}$$

The squared modulus of its Fourier transform is derived as

$$|\hat{\mathcal{O}}(\mathbf{u})|^2=A_0^2+A_0\hat{\mathcal{O}}_1(\mathbf{u})+A_0\hat{\mathcal{O}}_1^*(\mathbf{u})+\hat{\mathcal{O}}_1(\mathbf{u})\hat{\mathcal{O}}_1^*(\mathbf{u}). \tag{79}$$

The inverse Fourier transform of this equation translates into

$$\mathcal{A}[\mathcal{O}(\mathbf{x})]=A_0^2\delta(\mathbf{x})+A_0\mathcal{O}_1(\mathbf{x})+A_0\mathcal{O}_1(-\mathbf{x})+\mathcal{A}[\mathcal{O}_1(\mathbf{x})]. \tag{80}$$

The first and the last terms in Eq. (80) are centered at the origin. If the object is far enough from the reference source $\mathcal{O}(\mathbf{x})$, its mirror image, $\mathcal{O}(-\mathbf{x})$, is therefore recovered apart from a 180° rotation ambiguity.

3. Differential speckle interferometry

Differential speckle interferometry is a method of observing the objects in different spectral channels simultaneously and computing the average cross correlation of pairs of speckle images (Beckers, 1982). Let $\mathcal{O}_1(\mathbf{x})$ and $\mathcal{O}_2(\mathbf{x})$ be the source brightness distributions at λ_1 and λ_2, respectively, and $\mathcal{I}_1(\mathbf{x})$ and $\mathcal{I}_2(\mathbf{x})$ their associ-

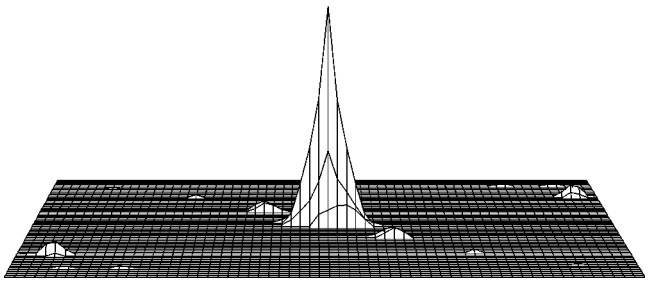

FIG. 4. Autocorrelation of a binary system, HR4689; the second star in the binary is one of the two distinct bumps that are symmetrically placed on either side of the main peak. The bumps at the edge of the figure are artifacts.

ated instantaneous image intensity distributions. The relation between the object and the image in Fourier space becomes

$$\hat{\mathcal{I}}_1(\mathbf{u}) = \hat{\mathcal{O}}_1(\mathbf{u}) \cdot \hat{\mathcal{S}}_1(\mathbf{u}), \tag{81}$$

$$\hat{\mathcal{I}}_2(\mathbf{u}) = \hat{\mathcal{O}}_2(\mathbf{u}) \cdot \hat{\mathcal{S}}_2(\mathbf{u}), \tag{82}$$

where $\hat{\mathcal{S}}_1(\mathbf{u})$ and $\hat{\mathcal{S}}_2(\mathbf{u})$ are the related transfer functions. The average cross spectrum is given by

$$\langle \hat{\mathcal{I}}_1(\mathbf{u}) \hat{\mathcal{I}}_2^*(\mathbf{u}) \rangle = \hat{\mathcal{O}}_1(\mathbf{u}) \hat{\mathcal{O}}_2^*(\mathbf{u}) \cdot \langle \hat{\mathcal{S}}_1(\mathbf{u}) \hat{\mathcal{S}}_2^*(\mathbf{u}) \rangle. \tag{83}$$

The transfer function, $\langle \hat{\mathcal{S}}_1(\mathbf{u}) \hat{\mathcal{S}}_2^*(\mathbf{u}) \rangle$, can be calibrated on the reference point source for which $\langle \hat{\mathcal{O}}_1(\mathbf{u}) \rangle = \langle \hat{\mathcal{O}}_2(\mathbf{u}) \rangle = 1$. If the two spectral windows are close enough ($\Delta\lambda/\lambda \ll r_0/D$), the instantaneous transfer function is assumed to be identical in both channels [$\mathcal{S}_1 = \mathcal{S}_2 = \mathcal{S}$]. Therefore Eq. (83) becomes

$$\hat{\mathcal{O}}_1(\mathbf{u}) = \frac{\langle \hat{\mathcal{I}}_1(\mathbf{u}) \hat{\mathcal{I}}_2^*(\mathbf{u}) \rangle}{\hat{\mathcal{O}}_2^*(\mathbf{u}) \langle |\hat{\mathcal{S}}(\mathbf{u})|^2 \rangle} = \hat{\mathcal{O}}_2(\mathbf{u}) \frac{\langle \hat{\mathcal{I}}_1(\mathbf{u}) \hat{\mathcal{I}}_2^*(\mathbf{u}) \rangle}{\langle |\hat{\mathcal{I}}_2(\mathbf{u})|^2 \rangle}. \tag{84}$$

The noise contributions from two different detectors are uncorrelated, and thereby their contributions cancel out. Differential speckle interferometry estimates the ratio $\hat{\mathcal{O}}_1(\mathbf{u})/\hat{\mathcal{O}}_2(\mathbf{u})$, and the differential image $\mathcal{D}_{\mathcal{I}}(\mathbf{x})$ is obtained by performing an inverse Fourier transform of this ratio

$$\mathcal{D}_{\mathcal{I}}(\mathbf{x}) = \mathcal{F}^{-1} \left[\frac{\langle \hat{\mathcal{I}}_1(\mathbf{u}) \hat{\mathcal{I}}_2^*(\mathbf{u}) \rangle}{\langle |\hat{\mathcal{I}}_2(\mathbf{u})|^2 \rangle} \right], \tag{85}$$

where $\mathcal{D}_{\mathcal{I}}(\mathbf{x})$ represents an image of the object in the emission feature having the resolution of the object imaged in the continuum.

4. Speckles and shadow bands

When any planetary body of notable size passes in front of a star, the light coming from the latter is occulted. The profiles of stellar occultations by the Moon show diffraction patterns as the star is being occulted, provided the data are recorded at high time resolution. The method remains useful because of the extraordinary geometric precision it provides. The notable advantage of occultation of binary stars is that it can help one determine relative intensities and measure separations comparable to those measured by long-baseline interferometers. Speckle surveys have resolved known occulting binaries down to a separation of about <0.025 arcsec (Mason, 1996). Furthermore, this method provides a means of determining the limiting magnitude difference of SI. The shortcomings of this technique are due to its singular nature: the object may not occult again until one Saros cycle later (18.6 yr) and must be limited to a belt of the sky (10% of the celestial sphere).

5. Speckle spectroscopy

The application of the SI technique to speckle spectroscopic observations enables one to obtain spectral resolution with high spatial resolution of astronomical objects simultaneously. The intensity distribution $\mathcal{W}(\mathbf{x})$ of an instantaneous objective prism speckle spectrogram is expressed as

$$\mathcal{W}(\mathbf{x}) = \sum_m \mathcal{O}_m(\mathbf{x} - \mathbf{x}_m) \star \mathcal{G}_m(\mathbf{x}) \star \mathcal{S}(\mathbf{x}), \tag{86}$$

where $\mathcal{O}_m(\mathbf{x} - \mathbf{x}_m)$ denotes the intensity of the mth object pixel and $\mathcal{G}_m(\mathbf{x})$ is the spectrum of the object pixel. In the narrow-wavelength bands (<30 nm), the point-spread function $\mathcal{S}(\mathbf{x})$ is wavelength independent. The objective prism spectrum $\Sigma_m \mathcal{O}_m(\mathbf{x} - \mathbf{x}_m) \star \mathcal{G}_m(\mathbf{x})$ can be reconstructed from the speckle spectrograms.

In a speckle spectrograph, either a prism or a grism can be employed to disperse 1D specklegrams (Grieger *et al.*, 1988). An imaging spectrometer uses two synchronized detectors to record the dispersed speckle pattern and the specklegrams of the object (Baba, Kuwamura, *et al.*, 1994); a reflection grating acts as disperser.

6. Speckle polarimetry

In general, radiation is polarized, and the measurement of polarization parameters is important in understanding the emission mechanisms. Processes such as electric and magnetic fields, scattering, chemical interactions, molecular structure, and mechanical stress cause changes in the polarization state of an optical beam. Applications relying on the study of these changes cover a vast area, including astrophysics and molecular biology. Such observations are important in astronomy for obtaining information about the size and shapes of dust envelopes around stars, the size and shape of the dust grains, and magnetic fields. Among other astronomical objectives worth investigating are the wavelength dependence of the degree of polarization and the rotation of the position angle of emitted light from (i) stars with extended atmospheres, and (ii) stars present in very young ($\leqslant 2 \times 10^6$ yr) clusters and associations.

The modified incident polarization caused by the reflection of a mirror is characterized by two parameters: (i) the ratio between the reflection coefficients of the electric vector components perpendicular and parallel to the plane of incidence, known as s and p components, respectively, and (ii) the relative phase shift between

these electric vibrations. The effect on the statistics of a speckle pattern is the degree of depolarization caused by the scattering at the surface. If the light is depolarized, the resulting speckle field is considered to be the sum of two component speckle fields produced by scattered light polarized in two orthogonal directions. The intensity at any point is the sum of the intensities of the component speckle patterns (Goodman, 1975). These patterns are partially correlated; therefore a polarizer that transmits one of the component speckle patterns is used in the speckle camera system (Falcke *et al.*, 1996). The advantage of using a speckle camera over a conventional imaging polarimeter is that it helps in monitoring the short-time variability of the atmospheric transmission.

7. Speckle imaging of extended objects

Image recovery is relatively simple when the target is a point source. Nevertheless, interferometric observations can reveal fundamental processes on the Sun, such as changes in convection and magnetic fields, that take place on subarcsecond scales. The limitations come from (i) the rapid evolution of solar granulation, which prevents the collection of long sequences of specklegrams for reconstruction, and (ii) the lack of efficient detectors to record a large number of frames within the stipulated time before the structure changes. Another major problem of reconstructing images comes from difficulty in estimating the point-spread function due to the lack of a reference point source. The spectral ratio technique (Von der Lühe, 1984), which is based on a comparison between long- and short-exposure images, has been employed (Wilken *et al.*, 1997) to derive Fried's parameter. Models of the speckle transfer function (Korff, 1973) and of the average short-exposure modulation transfer function have also been applied to compare the observed spectral ratios with theoretical values. High-resolution solar images obtained during partial solar eclipses may help in estimating the seeing effect (Callados and Vàzquez, 1987). The limb of the moon eclipsing the sun provides a sharp edge as a reference object. The intensity profile falls off sharply at the limb. The departure of this falloff gives an indirect estimate of the atmospheric point-spread function.

B. Other techniques

Several other methods, viz., pupil-plane techniques such as wave-front shearing interferometry, phase-closure methods, and phase-diversity techniques are also employed at single telescopes in order to obtain diffraction-limited information.

1. Shearing interferometry

Shearing interferometers make use of the principle of self-referencing; that is, they combine the wave front with a shifted version of itself to form interferences. Fringes are produced by two partially or totally superimposed pupil images created by introducing a beam splitter. At each point, interference occurs from the combination of only two points on the wave fronts at a given baseline and therefore behaves as an array of Michelson-Fizeau interferometers. An important property of these interferometers is their ability to work with partially coherent light, which offers a better S/N ratio on bright sources and is insensitive to calibration errors due to seeing fluctuations and telescope aberrations. A rotational shear interferometer was used at the telescope to map the visibility of fringes produced by α Ori (Roddier and Roddier, 1988). In this technique, the 2D Fourier transform is obtained by rotating one pupil image about the optical axis by a small angle with respect to the other. If the rotation axis coincides with the center of the pupil, the two images overlap. All the object Fourier components within a telescope's diffraction cutoff frequency are measured simultaneously.

2. Phase-closure methods

The phase of the visibility may be deduced from a closure phase that is insensitive to atmospherically induced random phase errors as well as to the permanent phase errors introduced by the imaging systems (Jennison, 1958) using three telescopes. The observed phases ψ_{ij} on the different baselines contain the phases of the source Fourier components $\psi_{0,ij}$ and also the error terms θ_j, θ_i, introduced by errors at the individual antennas and by atmospheric variations at each antenna. The observed fringes are represented by the following equations:

$$\psi_{12} = \psi_{0,12} + \theta_2 - \theta_1, \tag{87}$$

$$\psi_{23} = \psi_{0,23} + \theta_3 - \theta_2, \tag{88}$$

$$\psi_{31} = \psi_{0,31} + \theta_1 - \theta_3, \tag{89}$$

where the subscripts refer to the antennae at each end of a particular baseline. The closure phase β_{123} is the sum of phases of the source Fourier components and is derived as

$$\beta_{123} = \psi_{12} + \psi_{23} + \psi_{31} \tag{90}$$

$$= \psi_{0,12} + \psi_{0,23} + \psi_{0,31}. \tag{91}$$

This equation implies cancellations of the antennae phase errors. Using the measured closure phases and amplitudes as observables, one is able to determine the object phases (mostly by least-squares techniques, viz., singular value decomposition or the conjugate gradient method). From the estimated object phases and the calibrated amplitudes, the degraded image is reconstructed.

Baldwin *et al.* (1986) reported measurements of the closure phases obtained at a high light level with a three-hole aperture mask set in the pupil plane of the telescope. The nonredundant aperture masking method, in which the short-exposure images are taken through a multiaperture screen, has several advantages: (i) an improvement of S/N ratios for the individual visibility and closure-phase measurements, (ii) attainment of the maximum possible angular resolution by using the longest baselines, and (iii) built-in delay to observe objects at low declinations. But the system is restricted to high

light levels, because the instantaneous coverage of spatial frequencies is sparse and most of the available light is discarded.

3. Phase-diversity imaging

Phase-diversity imaging (Gonsalves, 1982; Paxman *et al.*, 1992) is a postcollection technique that uses a number of intensity distributions encoded by known aberrations for restoring high spatial resolution detail while imaging in the presence of atmospheric turbulence. The phase aberrations are estimated from two simultaneously recorded images. Phase-diverse speckle interferometry is an extension of this technique, whereby a time sequence of short-exposure image pairs is detected at different positions in and out of focus near the focal plane. Incident energy is split into two channels by a simple beam splitter: one is collected at a conventional focal plane, the other is defocused (by a known amount) and a second detector array permits the instantaneous collection of the latter. It is less susceptible to the systematic errors caused by the optical hardware and is found to be more appealing in astronomy (Baba, Tomita, *et al.*, 1994; Seldin and Paxman, 1994).

C. Adaptive optics

Significant technological innovations over the past several years have made it possible to correct perturbations in wave fronts in real time by incorporating a controllable phase distortion in the light path opposite to that introduced by the atmosphere (Babcock, 1953; Rousset *et al.*, 1990). This technique has advantages over postdetection image restoration techniques that are limited by noise. Adaptive optics (AO) systems are employed in other branches of physics as well. Liang *et al.* (1997) constructed a camera equipped with adaptive optics that allows one to image a microscopic single cell in the living human retina. They showed that a human eye with adaptive optics correction can resolve fine gratings that are invisible to the unaided eye. AO systems are useful for spectroscopic observations, as well as for low-light-level imaging with future very large telescopes and ground-based long-baseline optical interferometers.

1. Greenwood frequency

Turbulence cells are blown by wind across the telescope aperture; hence the wind velocity dictates the speed with which a corrective action must be taken. Greenwood (1977) derived the mean-square residual wave-front error as a function of servo loop bandwidth for a first-order controller, which is given by

$$\sigma_{cl}^2=\left(\frac{f_G}{f_{3db}}\right)^{5/3} rad^2, \tag{92}$$

where f_{3db} is the closed-loop bandwidth of the wave-front compensator and f_G is the Greenwood frequency defined by the relation

$$f_G=\frac{0.426v}{r_0}, \tag{93}$$

where v is the wind velocity in the turbulent layer of air. For imaging in the near-IR to ultraviolet, the AO system bandwidths need to have a response time on the order of several hundred to 1000 Hz. It is easier to achieve diffraction-limited information using AO systems at longer wavelengths, since r_0 is proportional to the six-fifths power of the wavelength,

$$r_0 \propto \lambda^{6/5}. \tag{94}$$

The above equation implies that the width of seeing-limited images, $1.22\lambda/r_0 \propto \lambda^{-1/5}$, varies with λ. The number of degrees of freedom, i.e., the number of actuators on the deformable mirror and the number of subapertures in the wave-front sensor, in an AO system should be determined by the following equation:

$$(D/r_0)^2 \propto \lambda^{-12/5}. \tag{95}$$

2. Adaptive optics imaging systems

The required components for implementing an AO system are wave-front sensing, wave-front phase error computation, and a flexible mirror whose surface is electronically controlled in real time to create a conjugate surface enabling compensation of the wave-front distortion (Roggemann *et al.*, 1997, and references therein). In order to remove the low-frequency tilt error, the incoming collimated beam is generally fed by a tip-tilt mirror. After traveling further, it reflects off a deformable mirror that eliminates high-frequency wave-front errors. A beam splitter divides the beam into two parts: one is directed to the wave-front sensor to measure the residual error in the wave front and to provide information to the actuator control computer to compute the deformable mirror actuator voltages, and the other is focused to form an image.

Use of a tip-tilt mirror system in conjunction with closed-loop control electronics has several advantages: (i) conceptually, the system is simple, (ii) fainter guide stars increase the sky coverage, and (iii) the field of view is wider (Glindemann, 1997). These systems are limited to two Zernike modes (x and y tilt), while a higher-order system compensating for many Zernike[1] modes is required to remove high-frequency errors.

A variety of deformable mirrors has been developed for the applications of (i) high-energy laser focusing, (ii) laser cavity control, (iii) compensated imagery through atmospheric turbulence, etc. Several wave-front sensors such as (i) the lateral shearing interferometer, (ii) the Shack-Hartman sensor, and (iii) the curvature sensor are in use as well. The technical details of these deformable

[1]Zernike polynomials are an orthogonal expansion over the unit circle.

mirrors and sensors are enumerated in the recent literature (Roggemann *et al.*, 1997; Roddier, 1999; Saha, 1999).

Phase reconstruction method can be categorized as being either zonal or modal, depending on whether the estimate is a phase value in a local zone or a coefficient of an aperture function (Rousset, 1999). In the case of curvature sensing, the computed sensor signals are multiplied by a control matrix to convert wave-front slopes to actuator control signals, the output of which are the increments to be applied to the control voltages on the deformable mirror. A conjugate shape is created on the mirror using these data.

The real-time computation of the wave-front error, as well as correction of wave-front distortion, involves digital manipulation of data in the wave-front sensor processor, the reconstructor, and the low-pass filter; the output is converted to analog drive signals for the deformable mirror actuators. The functions are (i) to compute subaperture gradients, phases at the corners of each subaperture, and low-pass filter phases, and (ii) to provide actuator offsets to compensate for the fixed optical system errors and wave-front distortions.

3. Artificial source

An AO system requires a reference source for measuring wave-front errors, as well as for mapping the phase on the entrance pupil. It is generally not possible to find a sufficiently bright reference star close enough to a target star. In order to get around this limitation, many observatories are currently using artificial laser guide stars (Racine *et al.*, 1996; Ragazzoni and Bonnacini, 1996; Lloyd-Hart *et al.*, 1998). However, the best results are still obtained with natural guide stars.

An artificial guide star can be obtained using either resonance scattering by sodium in the mesosphere at 90 km (Foy and Labeyrie, 1985) or Rayleigh scattering between 10 and 20 km in altitude (Fugate *et al.*, 1994). A pulsed laser (tuned to the sodium D_2 line to excite sodium atoms) is used to produce a bright compact glow in the upper atmosphere. Concerning the flux backscattered by a laser shot, Thompson and Gardner (1988) stressed the importance of investigating two basic problems: (i) the cone effect, which arises due to the parallax between the remote astronomical source and the artificial source, and (ii) angular anisoplanar effects. These effects can be restored by imaging the various turbulent layers of the atmosphere onto different adaptive mirrors (Tallon *et al.*, 1988). Scattering of the upward propagating laser beam is due to Rayleigh scattering, mostly by N_2 molecules. Mie scattering by aerosol or cirrus clouds may be important at lower altitudes but is usually variable and transient.

4. Multiconjugate adaptive optics

A multiconjugate AO system makes possible near-uniform compensation for the atmospheric turbulence over a considerably larger field of view than can be corrected with a normal AO system. This method employs an ensemble of guide stars that allows for 3D tomography of the atmospheric turbulence and a number of altitude-conjugate deformable mirrors to extend the compensated field of view. However, its performance depends on the quality of the wave-front sensing of the individual layers. Ragazzoni *et al.* (2000) have demonstrated this type of tomography. This new technique pushes the detection limit by $\sim$1.7 mag on unresolved objects with respect to seeing-limited images; it also minimizes the cone effect. It will be useful for the extremely large telescopes of the 100-m class, e.g., the Overwhelmingly Large (OWL) Telescope (Dierickx and Gilmozzi, 1999). However, it has some limitations, mainly related to the finite number of actuators in deformable mirrors, wave-front sensors, and guide stars.

5. Adaptive secondary mirrors

The use of an adaptive secondary mirror for corrections may soon make obsolete the kind of relay optics that are required to conjugate a deformable mirror at a reimaged pupil, as well as to minimize thermal emission (Bruns *et al.*, 1997). Notable advantages of the second mirror are (i) enhanced photon transmission through an optical setup, (ii) introduction of negligible extra IR emissivity, (iii) creation of no extra polarization, and (iv) nonaddition of reflective losses (Lee *et al.*, 2000). Due to the interactuator spacing, the resonant frequency of such a mirror may be lower than the AO bandwidth. The adaptive secondary mirror system uses a Shack-Hartman sensor with an array of small lenslets, which adds two extra refractive surfaces to the wave-front sensor optical beam (Lloyd-Hart, 2000). An *f*/15 AO secondary with 336 actuators is in the final stages of testing and will be installed on the 6.5-m telescope of the Multiple Mirror Telescope (MMT) Observatory, Mt. Hopkins, Arizona in 2002 (Wehinger, 2001).

6. High-resolution coronagraphy

A coronagraph is used in imaging or spectroscopy of a faint structure near a bright object. Its purpose is to reduce the light coming from the central star and filter out the light at low spatial frequency; the remaining light at the edge of the pupil corresponds to high frequencies. A coronagraph reduces off-axis light from an on-axis source with an occulting stop in the image plane as well as with a matched Lyot stop in the next pupil plane. While using the former stop, one chooses the size of the latter pupil with some care to find the best tradeoff between the throughput and image suppression. The limitations come from the light diffracted by the telescope and instrument optics. Coronagraphy with dynamic range can be a powerful tool for direct imaging of extrasolar planets. Nakajima (1994) estimates that imaging with such a method using a low-order AO system in a 6.5-m telescope could detect Jupiter-size extrasolar planets at separation of $\sim$1.5 arcsec with a S/N ratio of 3 in 10^4 s. Rouan *et al.* (2000) describe a four-quadrant

phase-mask coronagraph in which a detection at a contrast of more than 8-mag difference between a star and a planet is feasible.

D. Dark speckle method

The dark speckle method uses the dark zones between speckles—"dark speckles." It exploits the light cancellation effect in a random coherent field; highly destructive interferences that appear near black spots in the speckle pattern (Labeyrie, 1995) may occur occasionally. The aim of this method is to detect faint objects around a star when the difference of magnitude is significant. If a dark speckle is at the location of the companion in the image, the companion emits enough light to reveal itself.

The required system consists of a telescope with an AO system, a coronagraph, a Wynne corrector, and a fast photon-counting camera with low dark noise. If a pixel of the photon-counting camera is illuminated by the star only (in the Airy rings area), the number of photons in each pixel for a given interval (frame) is statistically given by a Bose-Einstein distribution. The number of photons per frame in the central peak of the image of a point source obeys a classical Poisson distribution. For the pixels containing the image of the companion, the number of photons, resulting from both the star and the companion, is given by a different distribution (computed by mixing Bose-Einstein and Poisson distributions). One noticeable property is that the probability of getting zero photons in a frame is very low for the pixels containing the image of the companion, and much higher for the pixels containing only the contribution from the star. Therefore, if the "no photon in the frame" events for each pixel are counted for a very large number of frames, a *dark map* can be built that will show the pixels for which the distribution of the number of photons is not of the Bose-Einstein type, therefore revealing the location of a faint companion. The role of the Wynne corrector is to give residual speckles the same size regardless of wavelength. Otherwise, dark speckles at a given wavelength would be overlapped by bright speckles at other wavelengths. With the current technology, using the dark speckle technique at a 3.6-m telescope should allow detection of a companion with $\Delta m_k \approx 6-7$ mag. Figures 5 and 6 depict coronagraphic images of the binary stars HD192876 and HD222493, respectively (Boccaletti *et al.*, 2001); the data were obtained with the Adaptive Optics Near Infrared System (ADONIS) in the K band (2.2 μm) on the European Southern Observatory's (ESO) 3.6-m telescope. Due to the lack of a perfect detector (no readout noise) in the near-IR band, every pixel under the defined threshold (a few times the readout noise) is accounted as a dark speckle.

Phase boiling, a relatively new technique that consists of adding a small amount of white noise to the actuators in order to get a fast temporal decorrelation of the speckles during long-exposure acquisition, may produce better results. Aime (2000) computed the S/N ratio for two different cases: short exposure and long exposure. According to him, even with an electron-noise-limited detector like a charge-coupled device (CCD) or a near-IR camera multiobject spectrometer (NICMOS), phase boiling can provide better results if the halo has its residual speckles smoothed by fast residual "seeing" during the long exposure than by building a dark map from short exposures in the photon-counting mode. Artificial very fast seeing can also be generated by applying fast random noise to the actuators at amplitude levels comparable to the residual seeing left over by the AO system.

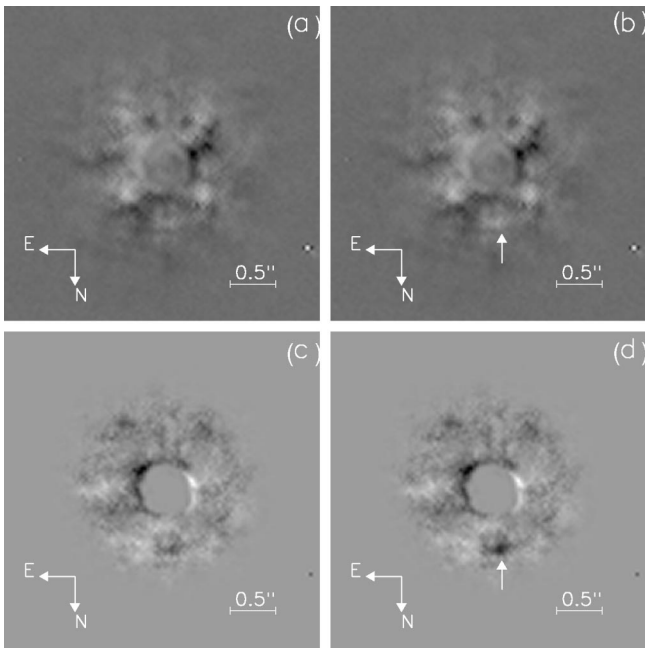

FIG. 5. Coronagraphic images of the star HD192876. An artificial companion was added to the data to assess the detection threshold ($\Delta m_K = 6.0$ mag, $\rho = 0.65$ arcsec): (a) direct image: addition of four hundred 60-ms frames; (b) the same image with a $\Delta m_K = 6.0$ mag companion (S/N ratio = 1.8); (c) dark speckle analysis; (d) dark speckle analysis with the companion (S/N ratio = 4.8); the detection threshold on that image is about $\Delta m_K = 7.5$ mag, an improvement of 1.5 mag over the direct image. From Boccaletti *et al.* (2001), courtesy A. Boccaletti.

The question is, what is easiest: dark speckle analysis or a "hyperturbulated" long exposure? Labeyrie (2000) made simulations supporting Aime's (2000) results. Boccaletti (2001) compared the dark speckle S/N ratio with the long-exposure S/N ratio (Angel, 1994). The speckle lifetime has to be of order 0.1 ms. Currently, it is impossible to drive a deformable mirror at this frequency (10 kHz). With the 5-m Palomar telescope Boccaletti (2001) tried to smooth the speckle pattern by adding straightforward random noise to the actuators (the deformable mirror is equipped with 241 actuators) at a maximum speed of 500 Hz. Effectively, the halo was smoothed, but its intensity also increased, so that the companion S/N ratio actually decreased. Blurring the speckle pattern would probably require wave-front sensor telemetry;

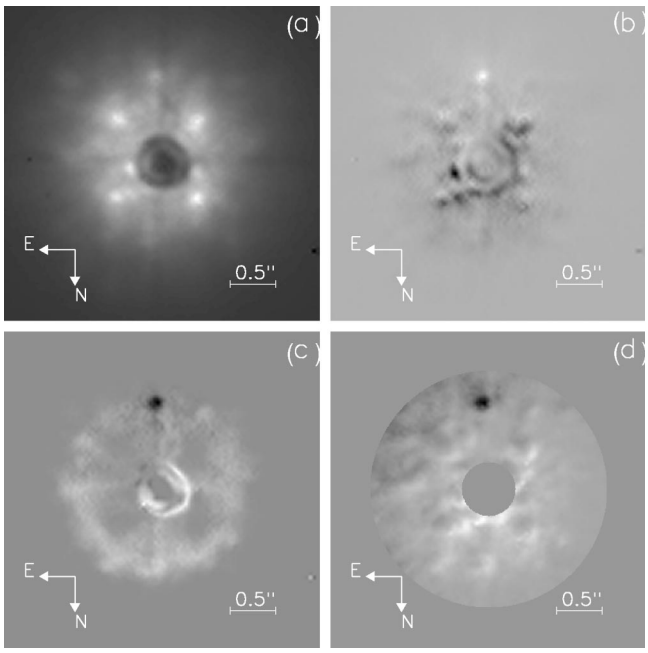

FIG. 6. Coronagraphic images of the binary star HD222493 ($\Delta m_K = 3.8$ mag, $\rho = 0.89$ arcsec); (a) direct image: addition of six hundred 60-ms frames; (b) subtraction of a reference star from the direct image (S/N ratio = 14.6); (c) dark speckle analysis (constant threshold) and subtraction of a reference star; (d) dark speckle analysis (radial threshold) and subtraction of a reference star (S/N ratio = 26.7). From Boccaletti *et al.* (2001), courtesy A. Boccaletti.

implementation of a hyperturbulated long exposure at the Palomar is still under study (Boccaletti, 2001).

E. High-resolution sensors

All the techniques described above require a high-quality sensor to enable one to obtain snapshots with a very high time resolution of the order of (i) frame integration of 50 Hz, or (ii) photon-recording rates of a few megahertz. The performance relies on the characteristics of such sensors, e.g., (i) the spectral bandwidth, (ii) the quantum efficiency, (iii) the detector noise, including dark current, readout and amplifier noise, (iv) the time lag due to the readout of the detector, and (v) the array size and the spatial resolution.

1. Frame-transfer camera systems

The frame-transfer intensified CCD camera employs a *microchannel plate* as an intensifier. The photoelectron is accelerated into a channel of the microchannel plate, releasing secondaries and producing an output charge cloud of about 10^3–10^4 electrons with 5–10 kV potential. With further applied potential of ~5–7 kV, these electrons are accelerated to impact a phosphor, thus producing an output pulse of $\sim 10^5$ photons. These photons are directed to the CCD by fiber-optic coupling. The main disadvantage of such a system is that the poor gain statistics result in the introduction of a noise factor between 2 and 3.5. Recent development of a nonintensified CCD device that effectively reduces readout noise to less than one electron rms has enabled substantial internal gain within the CCD before the signal reaches the output amplifier (Mackay *et al.*, 2001). Such a detector, although the photon-counting performance appears moderate for the moment, shows promise for quantitative measurement of diffraction-limited stellar images.

2. Photon-counting detectors

The marked advantage of a photon-counting system is that of reading the signal *a posteriori* to optimize the correlation time of short exposures in order to overcome the loss of fringe visibility due to the speckle lifetime. The typical values for an object of $m_v = 12$ over a field of 2.5 arcsec are less than 50 photons/ms through a narrow-band filter. The other notable features are (i) the ability to determine the position of a detected photon, (ii) the ability to register individual photons with equal statistical weight and to produce a signal pulse (with a dead time of a few ns), and (iii) low dark noise.

The major shortcomings of a photon-counting system based on frame integration (Blazit, 1986) arise from (i) calculations of the coordinates which are hardware limited, and (ii) the limited dynamic range of the detector. Nondetectability of a pair of photons closer than a minimum separation by the detector yields a loss in high-frequency information; this, in turn, produces a hole in the center of the autocorrelation—a Centreur hole—resulting in degradation of the power spectra or bispectra (triple correlation Fourier transform) of speckle images.

Several 2D photon-counting sensors that allow recording of the position and time of arrival of each detected photon have been developed, such as (i) the precision analog photon address (PAPA; Papaliolios *et al.*, 1985), (ii) the resistive anode position detector (Clampin *et al.*, 1988), (iii) the multi-anode microchannel array (MAMA; Timothy, 1993), (iv) the wedge-and-strip anode, (v) the delay-line anode, (vi) the silicon anode detector, etc. Except for PAPA, which is based on a high-gain image intensifier and a set of photomultiplier tubes, these sensors detect the charge cloud from a high-gain microchannel plate. They provide spatial event information by means of a position-sensitive readout setup; the encoding systems identify each event's location. The shortcomings of the microchannel plates are due notably to its local dead time, which essentially restricts the conditions for use of these detectors to high-spatial-resolution applications. These constraints are also related to the light intensity and the pixel size.

3. Infrared sensors

In the infrared band, no photon counting is possible with the current technology. Nevertheless, a near-IR focal-plane array, NICMOS, has been developed. It consists of 256×256 integrating detectors organized in four independent 128×128 quadrants and is fabricated in HgCdTe grown on a sapphire substrate that is very rugged and provides a good thermal contraction match to

the silicon multiplexer (Cooper *et al.*, 1993). The typical NICMOS3 focal-plane arrays have read noise less than 35 electrons with less than 1 electron/sec detector dark current at 77 K, and their broadband quantum efficiency is better than 50% in the range of 0.8–2.5 μm.

V. DILUTE-APERTURE INTERFEROMETRY

Modern technology has solved many of the problems that were first encountered by Michelson and Pease (1921). The light collected by an array of separated telescopes can be coherently combined to measure the Fourier components of the brightness distribution of a star. The following subsections elucidate the current state of the art of such arrays, which are at an interesting stage of development, though still limited in their imaging capabilities.

A. Aperture-synthesis interferometry

The potential of aperture-synthesis interferometry in the optical domain is demonstrated by the spectacular images produced by aperture masking of a single telescope (Tuthill *et al.*, 2000). This method is an extension of the same principle as the operation of a conventional filled-aperture telescope composed of N elemental areas, in which there are $N(N-1)/2$ independent baselines, with $N-1$ unknown phase errors. By using many telescopes in an interferometric array, most of the phase information can be retrieved. The signal in the nth area due to a source of emission is expressed as

$$V_n = a_n \cos(\omega t + \psi_n), \tag{96}$$

where a_n is the amplitude of the signal and ψ_n the relative phase of the radiation. If these signals are added together vectorially and time averaged, the intensity of the light $\mathcal{I}_n$ is derived as

$$\begin{aligned}\mathcal{I}_n &\propto \frac{1}{2}\sum_{j=1}^{N}\sum_{k=1}^{N} a_j a_k \cos(\psi_j - \psi_k) \\ &= \frac{1}{2}\sum_{j=1}^{N} a_j^2 + \sum_{j=1}^{N-1}\sum_{k=j+1}^{N} a_j a_k \cos(\psi_j - \psi_k).\end{aligned} \tag{97}$$

The first term is proportional to the sum of the power received by the elemental areas. The resolving power is derived from the cross product. Each term can equally be measured with two elemental areas in positions j and k. The term $\psi_j - \psi_k$ is expressed as

$$\psi_j - \psi_k = \frac{2\pi}{\lambda}\,\mathbf{B}_{jk}\cdot\mathbf{s}, \tag{98}$$

where $\mathbf{B}_{jk}$ is the separation of the two elemental areas, and $\mathbf{s}$ is the unit vector pointing toward the source.

1. Aperture-synthesis imaging

Generally, three or more telescopes are required for aperture synthesis, though two can suffice if the object includes a point source usable as a phase reference. Different spectral channels are employed for differential visibility measurements. One may use data from one part of the spectrum, such as the continuum emission, to calibrate another part, such as a spectral line (Mourard *et al.*, 1989). The continuum channel is thought to originate from the unresolved region of a star, e.g., the photosphere, and the spectral line centered on a part of the spectrum is thought to be created in an extended region, such as the circumstellar medium. The phase-referenced technique with a fringe-tracking channel was also used at the Mark III Interferometer to recover phase information (Quirrenbach *et al.*, 1996). Another convenient method is to measure the instantaneous phases of fringes from a bright point source that lies within the isoplanatic patch in order to correct the corrupt phases on the target. Shao and Colavita (1992) used fringe-phase information to determine the precise relative positions of nearby stars.

The direct measurements of the closure phase together with the measurements of visibility amplitude allow one to reconstruct an image of any object using three or more independent telescopes. This technique was successfully demonstrated by Baldwin *et al.* (1998) in the visible band at the Cambridge Optical Aperture Synthesis Telescope (COAST). Each pair of telescopes in an array yields a measure of the amplitude of the spatial coherence function of the object at a spatial frequency $\mathbf{B}/\lambda$ where $\mathbf{B}$ is the baseline vector. In order to make an image from an interferometer, one needs estimates of the complex visibilities over a large portion of the (u,v) plane, both the amplitudes and phases. The (u,v) coordinates corresponding to a snapshot projection of the baseline that are sampled from a star of declination δ_*, when its hour angle is H, are given by (Fomalont and Wright, 1974)

$$u = (\mathrm{B}'_{EW}\cos H - \mathrm{B}'_{NS}\sin\theta_l \sin H)/\lambda, \tag{99}$$

$$\begin{aligned}v = [&\mathrm{B}'_{EW}\sin\delta_* \sin H + \mathrm{B}'_{NS}(\sin\theta_l \sin\delta_* \cos H \\ &+ \cos\theta_l \cos\delta_*)]/\lambda,\end{aligned} \tag{100}$$

where B'_{EW} and B'_{NS} are orthogonal east-west and north-south components, respectively, of the baseline vector at the ground of an interferometer located at the terrestrial latitude θ_l.

2. Astrometry

The accurate determination of relative positions of stars will provide crucial data for astrophysics. For example, precise parallax distances of Cepheids will help to establish a period/absolute magnitude relationship in order to calibrate distances of galaxies, thus reducing the uncertainty on the value of the Hubble constant (H_0). An interferometer measures the angle projected onto the baseline. Stellar fringes must be observed at two or more baseline orientations to determine two angular coordinates of an astronomical object. The Hipparcos catalog (Hipparcos, 1997) uses the phase-shift measurement of the temporal evolution of the photometric level of two stars seen drifting through a grid.

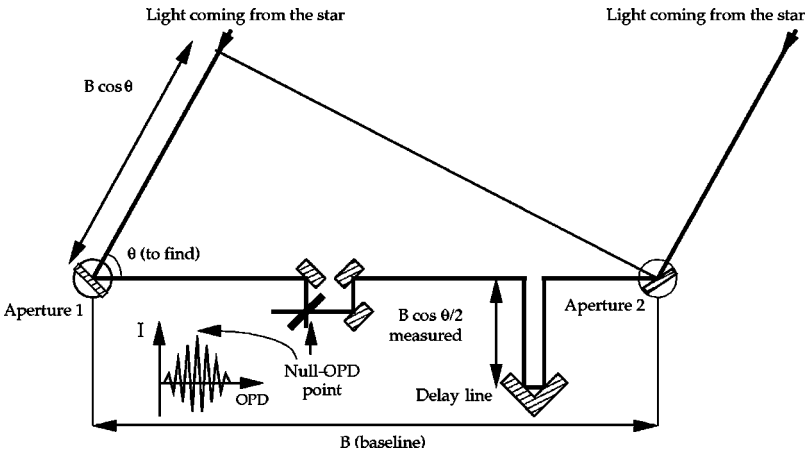

FIG. 7. Schematic representation of an interferometer for astrometry. From Saha and Morel (2000).

For a two-aperture interferometer (see Fig. 7) the external optical delay d, while an object with angle θ is observed in a broad spectral range (i.e., white light), is

$$d = |\mathbf{B}| \times \cos\theta. \tag{101}$$

This delay can be determined from the position of the optical delay line of an instrument set up such that the central fringe of the interference pattern appears in a narrow observation window. The position, as well as $|\mathbf{B}|$, is measured by laser metrology. Hence θ is deduced with high precision. For ground-based interferometers, the baseline is fixed to the Earth and will rotate with the Earth, while in space the interferometer must reorient the baseline to measure both angular coordinates. For a space-borne interferometer, the issue is to find a reference for the angle measured. Usually, a grid of far objects like quasars is used as a reference frame. There are two modes of observation possible: the "wide-angle" and the "narrow-angle" modes. In wide-angle mode, the large angle difference between the reference and the studied object usually requires collector motions. In narrow-angle mode, the two objects are in the field of view of the instrument; therefore, no motions are required and the accuracy of the measurement is improved. However, it is difficult always to have a correct reference star within the field of view for any studied object. Narrow-angle astrometry is, therefore, more suitable for wobble characterization.

3. Nulling interferometry

Nulling interferometry was first proposed by Bracewell (1978) for applications in radio astronomy. Such an interferometer could be employed at the upcoming large interferometers to observe faint structures close to nonobscured central sources. This technique can also be used in space to search for extrasolar Earthlike planets through their thermal emission and to determine by spectroscopic analysis whether they have atmospheres that might support life (Angel *et al.*, 1986; Hinz *et al.*, 1998). Here the light collected by two apertures is combined to generate a deep destructive interference fringe at the stellar position, thus selectively nulling the star by many orders of magnitude compared to the surrounding off-axis environs, such as a planetary system. Basically, a π phase shift is introduced in one wave-front segment, so that when it interferes with another segment of the same wave front, perfect cancellation is achieved. Therefore the central fringe of the interference pattern is dark, allowing the fringe pattern from a faint object to appear. In contrast to a coronagraph, with which useful imaging is possible beyond several Airy radii from the on-axis stellar source, this method is expected to be effective within the core of a telescope's point-spread function, and so can be employed for stars at greater distances, where a larger sample is available (Serabyn, 2000). The quality of a nulling is defined by the "null depth" N_d,

$$N_d = (1 - \mathcal{V}\cos\varphi_e)/2 \approx (\pi\sigma_{\Delta\psi}/\lambda)^2, \tag{102}$$

where φ_e is the phase error between the two recombined beams, $\mathcal{V}$ the fringe visibility modulus, and $\sigma_{\Delta\psi}$ the standard deviation of the optical path difference (OPD) between the two beams.

To create the π phase shift, these are two important techniques that may be used, (i) using roof reflectors to achieve a reversal of sign of the electric vector, and (ii) introducing a precise thickness of glass whose index acts to retard all wavelengths by very nearly one-half wavelength. Serabyn (2000) reported satisfactory nulling results obtained with a fiber-coupled rotational shearing interferometer in visible wavelengths. Hinz *et al.* (1998) demonstrated the viability of nulling interferometry using two 1.8-m mirrors of the original six-mirror Multiple Mirror Telescope (MMT). They detected the thermal image of the circumstellar dust nebula around α Ori. Hinz *et al.* (2001) measured the spatial extent of the mid-IR emission for a few Herbig Ae stars as well. Figure 8 depicts the schematic of the nulling interferometer at the MMT (Hinz *et al.*, 1998).

B. Fundamental limitations and technical challenges

Atmospheric seeing affects the measurements of fringe visibility by introducing phase aberrations across the wave fronts incident on the interferometer. The relative phase of the wave fronts at the apertures changes with time, and also varies the optical paths through the arms. Fringes need to be obtained over a time scale as

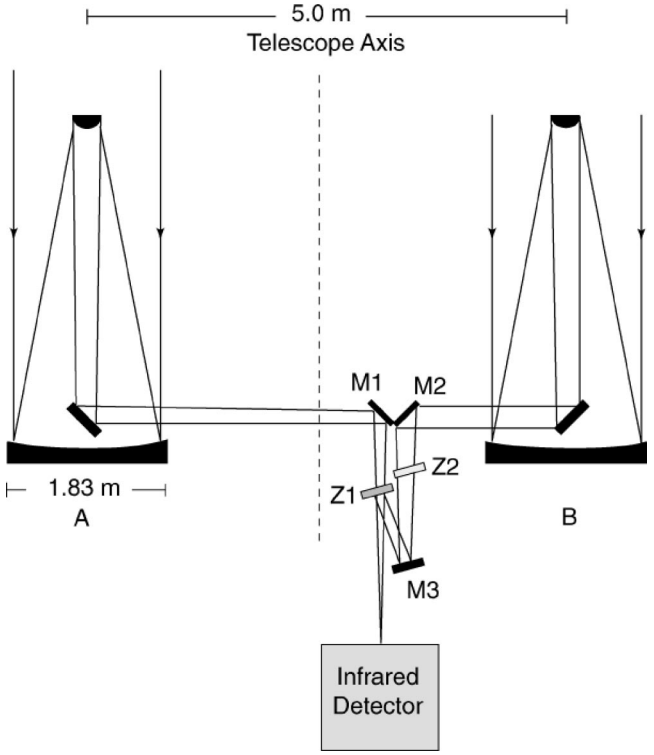

FIG. 8. Schematic of the nulling interferometer at the Multiple Mirror Telescope. The wave fronts from the two comounted telescopes A and B are translated via three mirrors, M1, M2, and M3, for superposition without relative rotation or tilt. The zinc selenide beam splitters Z1 and Z2 are used to adjust the path length. From Hinz *et al.* (1998), courtesy P. M. Hinz.

short as that of atmospheric fluctuations ($\sim$0.01 s). Optical interferometers require accurate alignments, high stability, and full control of any effect decreasing visibility. These challenges must be met in order to achieve the aims of interferometry, viz., (i) precise determination of visibility, (ii) sensitivity in measuring weak sources, (iii) accurate measurement of fringe phases, and (iv) availability of a range of baselines.

1. Signal-to-noise ratio

The S/N ratio with which the visibility can be measured is a function of $N_p'\mathcal{V}^2$. The fringe S/N ratio is given by the expression (Lawson, 1995)

$$\mathrm{S/N} \propto \frac{N_p'\mathcal{V}^2}{\sqrt{1+0.5\times N_p'\mathcal{V}^2}}, \tag{103}$$

where N_p' is the number of photons detected per subaperture per integration time.

The dependence on $N_p'\mathcal{V}^2$ implies that interferometry becomes increasingly difficult for faint sources, particularly for those with complex structures. The $N_p'\mathcal{V}^2$ limit can be addressed in various ways, viz., (i) using larger subapertures, (ii) slicing of the image at the entrance of the spectrograph, (iii) bootstrapping, and (iv) tracking fringes on a point source to increase integration time on the target.

2. Delay lines

The real art of developing interferometers is to combine the beams in phase with each other after they have traversed exactly the same optical path from the source through each telescope down to the beam combination point. The path lengths of the two arms need to be equalized and maintained to a fraction of $c/\Delta\nu$. A correct determination of **B** that is unstable over time is also necessary; the situation becomes complicated in the presence of atmosphere. The paths are made equal by adjusting the position of mirrors in the optical delay line, which corrects the drift induced by the diurnal rotation of the tracked star. Of course, the difficulty is to avoid various aberrations and vignetting, particularly when light is fed through long and narrow pipes. The optical delay in terms of telescope and source parameters translates into

$$d = \mathrm{B}'_{EW}\cos\delta_*\sin H - \mathrm{B}'_{NS}(\sin\theta_l\cos H\cos\delta_* - \cos\theta_l\sin\delta_*). \tag{104}$$

Until recently, the beam-recombining optical devices at both the Interféromètre à Deux Télescopes (I2T) and the Grand Interféromètre à Deux Télescopes (GI2T; Labeyrie, Schumacher, *et al.*, 1986) were kept on a computer-controlled motor-driven carriage parallel to the baseline in order to compensate for the OPD. Of late, a delay line that is movable has been inserted in one of the arms of the I2T by means of a cat's-eye system; the other arm has been equipped with a fixed delay line (Robbe *et al.*, 1997). The present recombiner at GI2T, the Recombinateur pour Grand Interféromètre (REGAIN), also uses a delay line featuring a cat's-eye reflector with a variable-curvature mirror.

A few interferometers, viz., the Mark III Stellar Interferometer (Shao *et al.*, 1988), the US Navy Prototype Optical Interferometer (NPOI; Armstrong *et al.*, 1998), and the Infrared Optical Telescope Array (IOTA; Carleton *et al.*, 1994), use vacuum delay lines. The Mark III Interferometer delay line used laser interferometers to measure the position of the delay line carts and nested servo loops for fine control of the OPD. The delay lines of IOTA include a "long" one with a 28-m travel so that the cart can be moved each time a new object is observed, when the OPD to compensate is very different. It does not move during fringe acquisition. IOTA also has a second "short" delay line of about 2-m travel, which tracks the sidereal motion during fringe acquisition. Both delay lines use a dihedral (two plane mirrors at 90°) mounted on a carriage. For the long delay line, the carriage is moved by a pulley-and-cable system powered by a stepper motor, while for the short delay line, a linear motor system allows precise motion of the carriage (10-nm steps). For both delay lines, measurement of the carriage position is carried out by a laser metrology system using the Doppler-Fizeau effect of a laser beam sent to the carriage and bounced back (Morel, 2000).

Another method known as group-delay tracking, based on the integration of the moduli of all the com-

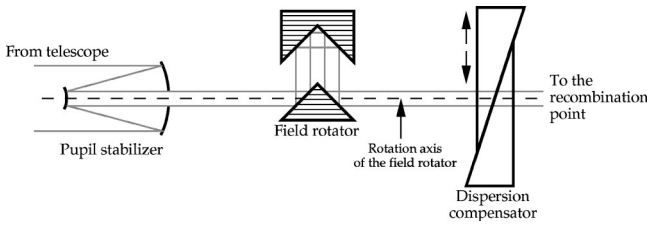

FIG. 9. Optical processing of a beam from one arm of the Grand Interféromètre à Deux Télescopes (GI2T) by the Recombinateur pour Grand Interféromètre (REGAIN) recombiner. From Saha and Morel (2000).

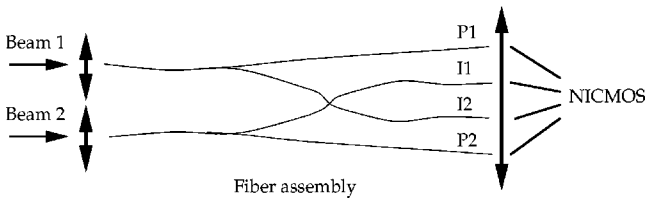

FIG. 10. Schematic of the Fiber Linked Unit for Optical Recombination (FLUOR). P1 and P2 are the photometric output fibers. I1 and I2 are the interferometric output fibers. These outputs are imaged by a lens on a near-infrared multiobject spectrometer (NICMOS). From Saha and Morel (2000).

puted Fourier transforms (Lawson, 1994; Lawson *et al.*, 1998), is used with the interferometers SUSI and COAST. The group delay is proportional to the rate of change of phase as a function of wave number, evaluated at the center of the band. This delay can be measured if the combined beams from an interferometer are dispersed in a spectrometer. The group-delay tracking yields a peak whose position is proportional to the optical path difference.

3. Beam recombination

Fringes can be obtained either by utilizing the concept of merging speckles (Labeyrie, 1975) or by employing a pupil-plane configuration (Tango and Twiss, 1980). At the initial stage, the beam-recombining optics that were employed at both I2T and GI2T consisted of (i) a recombining element for reconfiguring the pupil and fixing the fringe spacing, (ii) an image slicer (a series of 10 wedges of different angles cemented on a field lens, which slice the image), (iii) the compensating system for atmospheric dispersion, (iv) gratings (with a maximum spectral resolution of 0.15 nm), and (v) detectors to record the fringes. The advantages of the dispersion mode are the capabilities of (i) allowing continuous observation of fringes across the spectral bandwidth, (ii) recording the fringes with longer integration time, and (iii) selecting different spectral channels for differential visibility measurements. In the REGAIN combiner, each Coudé beam coming from the telescopes meets a pupil stabilizer, a field rotator, a wedge prism, and the beam combiner (Rousselet-Perraut *et al.*, 1996). Figure 9 depicts the process performed by an arm of the REGAIN table prior to recombination.

Interferometers with multiple apertures, such as COAST, use a multistage four-way combiner. Light from the telescopes is first combined in pairs. These pairs are recombined with other pairs. Each detector sees light from all of the telescopes. Another method known as the pairwise recombination technique is employed at NPOI, where a beam combiner uses a different detector for each baseline.

a. Fiber-linked recombination

Fiber-optic recombiners provide a perfect spatial filtering of turbulence-induced corrugated wave fronts, much reducing the contribution variations. They offer several advantages, allowing one to (i) select the plane-wave part of a wave front, (ii) split a guided wave into any desired intensity ratio, and (iii) combine two guided waves interferometrically. The Fiber Linked Unit for Optical Recombination (FLUOR) at IOTA is able to calibrate visibilities with sub-1% precision, which is important for many astrophysical applications like stellar atmospheres studies, Cepheid pulsation measurements for distance determinations, and detection of angular anisotropies arising in disks around young stars.

Fiber delay lines, using spools of fiber that can be stretched or relaxed to increase or decrease the optical path length, are used in FLUOR. These fibers have been designed to propagate infrared light at near-IR (Mennesson *et al.*, 1999) in transverse electromagnetic mode, like a coaxial cable. Therefore only plane waves perpendicular to the axis of the fiber may propagate over a long distance. Basically, this method results in a "spatial filtering," thus smoothing the wave front. The advantage of such a method for interferometry is a reduction of the uncertainty on the measured visibility, and the drawbacks are the loss of optical coupling efficiency and larger photometric variations due to the turbulence. Figure 10 depicts the schematic of the FLUOR recombiner.

b. Integrated optics

Integrated optics, analogous to integrated chips in microelectronics, potentially allow large tables of bulk optics to be replaced by miniature devices (Haguenauer *et al.*, 2000). Such hardware provides easy access to spatial filtering and photometric calibration. The successful use of integrated optics to combine beams interferometrically from separated telescopes at IOTA has recently been reported by Berger *et al.* (2001). They used two different chips designed for two-telescope beam combination in the *H* band. One was manufactured using the ion-exchange process: Na^+ ions from a glass substrate were exchanged with Ag^+ ions in a molten salt through a dedicated mask; the other was manufactured using the silica etching technique.

c. Polarization

For phased combination in either the image plane or the pupil plane, the individual incoming beams from the arms of an interferometer should have identical pupil orientations, image orientations, and polarization char-

acteristics (Traub, 2000). If the corresponding mirrors at each reflection (in the case of a two-telescope interferometer) are of same type, both the beams will experience the same phase shifts. The respective s and p components combine independently in the focal plane and produce identical fringe packets. If the sequence of reflections is different, the visibility $\mathcal{V}_{pol}$ of an interferogram is

$$\mathcal{V}_{pol}=\left|\cos\frac{\psi_{sp}}{2}\right|, \tag{105}$$

where ψ_{sp} is the s-p shift between the two beams. The loss of coherence due to misalignment of the optical train, aging of coatings, and accumulation of dust can also be analyzed (Elias, 2001).

At GI2T, the REGAIN uses field rotators consisting of four plane mirrors for each beam to compensate for differences in polarization. In the COAST, starlight passing through the central siderostat undergoes an additional two reflections so that its s and p polarizations experience the same reflections as light from the other siderostats (Baldwin *et al.*, 1998).

Fibers have a natural birefringence that introduces elliptic polarization at the output when linearly polarized light is injected, which causes a loss of the measured visibility. To compensate for the fiber birefringence, the fibers may be wound into one or two loops (Lefèvre, 1980). The supplementary birefringence introduced by this system depends on the radius of the loops; it cancels the effects of the natural birefringence. With this system, the polarization plane can be rotated by twisting the fiber (displacing the loops around the main fiber axis). Another way to minimize birefringence effects consists in using a Babinet compensator, a birefringent quartz crystal consisting of two thin prisms cemented together to form a thin parallel plate, at the input of each fiber.

d. Dispersion

A compensating system for correcting atmospherically induced dispersion is essential at the recombiner. In the REGAIN, the different "chromatic dispersions" between the two beams are compensated by using two prisms that can slide on their hypotenuse, thereby forming a plate with adjustable thickness. This thickness is modified every 4 min, following the variation of the altitude of the observed object (Rousselet-Perraut *et al.*, 1996).

In the case of a fiber-linked recombiner, the dispersion of a fiber-optic coupler made by two fibers, 1 and 2, is expressed by the phase curvature

$$\frac{d^2\psi}{dk^2}, \tag{106}$$

where ψ is the phase of the spectrum of the interferogram. It is demonstrated by Coudé du Foresto *et al.* (1995) that the phase curvature can be given by

$$\frac{d^2\psi}{dk^2}=-2\pi c\lambda^2(\nabla_2\Delta L+L_1\Delta\nabla), \tag{107}$$

where ∇_2 is the dispersion coefficient of fiber 2, $\Delta L=L_2-L_1$ the difference of length between the two fibers, and $\Delta\nabla=\nabla_2-\nabla_1$ the difference of dispersion. The dispersion coefficient depends on the refractive indexes of both the core and the cladding of the fiber. One problem of fiber dispersion is the "flattening" of the interferogram, reducing the fringe contrast. To minimize dispersion, the length of each fiber must be calculated from the dispersion coefficients of each fiber.

4. Calibration

Due to the atmospheric turbulence affecting the wave fronts before recombination, measurements of $\mathcal{V}$ are biased by a random factor depending on the seeing quality. Instrumental flaws leading to optical aberrations and nonbalanced flux between the two beams modify the measured visibility modulus as well. It is therefore important to calibrate each measurement on an object by measuring $\mathcal{V}$ on a nonvariable unresolved source (e.g., a farther star) in the neighborhood, preferably within 1° of the program star to minimize motions of telescopes and delay lines, and at the same turbulence condition. The calibrator and the studied object observations should be interleaved, recording the fringes on both, back and forth a few times during the observing run. Hence one can interpolate the transfer function for each object-observation period. To reproduce the instrumental conditions, the calibrator must be roughly as bright as the object to calibrate; it should ideally have a spectral type and a magnitude similar to those of the studied object. The calibration of the resulting visibility is given by $\mathcal{V}^2_{cal}=\mathcal{V}^2/\mathcal{V}^2_{ref}$ (Berio, Mourard, *et al.*, 1999).

5. Fringe tracking

Fringes are searched by adjusting the delay-line position; however, mechanical constraints on the instrument, errors on the pointing model, thermal drifts, various vibrations, and atmospheric turbulence change the null-OPD point. The error on the optical path difference must be less than the coherence length defined by

$$l_c=c\cdot\tau_c=\frac{\overline{\lambda}^2}{\Delta\lambda}, \tag{108}$$

where $\overline{\lambda}$ is the mean wavelength observed and $\Delta\lambda$ is the spectral interval. This real-time control is called "fringe tracking."

There exist three possible setups for fringe acquisition in the visible spectrum. In the first, the OPD is temporally modulated by a sawtooth signal, using a fast- and short-travel delaying device. The intensity of the recombined beams therefore describes over time a fringe pattern that is recorded by single-pixel detectors. The second method consists of imaging the dispersed recombined beam on a linear detector. In the third, beams are dispersed prior to recombination; recombination is done by focusing them with a common lens as in the Michelson stellar interferometer. In the IR it is essential to use as few pixels as possible in order to reduce

global readout noise. The "white" fringe setup is preferably used for IR observations.

a. Coherencing and cophasing

Techniques to compensate for OPD drift between the two beams of a standard optical interferometer may be classified into two categories: *coherencing* and *cophasing*. The aim of the former is to reduce the optical path difference sufficiently to be able to get fringes, that is, to keep the OPD within the *coherence area* of the fringes. The latter also, called phase locking, aims to climate or "freeze" fringe motion by minimizing the OPD, which must remain much smaller than the wavelength. Fast compensation of OPD variations due to the differential piston mode of the turbulence is achieved by use of a high (10 GHz or more) servo loop frequency and an instrument called a "fringe tracker."

Coherencing with nonwhite fringes is comparable to active optics. In white light it is done, as in the IOTA, by scanning the OPD while acquiring signals to find the null-OPD point in the fringe pattern (Morel *et al.*, 2000). This coherencing yields the OPD correction to apply to the delay line, at a servo-loop rate of a few Hz. With a channeled spectrum, the OPD is proportional to the fringe frequency. Another method, real-time active fringe-tracking, has been applied to dispersed fringes on GI2T using a 2D Fourier transform (Koechlin *et al.*, 1996). Both group-delay tracking and real-time active fringe tracking allow a slow servo loop period (up to a few seconds) by multiplying the coherence length by the number of spectral channels used.

Cophasing that may be compared with the AO system is performed with white fringes using the synchronous detection method; the OPD is quickly scanned over a wavelength range. The signal acquired from the detector is then processed in order to yield the phase shift and the visibility, which can be done by integrating the signal (Shao and Staelin, 1977) over four $\lambda/4$ bins, named A, B, C, and D. The phase shift and visibility modulus are then given by

$$\Delta\varphi = \arctan\left(\frac{B-D}{A-C}\right), \tag{109}$$

$$\mathcal{V} = \frac{\pi\sqrt{(A-C)^2+(B-D)^2}}{\sqrt{2}(A+B+C+D)}. \tag{110}$$

Fringe-tracking methods may be enhanced by introduction of *a priori* information in order to allow observations at fainter $\mathcal{V}$ or fainter magnitudes. Gorham (1998) proposed improving white-light cophasing by filtering data with a function computed to reduce the photon noise. The gain for the tracking limit magnitude at constant $\mathcal{V}$ is between 0.5 and 0.7. Methods introducing *a priori* information for group-delay tracking and real-time active fringe tracking have been proposed as well (Morel and Koechlin, 1998; Padilla *et al.*, 1998).

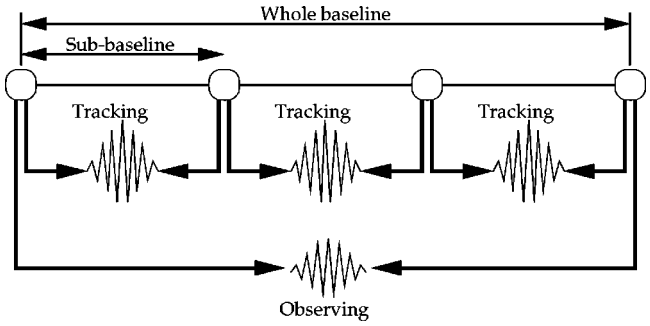

FIG. 11. Schematic representation of baseline bootstrapping. Apertures are represented by circles. From Saha and Morel (2000).

b. Bootstrapping

It is possible to stabilize the fringes using bootstrapping methods at the interferometers. These methods can be categorized into two systems, namely, wavelength bootstrapping and baseline bootstrapping. In the latter, a long baseline is split into shorter segments by placing one or more mirrors between the most widely separated pair. There is higher fringe contrast for a shorter segment, making cophasing easier. Wavelength bootstrapping, on the other hand, uses a multiwavelength system that can simultaneously span a significant range of spatial frequency: the longer wavelengths will usually have the longest visibility amplitude and the shortest wavelengths have most resolution. In this case, two recombiners are required: one for visibility measurement, the other for fringe tracking. For example, at long baselines, when the expected fringe visibility is too low for tracking, it is possible to use a longer wavelength at which the fringe contrast for a white object is higher. Meanwhile, fringes for computing the visibility are acquired at a shorter wavelength than for tracking. This method was applied at the Mark III Interferometer (Quirrenbach *et al.*, 1996). On the other hand, baseline bootstrapping is performed by tracking fringes over a connected series of short baselines to allow low-visibility fringes to be measured on the longest baseline. In this method the photons are shared, and it works well because of the closure-phase relationships. Here the baseline is divided into sub-baselines by adding apertures along the baseline. Fringe tracking is performed on each sub-baseline, where the visibility is higher than with the entire baseline. Then fringes are tracked on the whole baseline as well. Figure 11 depicts the principle of baseline bootstrapping. NPOI employs such a system, which enables one to reach spatial frequencies beyond the first visibility null (Pauls *et al.*, 1998). A related idea has been developed for the Keck Interferometer, as well as for the ESO's Very Large Telescope Interferometer (VLTI).

c. Role of adaptive optics systems

An interferometer works well if the wave fronts from the individual telescopes are coherent. The maximum useful aperture area is proportional to $\lambda^{12/5}$. In order to improve the sensitivity of an interferometer when it is

used to target faint sources, each telescope will have to be reasonably large. A large aperture produces more than 100 speckles in the image, and the fringe pattern within each speckle is randomly phased. Enough photons are required to phase the telescopes into a coherent aperture; therefore, to enhance the instrumental visibility, an AO system should be incorporated. A typical image-width reduction of roughly a factor of 10 and a central intensity enhancement of a factor of $10^{1.5}$ can be achieved on large telescopes (Traub, 2000). Though complete AO systems have not been implemented at any of the interferometers to date, barring the Keck interferometer, which uses full AO corrections, a few of them, viz., GI2T and IOTA, are using a tip-tilt control system. This correction is sensed in the visible using CCD's, and fringe detection is done in the near IR. The IOTA tip-tilt correction system uses a 32×32-pixel CCD for each beam. The maximum rate is 200 Hz (Morel, 2000). A computer reads each frame and computes the centroid. The value of the centroid position is sent to a piezo mirror placed downstream from the secondary mirror of each telescope.

C. Data processing

The optimal integration time required for measuring a visibility point is a tradeoff between the number of photons to collect and the shift caused by the Earth's rotation, moving the sampled point in the (u,v) plane. Though with the Large Binocular Telescope (LBT), the two 8.4-m mirrors will be installed on a common altitude-azimuth mounting, thus allowing information in the (u,v) plane to be continuously combined or coadded, most interferometers use two apertures and are unable to recover the complex visibility. Therefore one must extract from a batch of fringes the modulus of the visibility. Theoretically, using merely the Fourier transform would give an optimal estimate of the visibility modulus, as demonstrated by Walkup and Goodman (1973). However, white-light fringes obtained from coherencing are flawed by the differential piston that modulates their frequency.[2] Techniques used in radio interferometry (in which wavelengths are much longer), like fitting a sine wave through the fringe data, are therefore not suitable. Perrin (1997) has proposed a method that would remove the piston from fringes. However, this method requires a high fringe S/N ratio and may only be applied when a fringe S/N ratio is important.

[2]Here the "piston" is not a piece of a telescope, but the concept of zero-order atmospheric turbulence, equivalent to an optical path offset of the whole pupil. In interferometry, one talks about the difference of piston between the two pupils, or "piston error," which is the main cause of the rapid fluctuations in optical path difference. In coherencing, one measures the center of the interferogram given by a scan (OPD modulation) and applies this measurement to a delay line in order to compensate the OPD.

1. Recovery of visibility functions

The model visibility amplitude $\mathcal{V}(s_\lambda)$ for a uniform disk (UD) of diameter ϕ_{UD} is given by

$$\mathcal{V}(s_\lambda)=\pm\frac{1}{F_0}\int_{-\phi_{UD}/2}^{\phi_{UD}/2}B(\theta)\cos[2\pi s_\lambda\theta]d\theta, \tag{111}$$

where F_0 and $B(\theta)$ are the respective total flux and the brightness distribution of the source, θ is the position angle of the source, and s_λ is the baseline length in wavelengths. This equation reduces to

$$\mathcal{V}(s_\lambda)=\frac{\sin[\pi s_\lambda\phi_{UD}]}{\pi s_\lambda\phi_{UD}}. \tag{112}$$

For objects with circular symmetry, the visibility function is expressed as

$$\mathcal{V}(s_\lambda)=\left|\frac{2J_1(\pi s_\lambda\phi_{UD})}{\pi s_\lambda\phi_{UD}}\right|, \tag{113}$$

where $J_1(\pi s_\lambda\phi_{UD})$ is a Bessel function of the first kind. However, a problem arises due to the limb darkening of the stars.[3] Observations of limb-darkening (LD) measurements require one to collect data in the vicinity of and beyond the first zero or minimum of the visibility function. The radial intensity profile of a star may be given (Hestroffer, 1997) by

$$\mathcal{I}(\mu)=\mathcal{I}(0)\mu^{\alpha_l}, \tag{114}$$

where $\mathcal{I}(\mu)$ is the disk brightness at angle μ ($=\cos\theta$), θ is the angle between the normal to the stellar surface and the direction to the observer, and α_l is the limb-darkening factor depending on the stellar atmosphere. The visibility function in this case may be derived as

$$\mathcal{V}(s_\lambda)=\Gamma(n+1)\frac{|2J_n(\pi s_\lambda\phi_{LD})|}{(\pi s_\lambda\phi_{LD}/2)^n}, \tag{115}$$

where n is $(\alpha_l+2)/2$ and ϕ_{LD} is the limb-darkened diameter of the source. Many interferometers cannot measure low visibilities existing at high angular frequency (i.e., when $\sqrt{u^2+v^2}$ is large) beyond the first minimum of the visibility function. Reconstructions are therefore ambiguous, and neither the diameter nor the limb-darkening factor may be accurately determined. Usually, α_l is *a priori* information given by the stellar atmosphere model. The diameter is therefore deduced from α_l and the interferometric data. Figure 12 represents two visibility curves of the Mira-type variable star R Leo, obtained by the FLUOR/IOTA combination in the K band at two different epochs, which show both the change in equivalent uniform disk diameter and (for the 1997 data) the diffusion by circumstellar material whose sig-

[3]The photons come, on average, from optical depth $\tau\sim1$. Stars are spherical, and their temperature decreases from center to surface. Thus the photons from the center of the disk include some from a hotter zone than those at the limb (edge) of the disk. Since surface brightness scales as T^4 for thermal radiation, the limb looks less bright, hence "limb darkening."

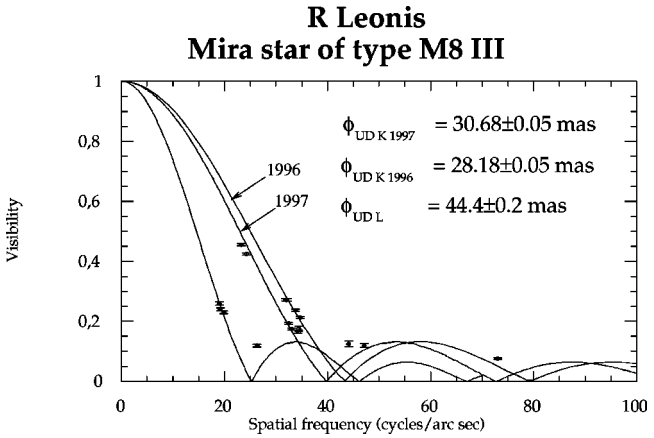

FIG. 12. Visibility curves of the Mira variable R Leonis. Figure courtesy of V. Coudé du Foresto.

nature is a visibility curve substantially different from that of a uniform disk (Perrin *et al.*, 1999).

For two unresolved sources, e.g., a binary system, the expression is formulated as

$$\mathcal{O}(\mathbf{x}) = B_1\delta(\mathbf{x}+\mathbf{x}_0) + B_2\delta(\mathbf{x}+\mathbf{x}_0+\mathbf{x}_s), \tag{116}$$

where $|\mathbf{x}_s|$ is the angular separation between two sources, and B_1 and B_2 are the brightnesses of source 1 and source 2, respectively. The visibility modulus corresponding to this function at $\mathbf{u}$ is therefore

$$|\hat{\mathcal{O}}(\mathbf{u})| = \sqrt{(B_1-B_2)^2 + 4B_1B_2\cos^2(2\pi\mathbf{u}\cdot\mathbf{x}_s)}. \tag{117}$$

It is then useful to use a technique called "supersynthesis": the (u,v) plane is swept during an observation lasting several hours, due to the Earth's rotation. After a large variation of hour angle H, several visibility moduli are therefore measured at different (u,v) points to determine the parameters (B_1, B_2, and $\mathbf{x}_s$) of the system by fitting the function described by Eq. (117).

The visibility function of the thin structures of the circumstellar shell may be computed by considering a coaxial uniform disk and a point source; therefore the function is written as

$$\mathcal{V}(s_\lambda) = V_p + (1-V_p)\left|\frac{2J_1(\pi s_\lambda \phi_s)}{\pi s_\lambda \phi_s}\right|, \tag{118}$$

where ϕ_s is the diameter of the shell and V_p the ratio of power radiated by the star.

2. Derivation of effective temperatures

Combining photometry with the measurement of a limb-darkened stellar diameter yields the stellar emergent flux F_e or surface brightness, which is found from the relation

$$F_e = \frac{4F_\nu}{\phi_{LD}^2}, \tag{119}$$

where F_ν is the measured absolute monochromatic flux received from the star at frequency ν.

The stellar effective temperature T_e is defined in terms of the emergent flux by the Stefan-Boltzmann law. Integrating over all frequencies, we determine a stellar emergent flux

$$F_e = \int F_\nu d\nu = \sigma T_e^4, \tag{120}$$

where σ is the Stefan constant.

D. Ground-based optical/IR arrays

Several ground-based long-baseline optical interferometers have been developed to obtain very-high-angular-resolution information on stellar objects. However, three of them are no longer in operation, viz., (i) the I2T (Labeyrie, 1975), Plateau de Calern, France, (ii) the Mark III interferometer (Shao *et al.*, 1988), Mt. Wilson, USA, and (iii) the Synthèse d'Ouverture en Infrarouge par Détéction Heterodyne (SOIRDÉTÉ) (Gay and Mekarnia, 1988), Plateau de Calern, France.

1. Direct-detection interferometers

(a) Several direct-detection interferometers have been developed. Labeyrie, Schumacher, *et al.* (1986) developed the Grand Interféromètre á Deux Télescopes (GI2T) with two "boule" telescopes that run on north-south tracks with a variable baseline of 12 to 65 m. This instrument at Plateau de Calern, France, combines features of the Michelson design and radio interferometers; it operates in speckle mode. It consists of a pair of 1.52-m telescopes on altitude-altitude mounts. Each telescope is housed in a sphere (3.5 m diameter) made of concrete, which has three mirrors directing the horizontal afocal Coudé beam to the recombiner optics. Light beams from both the telescopes are superposed at the foci in order to produce Young's fringes. The driving system of the sphere consists of a pair of rings; each ring is motorized by three actuators acting in three orthogonal directions within two different tangential planes. The two rings alternately carry the sphere, which in turn produces continuous motion with a resolution of the order of 1 μm. The main drawback comes from the slow pointing of the telescopes; only four or five stars can be tracked during the night.

(b) The Sydney University Stellar Interferometer (SUSI), located 20 km west of Narrabri, in Northern New South Wales, Australia, has a very long baseline ranging from 5 to 640 m (north-south) that is achieved with an array of 11 input stations equipped with a siderostat and relay optics, located to give a minimal baseline redundancy (Davis, Tango, Booth, ten Brummelaar, *et al.*, 1999). The intermediate baseline forms a geometric progression increasing in steps of $\sim$40%. Starlight is steered by two siderostats of 20 cm diameter into the evacuated pipe system that carries the light to the atmospheric refraction corrector (at the central laboratory) consisting of the pairs of counter-rotating Risley prisms via a beam reducer. It either proceeds towards the optical path length compensator or is diverted towards the acquisition camera. On leaving the optical path length

compensator, the beams from the two arms of this interferometer may be switched over to one of the optical tables (blue or red) for recombination.

(c) The Cambridge Optical Aperture Synthesis Telescope (COAST), Cambridge, UK, uses four independent telescopes consisting of a 50-cm siderostat flat feeding a fixed horizontal 40-cm Cassegrain telescope with a magnification of 16. These are arranged in a Y layout with one telescope on each arm, movable to a number of fixed stations, and one telescope at the center of the Y (Baldwin *et al.*, 1998). Light from each siderostat passes through pipes containing air at ambient pressure into the beam-combining laboratory (inside a tunnel). The four beams emerging from the path compensator are each split at a dichroic; the longer wavelength ($\lambda > 650$ nm) of the visible band passes into the beam-combining optics and the shorter ones are used for acquisition and autoguiding. Each output beam passes through an iris diaphragm and is focused by a long focus lens onto a fiber-fed single-element avalanche photodiode detector for fringe detection.

(d) The Infrared Optical Telescope Array (IOTA), situated at Mt. Hopkins, Arizona, consists of three 45-cm collector assemblies located at various stations on the L-shaped baseline (5–38 m) that comprises a siderostat, an afocal Cassegrain telescope, and an active relay mirror (Traub *et al.*, 2000). In the recombining table, the optical differences are compensated by fixed and variable delays and the beams are recombined onto a beam splitter, producing two complementary interference signals (Carleton *et al.*, 1994). A fast autoguiding system is used to correct atmospheric wave-front tilt errors. Two active delay lines for three telescopes are provided; a scanning piezo mirror is used to modulate the OPD between the two telescopes.

(e) The U.S. Navy Prototype Optical Interferometer (NPOI), located at Lowell Observatory, Arizona, is designed to measure positions with precision comparable to that of Hipparcos (1997). However, the aperture sizes limit the array to bright star astrometry. It was developed as a Y-shaped baseline configuration that includes subarrays for imaging and for astrometry. For the astrometric mode, four fixed siderostats (0.4 m diameter) are used with the baselines extendable from 19 to 38 m. The astrometric subarray has a laser metrology system to measure the motions of the siderostats with respect to one another and to the bedrock. For the imaging mode, six transportable siderostats (0.12 m diameter) are used. Three siderostat positions are kept with equal space for each arm of the Y. Coherence of imaging configuration is maintained by phase bootstrapping. The synchronous detection method applied to signals from several spectral channels has been used as well (Benson *et al.*, 1998).

(f) The Palomar Testbed Interferometer (PTI), Palomar Observatory, California, is an IR phase-tracking interferometer that was developed as a test bench for the Keck Interferometer. The main thrust is to develop techniques and methodologies for doing narrow-angle astrometry; therefore it is designed to observe two stars simultaneously to measure the angle between them with high precision. It uses coherent fringe demodulation and active fringe-tracking systems with an array detector at 2.2 μm and active delay lines with a range of ± 38 m. It comprises three 40-cm siderostats that are coupled to beam compressors. These siderostats are used pairwise to provide baselines of up to 110 m (Colavita *et al.*, 1999). Both phase and group-delay measurements for narrow-angle astrometry are being carried out (Lawson *et al.*, 2000). Visibility is estimated from the fringe quadrature, either incoherently or using source phase referencing to provide a longer integration time (Colavita, 1999).

2. Heterodyne interferometry

The heterodyne technique is generally used in radio astronomy to reduce the high-frequency signal to an intermediate one. Such a technique, when used for beam recombination in IR interferometry, offers a larger coherence length and a simplification of the transport of the signal from the collector to the recombiner (coaxial cables instead of mirrors).

Let $\mathcal{U}_s(t)$ and $\mathcal{U}_l(t)$ be, respectively, the signals of a wave coming from a star and of an artificial source (laser), which are expressed as

$$\mathcal{U}_s(t) = a_{s0} \cdot e^{-i[\omega_s \cdot t - \psi]}, \tag{121}$$

$$\mathcal{U}_l(t) = a_{l0} \cdot e^{-i\omega_l \cdot t}. \tag{122}$$

The laser is the phase reference. A detector like a photodiode, illuminated by the sources (star+laser), yields an electrical signal corresponding to the light intensity:

$$\begin{aligned}\mathcal{I}(t) &= |\mathcal{U}_s(t) + \mathcal{U}_l(t)|^2 \\ &= (a_{s0} \cdot e^{-i[\omega_s \cdot t - \psi]} + a_{l0} \cdot e^{-i\omega_l \cdot t}) \\ &\quad \times (a_{s0} \cdot e^{i[\omega_s \cdot t + \psi]} + a_{l0} \cdot e^{-i\omega_l \cdot t}) \\ &= a_{s0}^2 + a_{l0}^2 + 2 \cdot a_{l0} \cdot a_{s0} \cdot \cos[(\omega_l - \omega_s) + \psi].\end{aligned} \tag{123}$$

If ω_l and ω_s are close, the frequency of $\mathcal{I}$ is low enough to fit in the bandwidth of the detector and its electronics (a few GHz), and $\mathcal{I}$ carries the phase information from the radiation of the star. By correlating (multiplying) the signals $\mathcal{I}_1$ and $\mathcal{I}_2$ yielded by two apertures with heterodyning systems, one can extract a visibility term. However, the lasers must have the same phases for the two apertures.

Heterodyne interferometry at a spectral range of 8–11.5 μm was employed on the SOIRDÉTÉ (Observatoire de Calern, France), an IR interferometer that consisted of a pair of 1-m telescopes with a 15-m east-west horizontal baseline (Gay and Mekarnia, 1988). It was an interesting project but ultimately a failure and produced no significant scientific results. In this project, beams were received in the central laboratory on a double cat's-eye delay line on a step-by-step movable carriage; natural OPD drift due to the Earth's rotation was used for acquiring fringes (Rabbia *et al.*, 1990). Heterodyne interferometry is also used on the recently developed mid-IR Infrared Spatial Interferometer (ISI), Mt. Wilson, California (Townes *et al.*, 1998), which is an outstanding suc-

cess with many scientific results. It is well suited to the study of circumstellar material around bright evolved stars. It features three movable telescopes; each telescope comprises a 1.65-m parabolic mirror and a 2-m flat mirror equipped with an automated guiding and tip-tilt control system at 2 μm (Lipman *et al.*, 1998). The starlight from each aperture is first mixed with a stable CO_2 laser local oscillator, converting the signal to microwave frequencies, followed by path-length matching and fringe detection in a correlator. On the ISI, two CO_2 lasers are used, the phase of one being controlled by the other. Here the interferometer noise is dominated by shot noise of the laser, and thermal background is negligible for setting the sensitivity limit (Hale *et al.*, 2000). The ISI utilizes the Earth's rotation and periodic discrete changes of the baseline to obtain a wide range of effective baselines and map the visibility functions of the stellar objects.

E. Projects planned and under development

(1) The Center for High Angular Resolution Astronomy (CHARA) array at Mt. Wilson, California, comprises six fixed 1-m telescopes arranged in a Y-shaped configuration with a maximum baseline of $\sim$350 m that will operate at optical and IR wavelengths (McAlister *et al.*, 1998) with a limiting resolution of 0.2 mas. The key scientific goals of this interferometer are binary star astrometry, observations of stars with well-determined spectroscopic elements, and determination of metal abundances.

(2) The Mitaka Optical and IR Array (MIRA), National Astronomical Observatory, Japan, consists of several interferometers built one by one. The first of the series was MIRA-I (Machida *et al.*, 1998) which has 25-cm siderostats and a 4-m baseline. Its successor, MIRA-I.2 (Sato *et al.*, 1998), has the same baseline and slightly larger siderostats (30 cm). It features equipment encountered on many operating interferometers: beam compressors (yielding 30-mm beams), a delay line operating in vacuum, a tip-tilt correction system and laser metrology. These instruments are specially designed for astrometry.

(3) The Large Binocular Telescope (LBT) on Mt. Graham, Arizona, which consists of two 8.4-m primary mirrors (Hill, 2000), is under construction, The LBT mirrors are comounted on a fully steerable altitude-azimuth mounting, in which variable delay lines for path equalization are not needed. At near-IR wavelengths, a field of view of one arcminute or more is expected with unprecedented spatial resolution of the order of 8–9 mas at $\lambda\sim1$ μm and a variable baseline of 0–23 m (Wehinger, 2001).

(4) Another interferometer, the Magdalena Ridge Observatory Array, USA, with three elements (2 $\times$2.4 m plus 0.8 m) has also received initial funding and is under development.

1. Interferometers of heterogeneous nature

The Keck Interferometer, Mauna Kea, USA (Colavita *et al.*, 1998), and the VLTI, ESO, Paranal, Chile (Derie *et al.*, 2000), are of a heterogeneous nature. Recombination of two telescopes, one large and one small, poses problems because the S/N ratio is the one given by the small telescope. Nevertheless, recent success in obtaining interferometric fringes from starlight by the two large telescopes at Keck and the VLTI (Glindemann and Paresce, 2002) will have an enormous impact on developing future large optical arrays.

The Keck Interferometer comprises two 10-m and four 1.8-m "outrigger" telescopes. The main telescopes are to be used for imaging with outriggers to fill in incomplete parts of the (u,v) plane. This array will combine phased pupils provided by adaptive optics for the main telescopes and fast tip-tilt correction on the outriggers. Beam recombination will be carried out by five two-way combiners at 1.5–2.4 μm for fringe tracking, astrometry, and imaging. A 10-μm nulling combiner for exozodiacal disk characterization is in the planning stages. A differential phase technique to aim at detecting faint sources near a bright object is also under development (Akeson *et al.*, 2000).

At the VLTI, beams are received from the movable telescopes in a central laboratory for recombination and are made to interfere after introducing suitable optical delay lines. Coudé beams from these apertures are sent through delay lines operating in rooms at atmospheric pressure but at accurately controlled temperature. The beams reach an optical switch yard to be directed to one of the four expected recombiners, (i) a single-mode fiber recombiner (2.2 μm) that is intended to debug the upstream subsystems of VLTI, (ii) a beam-splitter-based recombiner that operates at 10 μm, (iii) a recombiner that operates between 1 and 2.5 μm, and (iv) a recombiner for narrow-angle astrometry.

2. Interferometry with large arrays

The next generation of imaging interferometers, with at least 15 or more elements, should have snapshot capability in an instantaneous mode. Beams from separated telescopes of such an interferometer must be recombined in the focal point as in the case of a Fizeau interferometer, which is optically equivalent to a single large telescope masked with a multiaperture screen, so as to reproduce exactly the ensemble of collecting telescopes (Traub, 1986).

Development of an Optical Very Large Array (OVLA), an array of 27 telescopes of 1.5 m diameter, was initiated more than a decade ago by Labeyrie, Lamaitre, *et al.* (1986). Each telescope is housed in a fiberglass sphere (Dejonghe *et al.*, 1998) that is mounted on a six-legged robot to enable it to move on the ground while fringes are acquired, eliminating the need for optical delay lines. A secondary mirror makes the beam afocal and compressed. A third steerable flat mirror sends this beam out through a slit located on the sphere to the central station, where all other beams coming

from other telescopes are combined into a single high-resolution image. OVLA has also been considered for different possible aperture diameters, including 12–25 m (Labeyrie, 1998). A new telescope structure has been imagined for this class of very large collectors: the "cage telescope," in which the sphere is replaced with an icosahedral truss steerable by a different mechanical system. Ridgway and Roddier (2000) have proposed a project to develop an Infrared Very Large Array (IRVLA) with a total baseline of ~1000 m, consisting of 27 telescopes, each with an aperture of 4 m. Another proposed project called the "Large-Aperture Mirror Array" (LAMA) would employ 18 fixed 10-m liquid-mirror telescopes, located within a circle of 60 m diameter, to collect 50% of the light that falls within this area (Hickson, 2001).

3. Hypertelescope imaging

"Densified-pupil multiaperture imaging interferometry" is a subtle technique that may provide direct images at the focal plane. The pupils from each telescope of an interferometric array are brought very close to each other (almost touching) in a new pupil plane before focussing. With a large number of telescopes, this provides an actual image—that is, one does not need to calculate fringe visibility for image reconstruction—but the field of view is small. The number of pixels depends on the number of telescopes. Conceptually, this differs from the Fizeau interferometer, which becomes inefficient when the subaperture spacing is large compared to its total size. The reason is that most of the energy goes into a broad diffractive halo rather than into a narrow interference peak, which precludes obtaining usable snapshot images with kilometric or megametric arrays in space.

Densifying the exit pupil, i.e., distorting it to increase the relative size of the subpupils in such a way that the pattern of subaperture centers is preserved, concentrates the halo and intensifies the image (Labeyrie, 1996). Figure 13 depicts the concept of the hypertelescope. Pedretti *et al.* (2000) derived the integrated intensities of the central peaks of the images on the star Capella, which were that obtained by taking two separate exposures of 100 s in the Fizeau and densified-pupil mode of the hypertelescope. The comparison of these values showed that the intensity gain was a factor of 24 ± 3 over the Fizeau configuration. Imaging arrays of huge size, possibly approaching a million kilometers, to observe neutron stars, may become feasible in this way. These would certainly warrant the name "hypertelescopes." They could provide an image with full luminosity in a narrow field of $\approx\lambda/B_s$, where B_s is the distance between the subapertures of the array.

For ground arrays, an elliptical track is one way of compensating for the Earth's rotation; with delay lines, a periodic dilute aperture could also be built at a scale of 10 km. In space, it would be a periodic hexagonal paving in the case of the hypertelescope version proposed by Labeyrie (2001) for the Terrestrial Planet Finder (TPF). This space interferometer would have a Fizeau focus,

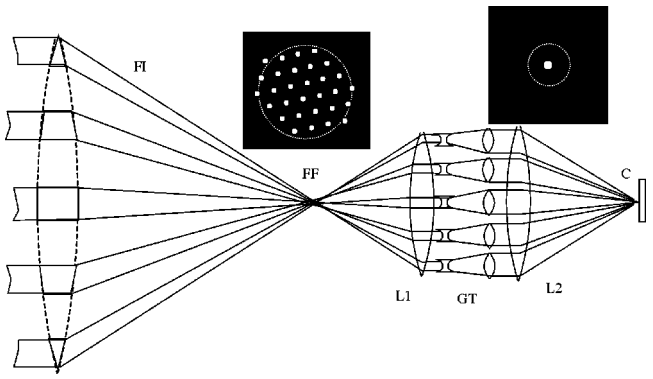

FIG. 13. Diagram of a hypertelescope. The focal image FF provided by a Fizeau interferometer FI is reimaged by lenses L1 and L2 on camera C, through an array of miniature and inverted Galilean telescopes GT. They densify the exit beam, thus shrinking the diffractive envelope (dotted circle) of the focal pattern with respect to the interference peak. For an off-axis star, they also attenuate the local tilt of the flat wave front transmitted from L1, while preserving the global tilt. The wave front from an off-axis star thus acquires stair steps while becoming densified at L2. The interference peak is displaced more than the envelope, but remains within it if the step is below one wavelength. Figure courtesy of A. Labeyrie.

followed by a small pupil densifier and a coronagraph (Boccaletti *et al.*, 2000). Unlike ground-based elliptic rings, where images are directly obtained at a recombination station located at a focus of the ellipse or periodic arrays on the ground, space arrays can be globally pointed.

The cophasing of the array may be done hierarchically (Pedretti and Labeyrie, 1999) by cophasing triplets of beams (yielding a honeycomb pattern in the image plane), then triplets of triplets, etc. Piston errors are measurable from the triplet images. Another way of analyzing the piston errors (Labeyrie, 1999a) is an extension of the classical dispersed fringes used since Michelson: a set of monochromatic images recorded with a spectro-imager is organized as an x,y,λ data cube, and its three-dimensional Fourier transform is calculated to extract piston errors in pairs or triplets of apertures.

F. Space-borne interferometry

The advantage of deploying long-baseline interferometry in space is that observing can be done at any wavelength and for a longer duration in the absence of atmospheric turbulence. The difficulty comes from the need for high-precision positioning, as well as for the toughness required for space operation. A new generation of ultralightweight active mirrors (Burge *et al.*, 2000; Angel, 2001) is essential to resolve the problems of size and weight.

1. Space Technology 3

A new generation of scientific spacecraft, NASA's Space Technology 3 (ST3; Gorham *et al.*, 1999), is sched-

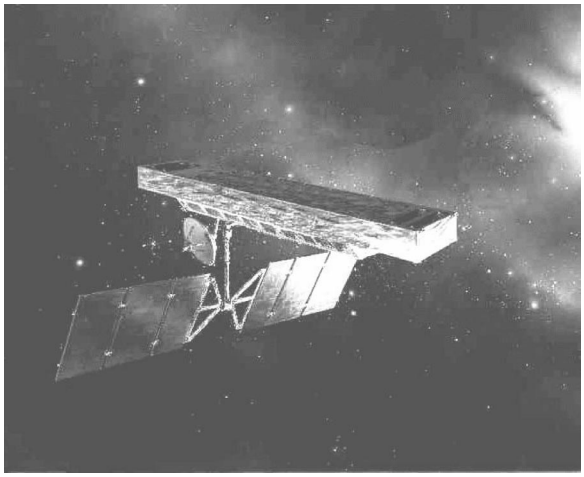

FIG. 14. An artist's rendition of the Space Interferometry Mission (SIM). Figure courtesy of NASA/JPL/Caltech.

uled for 2003. It consists of two independent free-flying elements launched into an Earth-trailing heliocentric orbit. One is a collector sending light from the observed object to the second element, featuring another collector, an optical delay line, and a beam recombiner. The aim of ST3 is to demonstrate and validate technologies that might be used for future space-borne interferometers. The two elements of ST3 should be able to move up to 1 km from each other, while being controlled by laser metrology. However, the designed delay line of ST3 is only designed for up to 20 m of optical path difference. This instrument will be used as an imaging interferometer for studying such objects as Wolf-Rayet or Be stars (Linfield and Gorham, 1999).

2. Space Interferometry Mission

Space Interferometry Mission (SIM) is also being designed and will be launched by NASA. The main goal of this interferometer will be to collect new high-precision astrometry results, including the possibility of Jovian planet detection around stars up to 1 kiloparsec (kpc) distant and terrestrial planet detection around nearby stars (Unwin *et al.*, 1998). The design consists of one free flyer with a 10-m boom supporting 30-cm collectors. The expected angular accuracy is 1 μas (microarcsecond) in narrow-angle mode (with a 1° field of view) and 4 μas in wide-angle mode. The sensitivity for astrometry is $m_v = 20$ after a 4-h integration. This interferometer will work in the visible spectrum (0.4–0.9 μm). In order to get an accurate knowledge of the baseline vector **B** for wide-angle astrometry without collector motions, it will feature two auxiliary interferometers, aimed at reference stars (gridlocking). An artist's rendition of the SIM is depicted in Fig. 14.

3. Other projects

Two new projects being pursued, Darwin and TPF, to search for ozone on extrasolar planets (Penny *et al.*, 1998) and for detecting extrasolar planets directly (Beichman, 1998), respectively.

VI. IMAGE RECONSTRUCTION TECHNIQUES

The diffraction-limited phase retrieval of a degraded image is indeed an art. This is true in other branches of physics, too, e.g., electron microscopy, wave-front sensing, and crystallography, where one often wishes to recover phase. AO systems may also require image-processing algorithms, since the real-time corrected image is often partial. Prior to using such algorithms, the basic operations to be performed are dead pixel removal, debiasing, flat fielding, sky or background emission subtraction, and suppression of correlated noise. In what follows, Secs. VI.A–VI.C describe methods for obtaining components of the object's Fourier transform, while Sec. VI.D describes methods for reconstructing an image from these components, which can usually be described as a "deconvolution."

A. Shift-and-add algorithm

The *shift-and-add* technique (Lynds *et al.*, 1976; Worden *et al.*, 1976) aligns and adds the recorded short-exposure images; the method is analogous to the tip-tilt mirror of conventional AO systems. The position of the brightest pixel $\mathbf{x}_k$ must be located in each specklegram $\mathcal{I}_k(\mathbf{x})$ [$\mathcal{I}_k(\mathbf{x}_k) > \mathcal{I}_k(\mathbf{x})$ for all $\mathbf{x} \neq \mathbf{x}_k$], followed by shifting the specklegram (without any rotation) to place this pixel at the center of the image space. The shift-and-add image $\mathcal{I}_{sa}(\mathbf{x})$ is obtained by averaging over the set of the shifted specklegrams,

$$\mathcal{I}_{sa}(\mathbf{x}) = \langle \mathcal{I}_{\mathbf{k}}(\mathbf{x}+\mathbf{x}_{\mathbf{k}}) \rangle. \tag{124}$$

Large variations in the brightness of the brightest pixels are observed in a set of speckle images; the contamination level may not be proportional to its brightest pixel (Bates and McDonnell, 1986). The adjusted shift-and-add image $\mathcal{I}_{asa}(\mathbf{x})$ can be defined as

$$\mathcal{I}_{asa}(\mathbf{x}) = \langle w[\mathcal{I}_k(\mathbf{x}_k)] \mathcal{I}_k(\mathbf{x}+\mathbf{x}_k) \rangle, \tag{125}$$

where $w[\mathcal{I}_k(\mathbf{x}_k)]$ is the weighting in relation to the brightness of the brightest pixel. The choice of the same quantity can be made as $w\{\mathcal{I}_k(\mathbf{x}_k)\} = \mathcal{I}_k(\mathbf{x}_k)$. An array of impulses is constructed by putting an impulse at each center of gravity with a weight proportional to the speckle intensity. This impulse array is considered to be an approximation of the instantaneous point-spread function and is cross-correlated with the speckle frame. Disregarding peaks lower than the preset threshold, one defines the mth speckle mask, $\text{mask}_m(\mathbf{x})$, as

$$\text{mask}_m(\mathbf{x}) = \sum_{n=1}^{M} \mathcal{I}_m(\mathbf{x}_{m,n}) \delta(\mathbf{x} - \mathbf{x}_{m,n}). \tag{126}$$

The mth masked speckled image $m\mathcal{I}_m(\mathbf{x})$ is expressed as

$$m\mathcal{I}_m(\mathbf{x}) = \mathcal{I}_m(\mathbf{x}) \otimes \text{mask}_m(\mathbf{x}). \tag{127}$$

The Lynds-Worden-Harvey image is obtained by averaging Eq. (127). For direct speckle imaging, the shift-and-add image, $\mathcal{I}_{sa}(\mathbf{x})$, is a contaminated one containing

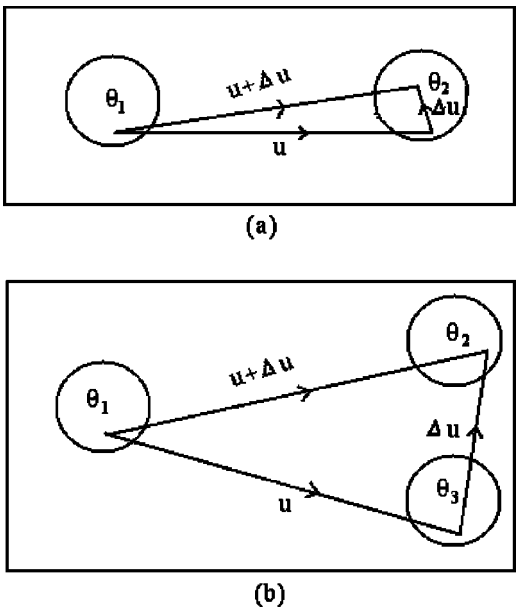

FIG. 15. Diagrammatic representation of pupil subaperture of diameter r_0: (a) approximate phase closure is achieved by the Knox-Thompson method; (b) complete phase closure is achieved by the triple correlation method.

two complications—a convolution, $\mathcal{S}_k(\mathbf{x})$, and an additive residual, $\mathcal{C}(\mathbf{x})$—which means

$$\mathcal{I}_{sa}(\mathbf{x}) = \mathcal{O}(\mathbf{x}) \star \mathcal{S}(\mathbf{x}) + \mathcal{C}(\mathbf{x}), \tag{128}$$

where $\mathcal{S}(\mathbf{x}) = \Sigma_{k=1}^{k} \delta(\mathbf{x} - \mathbf{x}'_k) d_k, \mathbf{x}'_k$ is the constant position vector, and d_k is a positive constant. It is essential to calibrate $\mathcal{I}_{sa}(\mathbf{x})$ with an unresolved point source and reduce it in the same way to produce $\mathcal{S}(\mathbf{x})$. The estimate for the object $\mathcal{O}(\mathbf{x})$, is evaluated from the inverse Fourier transform of the following equation:

$$\hat{\mathcal{O}}(\mathbf{u}) = \frac{\hat{\mathcal{I}}_{sa}(\mathbf{u})}{\hat{\mathcal{I}}_0(\mathbf{u}) + \hat{\mathcal{N}}(\mathbf{u})}, \tag{129}$$

which is the first approximation of the object irradiance. This method is found to be insensitive to telescope aberrations but sensitive to dominating photon noise.

Another method called *selective image reconstruction* selects the few sharpest images that are recorded when the atmospheric distortion is naturally at minimum, from a large dataset of short exposures (Dantowitz *et al.*, 2000). Baldwin *et al.* (2001) have demonstrated the potential of such a technique.

B. Knox-Thomson method

The Knox-Thomson method (Knox and Thomson, 1974) defines the correlation of $\mathcal{I}(\mathbf{x})$ and $\mathcal{I}(\mathbf{x})$ multiplied by a complex exponential factor with spatial frequency vector $\mathbf{\Delta u}$. The approximate phase closure is achieved by two vectors (see Fig. 15), $\mathbf{u}$ and $\mathbf{u}+\mathbf{\Delta u}$, assuming that the pupil phase is constant over $\mathbf{\Delta u}$. Let the general second-order moment be the cross spectrum $\langle \hat{\mathcal{I}}(\mathbf{u}_1) \hat{\mathcal{I}}^*(\mathbf{u}_2) \rangle$. It takes significant values only if $|\mathbf{u}_1 - \mathbf{u}_2| < r_0/\lambda$; the typical value of $|\mathbf{\Delta u}|$ is ~ 0.2–$0.5\, r_0/\lambda$. Invoking Eq. (70), we define $\hat{\mathcal{I}}(\mathbf{u})$, the Fourier transform of a 2D irradiance distribution $\mathcal{I}(\mathbf{x})$, as

$$\hat{\mathcal{I}}(\mathbf{u}) = \int_{-\infty}^{+\infty} \mathcal{I}(\mathbf{x}) e^{-i2\pi \mathbf{u}\mathbf{x}} d\mathbf{x}. \tag{130}$$

In image space, the correlations of $\mathcal{I}(\mathbf{x})$ are derived as

$$\mathcal{I}(\mathbf{x}_1, \mathbf{\Delta u}) = \int_{-\infty}^{+\infty} \mathcal{I}^*(\mathbf{x}) \mathcal{I}(\mathbf{x} + \mathbf{x}_1) e^{i2\pi \mathbf{\Delta u}\mathbf{x}} d\mathbf{x}, \tag{131}$$

where $\mathbf{x}_1 = \mathbf{x}_{1x} + \mathbf{x}_{1y}$ are 2D spatial coordinate vectors. The Knox-Thomson correlation may be defined in Fourier space as a product of $\hat{\mathcal{I}}(\mathbf{u})$,

$$\hat{\mathcal{I}}(\mathbf{u}_1, \mathbf{\Delta u}) = \hat{\mathcal{I}}(\mathbf{u}_1) \hat{\mathcal{I}}^*(\mathbf{u}_1 + \mathbf{\Delta u}) \tag{132}$$

$$= \hat{\mathcal{O}}(\mathbf{u}_1) \hat{\mathcal{O}}^*(\mathbf{u}_1 + \mathbf{\Delta u}) \hat{\mathcal{S}}(\mathbf{u}_1) \hat{\mathcal{S}}^*(\mathbf{u}_1 + \mathbf{\Delta u}), \tag{133}$$

where $\mathbf{u}_1 = \mathbf{u}_{1x} + \mathbf{u}_{1y}$ and $\mathbf{\Delta u} = \mathbf{\Delta u}_x + \mathbf{\Delta u}_y$ are 2D spatial frequency vectors. $\mathbf{\Delta u}$ is a small, constant offset spatial frequency. A number of subplanes are used by taking different values of $\mathbf{\Delta u}$. The argument of Eq. (133) provides the phase difference between the two spatial frequencies separated by $\mathbf{\Delta u}$ and is expressed as

$$\arg|\hat{\mathcal{I}}^{KT}(\mathbf{u}_1, \mathbf{\Delta u})| = \psi(\mathbf{u}_1) - \psi(\mathbf{u}_1 + \mathbf{\Delta u}). \tag{134}$$

Therefore Eq. (133) translates into

$$\hat{\mathcal{I}}(\mathbf{u}_1, \mathbf{\Delta u}) = |\hat{\mathcal{O}}(\mathbf{u}_1)||\hat{\mathcal{O}}(\mathbf{u}_1 + \mathbf{\Delta u})||\hat{\mathcal{S}}(\mathbf{u}_1)||\hat{\mathcal{S}}(\mathbf{u}_1 + \mathbf{\Delta u})| \times e^{i[\theta_{\mathcal{O}}^{KT}(\mathbf{u}_1, \mathbf{\Delta u}) + \theta_{\mathcal{S}}^{KT}(\mathbf{u}_1, \mathbf{\Delta u})]}. \tag{135}$$

The phase of the object spectrum of Eq. (135) is encoded in the term $e^{i\theta_{\mathcal{O}}^{KT}(\mathbf{u}_1, \mathbf{\Delta u})} = e^{i[\psi_{\mathcal{O}}(\mathbf{u}_1) - \psi_{\mathcal{O}}(\mathbf{u}_1 + \mathbf{\Delta u})]}$. In a single image realization, it is corrupted by the random phase differences due to the atmosphere-telescope optical transfer function, $e^{i\theta_{\mathcal{S}}^{KT}(\mathbf{u}_1, \mathbf{\Delta u})} = e^{i[\psi_{\mathcal{S}}(\mathbf{u}_1) - \psi_{\mathcal{S}}(\mathbf{u}_1 + \mathbf{\Delta u})]}$. If Eq. (135) is averaged over a large number of frames, the feature $(\mathbf{\Delta}\psi_{\mathcal{S}})$ is equal to 0. $|\hat{\mathcal{O}}(\mathbf{u}_1 + \mathbf{\Delta u})| \approx |\hat{\mathcal{O}}(\mathbf{u}_1)|$, when $\mathbf{\Delta u}$ is small, etc.; therefore

$$\langle \hat{\mathcal{I}}(\mathbf{u}_1, \mathbf{\Delta u}) \rangle = |\hat{\mathcal{O}}(\mathbf{u}_1)||\hat{\mathcal{O}}(\mathbf{u}_1 + \mathbf{\Delta u})| e^{i[\theta_{\mathcal{O}}^{KT}(\mathbf{u}_1, \mathbf{\Delta u})]} \times \langle \hat{\mathcal{S}}(\mathbf{u}_1) \hat{\mathcal{S}}^*(\mathbf{u}_1 + \mathbf{\Delta u}) \rangle. \tag{136}$$

From Eqs. (136), and (73), the object phase spectrum, $\theta_{\mathcal{O}}^{KT}(\mathbf{u}_1, \mathbf{\Delta u})$, can be determined.

C. Triple-correlation technique

The *triple-correlation* technique is a generalization of the phase-closure technique (Sec. IV.B.2.) that is used in radio/optical interferometry. In this technique the image is processed to produce a *bispectrum* Fourier transform, defined below (Weigelt, 1977; Lohmann *et al.*, 1983). It is insensitive to (i) atmospherically induced random phase errors, (ii) random motion of the image centroid, and (iii) permanent phase errors introduced by telescope aberrations; any linear phase term in the object phase cancels out as well. Other advantages of this method are that it (i) provides information about the object phases

with a better S/N ratio from a limited number of frames, and (ii) serves as the means of image recovery with diluted coherent arrays (Reinheimer and Weigelt, 1987). Its chief disadvantage is that it makes severe demands on computing facilities with 2D data since the calculations are four dimensional.

A triple correlation is obtained by multiplying a shifted object $\mathcal{I}(\mathbf{x}+\mathbf{x}_1)$ with the original object $\mathcal{I}(\mathbf{x})$, followed by cross correlating the result with the original one (for example, in the case of a close binary star, the shift is equal to the angular separation between the stars, masking one of the two components of each double speckle). The calculation of the ensemble-averaged triple correlation is given by

$$\mathcal{I}(\mathbf{x}_1,\mathbf{x}_2)=\left\langle \int_{-\infty}^{+\infty}\mathcal{I}(\mathbf{x})\mathcal{I}(\mathbf{x}+\mathbf{x}_1)\mathcal{I}(\mathbf{x}+\mathbf{x}_2)d\mathbf{x}\right\rangle, \tag{137}$$

where $\mathbf{x}_j=\mathbf{x}_{jx}+\mathbf{x}_{jy}$ are 2D spatial coordinate vectors. The bispectrum is given by

$$\hat{\mathcal{I}}(\mathbf{u}_1,\mathbf{u}_2)=\langle\hat{\mathcal{I}}(\mathbf{u}_1)\hat{\mathcal{I}}^*(\mathbf{u}_1+\mathbf{u}_2)\hat{\mathcal{I}}(\mathbf{u}_2)\rangle, \tag{138}$$

$$=\hat{\mathcal{O}}(\mathbf{u}_1)\hat{\mathcal{O}}^*(\mathbf{u}_1+\mathbf{u}_2)\hat{\mathcal{O}}(\mathbf{u}_2)\times\langle\hat{\mathcal{S}}(\mathbf{u}_1)\hat{\mathcal{S}}^*(\mathbf{u}_1+\mathbf{u}_2)\hat{\mathcal{S}}(\mathbf{u}_2)\rangle, \tag{139}$$

where $\mathbf{u}_j=\mathbf{u}_{jx}+\mathbf{u}_{jy}$, $\hat{\mathcal{I}}(\mathbf{u}_j)=\int\mathcal{I}(\mathbf{x})e^{-i2\pi\mathbf{u}_j\mathbf{x}}d\mathbf{x}$, and $\hat{\mathcal{I}}^*(\mathbf{u}_1+\mathbf{u}_2)=\int\mathcal{I}(\mathbf{x})e^{i2\pi(\mathbf{u}_1+\mathbf{u}_2)\mathbf{x}}d\mathbf{x}$. The object bispectrum is given by

$$\hat{\mathcal{I}}_{\mathcal{O}}(\mathbf{u}_1,\mathbf{u}_2)=\hat{\mathcal{O}}(\mathbf{u}_1)\hat{\mathcal{O}}^*(\mathbf{u}_1+\mathbf{u}_2)\hat{\mathcal{O}}(\mathbf{u}_2)=\frac{\langle\hat{\mathcal{I}}(\mathbf{u}_1)\hat{\mathcal{I}}^*(\mathbf{u}_1+\mathbf{u}_2)\hat{\mathcal{I}}(\mathbf{u}_2)\rangle}{\langle\hat{\mathcal{S}}(\mathbf{u}_1)\hat{\mathcal{S}}^*(\mathbf{u}_1+\mathbf{u}_2)\hat{\mathcal{S}}(\mathbf{u}_2)\rangle}. \tag{140}$$

The modulus $|\hat{\mathcal{O}}(\mathbf{u})|$ of the object's Fourier transform $\hat{\mathcal{O}}(\mathbf{u})$ can be evaluated from the object bispectrum $\hat{\mathcal{I}}_{\mathcal{O}}(\mathbf{u}_1,\mathbf{u}_2)$. The argument of Eq. (138) gives the phase difference and is expressed as

$$\arg|\hat{\mathcal{I}}^{TC}(\mathbf{u}_1,\mathbf{u}_2)|=\psi(\mathbf{u}_1)+\psi(\mathbf{u}_2)-\psi(\mathbf{u}_1+\mathbf{u}_2). \tag{141}$$

The phase of the object's spectrum is encoded in the term $e^{i\theta_{\mathcal{O}}^{TC}(\mathbf{u}_1,\mathbf{u}_2)}$. It is corrupted in a single realization by random phase differences due to the atmosphere-telescope optical transfer function, $e^{i\theta_{\mathcal{S}}^{TC}(\mathbf{u}_1,\mathbf{u}_2)}=e^{i[\psi_{\mathcal{S}}(\mathbf{u}_1)-\psi_{\mathcal{S}}(\mathbf{u}_1+\mathbf{u}_2)+\psi_{\mathcal{S}}(\mathbf{u}_2)]}$. If a sufficient number of specklegrams are averaged, one can overcome this degradation. Let $\theta_{\mathcal{O}}^{TC}(\mathbf{u}_1,\mathbf{u}_2)$ be the phase of the object bispectrum; then

$$\hat{\mathcal{O}}(\mathbf{u})=|\hat{\mathcal{O}}(\mathbf{u})|e^{i\psi(\mathbf{u})}, \tag{142}$$

$$\hat{\mathcal{I}}_{\mathcal{O}}(\mathbf{u}_1,\mathbf{u}_2)=|\hat{\mathcal{I}}_{\mathcal{O}}(\mathbf{u}_1,\mathbf{u}_2)|e^{i\theta_{\mathcal{O}}^{TC}(\mathbf{u}_1,\mathbf{u}_2)}. \tag{143}$$

Equations (142) and (143) may be inserted into Eq. (140), yielding the relations

$$\hat{\mathcal{I}}_{\mathcal{O}}(\mathbf{u}_1,\mathbf{u}_2)=|\hat{\mathcal{O}}(\mathbf{u}_1)||\hat{\mathcal{O}}(\mathbf{u}_2)||\hat{\mathcal{O}}(\mathbf{u}_1+\mathbf{u}_2)|\times e^{i[\psi_{\mathcal{O}}(\mathbf{u}_1)-\psi_{\mathcal{O}}(\mathbf{u}_1+\mathbf{u}_2)+\psi_{\mathcal{O}}(\mathbf{u}_2)]}\rightarrow, \tag{144}$$

$$\theta_{\mathcal{O}}^{TC}(\mathbf{u}_1,\mathbf{u}_2)=\psi_{\mathcal{O}}(\mathbf{u}_1)-\psi_{\mathcal{O}}(\mathbf{u}_1+\mathbf{u}_2)+\psi_{\mathcal{O}}(\mathbf{u}_2). \tag{145}$$

Equation (145) is a recursive one for evaluating the phase of the object's Fourier transform at coordinate $\mathbf{u}=\mathbf{u}_1+\mathbf{u}_2$. The object's phase spectrum at $(\mathbf{u}_1+\mathbf{u}_2)$ can be written as

$$\psi_{\mathcal{O}}(\mathbf{u}_1+\mathbf{u}_2)=\psi_{\mathcal{O}}(\mathbf{u}_1)+\psi_{\mathcal{O}}(\mathbf{u}_2)-\theta_{\mathcal{O}}^{TC}(\mathbf{u}_1,\mathbf{u}_2). \tag{146}$$

If the object spectrum at $\mathbf{u}_1$ and $\mathbf{u}_2$ is known, the phase of the object bispectrum at $(\mathbf{u}_1+\mathbf{u}_2)$ can be computed. The bispectrum phases are defined mod 2π; therefore the recursive reconstruction in Eq. (139) may lead to π phase mismatches between the computed bispectrum phase values along different paths to the same point in frequency space. However, according to Northcott *et al.* (1988), phases from different paths to the same point cannot be averaged to reduce noise under this condition. A variation of the nature of the computing argument of the term $e^{i\psi_{\mathcal{O}}(\mathbf{u}_1+\mathbf{u}_2)}$ is needed to obtain the phase of the object bispectrum. Equation (146) translates into

$$e^{i\psi_{\mathcal{O}}(\mathbf{u}_1+\mathbf{u}_2)}=e^{i[\psi_{\mathcal{O}}(\mathbf{u}_1)+\psi_{\mathcal{O}}(\mathbf{u}_2)-\theta_{\mathcal{O}}^{TC}(\mathbf{u}_1,\mathbf{u}_2)]}. \tag{147}$$

The values obtained using the unit amplitude phasor recursive reconstructor are insensitive to π phase ambiguities. Saha *et al.* (1999) have developed a code based on this reconstructor. The least-squares formulation of phase reconstruction (Glindemann *et al.*, 1991), the projection-slice theorem of tomography, and the Radon transform (Northcott *et al.*, 1988) have been successfully applied in the development of phase reconstruction from the bispectrum.

D. Deconvolution algorithms

Most deconvolution techniques, in which *a priori* information plays an essential role, can be simplified to the minimization/maximization of a criterion by using an iterative numerical method (Gerchberg and Saxton, 1972) that bounces back and forth between the image-domain and Fourier-domain constraints until two images are found that produce the input image when convolved together (Ayers and Dainty, 1988).

1. Blind iterative deconvolution technique

Let the degraded image $\mathcal{I}(\mathbf{x})$ be used as the operand. An initial estimate of the point-spread function $\mathcal{S}(\mathbf{x})$, has to be provided. The image is deconvolved from the estimated point-spread function by Wiener filtering (see Sec. IV.A.1), which is an operation of multiplying a suitable Wiener filter [constructed from $\hat{\mathcal{S}}(\mathbf{u})$ of the point-spread function] with $\hat{\mathcal{I}}(\mathbf{u})$. The technique of Wiener filtering damps the high frequencies and minimizes the mean-square error between each estimate and the true spectrum. This filtered deconvolution takes the form

$$\hat{\mathcal{O}}(\mathbf{u})=\hat{\mathcal{I}}(\mathbf{u})\frac{\hat{\mathcal{O}}_f(\mathbf{u})}{\hat{\mathcal{S}}(\mathbf{u})}. \tag{148}$$

The Wiener filter $\hat{\mathcal{O}}_f(\mathbf{u})$ is derived as

$$\hat{\mathcal{O}}_f(\mathbf{u}) = \frac{\hat{\mathcal{S}}(\mathbf{u})\hat{\mathcal{S}}^*(\mathbf{u})}{|\hat{\mathcal{S}}(\mathbf{u})|^2 + |\hat{\mathcal{N}}(\mathbf{u})|^2}. \tag{149}$$

The term $\hat{\mathcal{N}}(\mathbf{u})$ can be replaced with a constant estimated as the rms fluctuation of the high-frequency region in the spectrum where the object power is negligible. The Wiener filtering spectrum $\hat{\mathcal{O}}(\mathbf{u})$ takes the form

$$\hat{\mathcal{O}}(\mathbf{u}) = \hat{\mathcal{I}}(\mathbf{u}) \frac{\hat{\mathcal{S}}^*(\mathbf{u})}{\hat{\mathcal{S}}(\mathbf{u})\hat{\mathcal{S}}^*(\mathbf{u}) + \hat{\mathcal{N}}(\mathbf{u})\hat{\mathcal{N}}^*(\mathbf{u})}. \tag{150}$$

The result, $\hat{\mathcal{O}}(\mathbf{u})$, is transformed back to image space, and the negatives in the image and the positives outside a prescribed domain (called object support) are set to zero. The average of negative intensities within the support is subtracted from all pixels. The process is repeated until the negative intensities decrease below the noise. A new estimate of the point-spread function is next obtained by Wiener filtering $\mathcal{I}(\mathbf{x})$ with a filter constructed from the constrained object $\mathcal{O}(\mathbf{x})$; this completes one iteration. This entire process is repeated until the derived values of $\mathcal{O}(\mathbf{x})$ and $\mathcal{S}(\mathbf{x})$ converge to sensible solutions.

Blind iterative deconvolution has the ability to retrieve the diffraction-limited image of an object from a single specklegram without reference star data (Saha and Venkatakrishnan, 1997). Jefferies and Christou (1993) have developed an algorithm that requires several speckle frames for improving the convergence. Barnaby *et al.* (2000) used this algorithm and parametric blind deconvolution to postprocess the data obtained with the AO system and found that the secondary of 81 Cnc was $0.12m_v$ brighter than the primary at 0.85 μm.

2. Fienup algorithm

The Fienup (1978) algorithm reconstructs an object using only the modulus of its Fourier transform. At the kth iteration, $\mathcal{G}_k(\mathbf{x})$, an estimate of the object's Fourier transform is compared with the measured one and made to conform with the modulus at all Fourier frequencies. The inverse transform of the result yields an image $\mathcal{G}'_k(\mathbf{x})$. This iteration is completed by forming a new estimate of the object that conforms to certain object-domain constraints, e.g., positivity and finite extent, such that

$$\hat{\mathcal{G}}_k(\mathbf{u}) = |\hat{\mathcal{G}}_k(\mathbf{u})| e^{i\phi_k(\mathbf{u})} = \mathcal{F}[\mathcal{G}_k(\mathbf{x})], \tag{151}$$

$$\hat{\mathcal{G}}'_k(\mathbf{u}) = |\hat{\mathcal{I}}(\mathbf{u})| e^{i\phi_k(\mathbf{u})}, \tag{152}$$

$$\mathcal{G}'_k(\mathbf{x}) = \mathcal{F}^{-1}[\hat{\mathcal{G}}'_k(\mathbf{u})], \tag{153}$$

$$\mathcal{G}_{k+1}(\mathbf{x}) = \begin{cases} \mathcal{G}'_k(\mathbf{x}), & \mathbf{x} \notin \gamma \\ 0, & \mathbf{x} \in \gamma, \end{cases} \tag{154}$$

where the region γ is the set of all points at which $\mathcal{G}'_k(\mathbf{x})$ violates the object-domain constraints, and $\mathcal{G}_k(\mathbf{x})$, $\hat{\mathcal{G}}'_k(\mathbf{u})$, and ϕ_k are estimates of $\mathcal{I}(\mathbf{x})$, $\hat{\mathcal{I}}(\mathbf{u})$, and the phase ψ of $\hat{\mathcal{I}}(\mathbf{u})$, respectively.

The above procedure may be accelerated if an estimate $\mathcal{G}_{k+1}(\mathbf{x})$ is formed as

$$\mathcal{G}_{k+1}(\mathbf{x}) = \begin{cases} \mathcal{G}_k(\mathbf{x}), & \mathbf{x} \notin \gamma \\ \mathcal{G}_k(\mathbf{x}) - \beta \mathcal{G}'_k(\mathbf{x}), & \mathbf{x} \in \gamma, \end{cases} \tag{155}$$

where β is a constant feedback parameter.

3. Other iterative algorithms

(a) Several other iterative algorithms are worthy of mention. The Richardson-Lucy (Richardson, 1972; Lucy, 1974) algorithm converges to the maximum-likelihood solution for Poisson statistics in the data, which is appropriate for optical data with noise from counting statistics. It forces the restored image to be non-negative and conserves flux both globally and locally at each iteration.

(b) The Magain-Courbin-Sohy algorithm (Magain *et al.*, 1998) is based on the principle that sampled data cannot be fully deconvolved without violating the sampling theorem (Shannon, 1949), which determines the maximal sampling interval allowed so that an entire function can be reconstructed from sampled data. The sampled image should be deconvolved by a narrower function than the total point-spread function so that the resolution of the deconvolved image is compatible with the adopted sampling. The positivity constraint, unlike the traditional deconvolution methods, is not mandatory; accurate astrometric and photometric information of the astronomical objects can be obtained.

(c) The myopic iterative step-preserving algorithm (MISTRAL; Conan *et al.*, 1998) is based on the Bayesian theorem, which uses the probabilistic approach. It incorporates a positivity constraint and some *a priori* knowledge of the object (an estimate of its local mean and a model for the power spectral density, etc.). It also allows one to account for the noise in the image and the imprecise knowledge of the point-spread function. MISTRAL has produced a few spectacular images after processing AO images.

(d) A nonlinear iterative image-reconstruction algorithm called the Pixon method has been developed by Puetter and Yahil (1999) that provides statistically unbiased photometry and robust rejection of spurious sources. Unlike other Bayesian methods, this technique does not assign explicit prior probabilities to image models. It minimizes complexity by smoothing the image model locally. The model is then described using a few irregular-sized pixons containing similar amounts of information, rather than many regular pixels containing variable signal-to-noise data. Eke (2001) is of the opinion that it has the ability to detect sources in data with a low S/N ratio and to deconvolve a telescope beam in order to recover the internal structure of a source.

4. Aperture-synthesis mapping

Reconstruction of complex images involves the knowledge of complex visibilities. Interferometers with

two apertures have limited possibilities for image reconstructions because one cannot recover the phase of the visibility. The phase of a visibility may be deduced from the closure phase that has been applied in optical interferometry (Baldwin *et al.*, 1998). The process after data acquisition consists of phase calibration and visibility phase reconstruction from closure-phase terms by a technique similar to bispectrum processing. From complex visibilities acquired from a phased interferometric array, it is possible to reconstruct the image by actually interpolating the function in the (u,v) plane. Let the output of a synthesis array be a set of visibility functions $\mathcal{V}(u_j,v_j)$ that are obtained by averaging the quasisinusoidal response of each interferometer pair. The resultant brightness distribution is

$$\mathcal{I}''(x,y)=\sum_{j=1}^{N}\mathcal{V}(u_j,v_j)w_j e^{[-2\pi i(u_j x+v_j y)]}, \tag{156}$$

where $\mathcal{I}''(x,y)$ is usually called the dirty image, which is the convolution of the true brightness distribution $\mathcal{I}'(x,y)$ with the synthesized beam $\mathcal{S}'(x,y)$, and w_j is a weight associated with the jth N. The map will show sufficient details when the (u,v) coverage is good, but it is not the best representation of the sky and contains many artifacts, notably positive and negative side lobes around bright peaks. If the sampling of the (u,v) plane is irregular and uneven, the dirty beam will have large sidelobes and confuse and obscure the structure of interest in the image.

Several nonlinear methods have been introduced to restore the unmeasured Fourier components in order to produce a more physical map. These methods work on the constraint that the image must be positive or zero everywhere, and they make use of *a priori* knowledge about the extent of the source and statistics of the measurement processes. Since the restoration is not unique, the image restoration must select the best solution.

a. CLEAN algorithms

The most commonly used approaches to deconvolving dirty images fall into two groups: CLEAN algorithms (Högbom, 1974) and maximum-entropy methods (Ables, 1974). To some extent, CLEAN algorithms and maximum-entropy methods are complementary in their application. Of the two, CLEAN is the more often used, particularly in radio astronomy, because it is both computationally efficient and intuitively easy to understand. This procedure is a nonlinear technique that applies an iterative beam-removing method. It starts with a dirty image $\mathcal{I}'(x,y)$ made by the linear Fourier inversion procedure and attempts to decompose this image into a number of components, each of which contains part of the dirty beam $\mathcal{S}'(x,y)$. One wishes to determine the set of numbers $\mathcal{A}_i(x_i,y_i)$ such that

$$\mathcal{I}'(x,y)=\sum_i \mathcal{A}_i\mathcal{S}'(x-x_i,y-y_i)+\mathcal{I}_R(x,y), \tag{157}$$

where $\mathcal{I}_R(x,y)$ is the residual brightness distribution after decomposition. The solution is considered satisfactory if $\mathcal{I}_R(x,y)$ is of the order of the expected noise.

The algorithm searches the dirty image for the pixel with largest absolute value $\mathcal{I}_{\max}$ and subtracts a dirty beam pattern centered on this point with amplitude $G_l\mathcal{I}_{\max}$, where G_l is called the loop gain. The residual map is searched for the next largest value and the second beam stage is subtracted and so on. The iteration is stopped when the maximum residual noise level is consistent with the expected noise level. The iteration consists of a residual image that contains noise and low-level source calculations plus a set of amplitudes and positions of the components removed. These components can be considered as an array of delta functions, which are convolved with a clean beam and added to produce a CLEANed image. The clean beam is usually chosen as a truncated elliptical Gaussian about the same size as the main lobe of the dirty beam. CLEAN results in a map with the same resolution as the original dirty map without side lobes.

b. Maximum-entropy method

It is found that CLEAN generally performs well on small compact sources, while the maximum-entropy method does better on extended sources. The maximum-entropy method is employed in a variety of fields like medical imaging, crystallography, and radio and x-ray astronomy. With this procedure probability distributions can be estimated when limited information is available. In addition, it treats all the polarization component images simultaneously (unlike CLEAN, which deconvolves different polarization component images independently) and guarantees essential conditions on the image. It makes use of the highest spatial frequency information by finding the smoothest image consistent with the interferometric data. While enforcing positivity and conserving the total flux in the frame, it estimates smoothness by the "entropy" S that is of the form

$$S=-\sum_i h_j \ln\frac{h_j}{m_j}, \tag{158}$$

where $\mathbf{h}=[h_j]$ represents the image to be restored, and $\mathbf{m}=[m_j]$ is known as the prior image.

It can be shown that $S\leqslant 0$; the equality holds if $\mathbf{h}=\mathbf{m}$. The value of S is a measure of the similarity between $\mathbf{h}$ and $\mathbf{m}$ if the entropy S is maximized without any data constraints. With data constraints, the maximum of S will be less than zero, implying that $\mathbf{h}$ has been modified and deviates from its prior model $\mathbf{m}$.

The maximum-entropy method solves the multidimensional constraints minimization problem. It uses only those measured data and derives a brightness distribution that is the most random, i.e., has the maximum entropy S of any brightness distribution consistent with the measured data. Maintaining an adequate fit to the data, it reconstructs the final image that fits the data within the noise level.

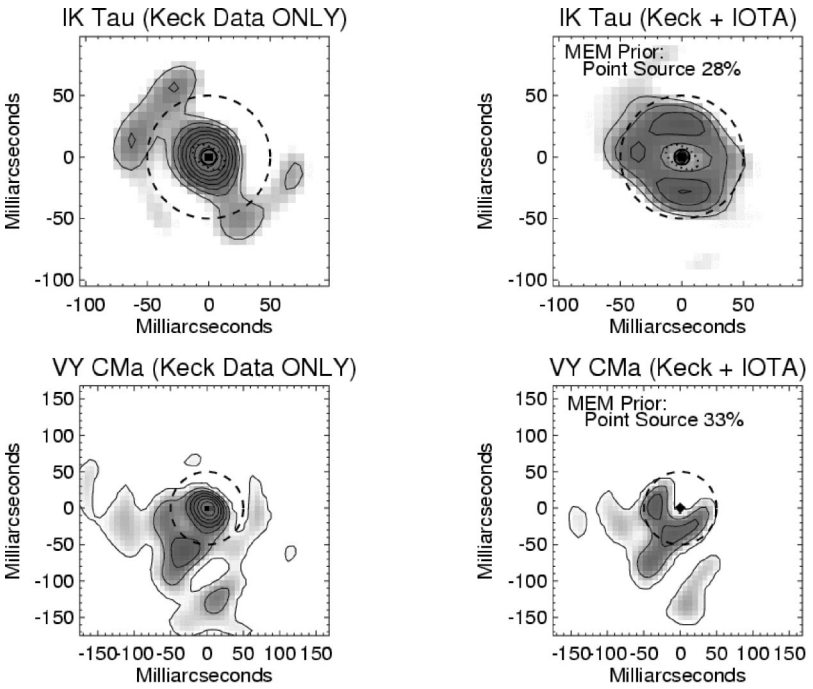

FIG. 16. Maximum-entropy method (MEM) image reconstructions of the dust shell around IK Tau and VY CMa: left panels, reconstructions from data obtained with a single Keck telescope using aperture masking (baselines up to 9 m at 2.2 μm); right panels, the dust shell reconstructions when the fractional amounts of star and dust shell emission are constrained to be consistent with both the Keck and the Infrared Optical Telescope Array (IOTA) data. From Monnier *et al.* (2001).

Monnier *et al.* (2001) have reconstructed the dust shells around two evolved stars, IK Tau and VY CMa, using (u,v) coverage from contemporaneous observations at the Keck Interferometer and IOTA. Figure 16 depicts the maximum-entropy method reconstructions of the dust shells around these stars. Their results clearly indicate that without adequate spatial resolution it is improbable to separate out cleanly the contributions of the star from the hot inner radius of the shell (left panel in Fig. 16). These authors were of the opinion that image reconstructions from the interferometer data are not unique and yield results that depend heavily on the biases of a given reconstruction algorithm. By including the long-baseline (>20 m) data from the IOTA interferometer (right panel), one can include the fraction of the flux arising from the central star in the image reconstruction process by using the maximum-entropy method beforehand. One can see that for a dust shell such as IK Tau additional IOTA data are critical in accurately interpreting the physical meaning of interferometer data. The dashed lines show the expected inner radius of the dust shell from the data obtained at the ISI.

c. Self-calibration

To produce images with an accurate visibility amplitude and poor or absent phases, self-calibration can be used (Baldwin and Warner, 1978). Cornwell and Wilkinson (1981) introduced a modification by explicitly solving for the telescope-specific error as part of the reconstructing step. They fit measured Fourier phases using a combination of intrinsic phases plus telescope phase errors.

If the field of observation contains one dominating internal point source that can be used as an internal phase reference, the visibility phase at other spatial frequencies is derived. A hybrid map can be made with the measured amplitudes together with model phase distributions. Since the measured amplitudes differ from the single-point-source model, the hybrid map diffuses from the model map. Adding some new feature to the original model map, one obtains an improved model map in the next iteration. With clever selection of features to be added to the model in each iteration, the procedure converges.

d. Linear approach

Another approach to the deconvolution problem is to formulate it as a linear system of the form

$$\mathbf{Ax}=\mathbf{b}, \tag{159}$$

and then use algebraic techniques to solve this system. The elements of **A** contain samples of the dirty beam, the elements of **b** are samples of the dirty image, while **x** contains components of the reconstructed image. Without any additional constraints matrix **A** is singular: additional information has to be added to find a solution. Assumptions that regularize the system include positivity and compact structure of the source. An algebraic approach is not new in itself, but practical applications of such techniques in astronomy have become feasible only recently, e.g., for the non-negative least-squares method (Briggs, 1995).

e. WIPE algorithm

Lannes *et al.* (1994) present another technique, WIPE, based on a least-squares approach, in which support information is used to regularize the algorithm. Again, a linear system similar to that mentioned in the previous paragraph is solved, but using a technique that iterates between (u,v) and the image planes. Unlike CLEAN and the maximum-entropy method, WIPE sup-

presses excessive extrapolation of higher spatial frequencies during the deconvolution.

VII. ASTRONOMICAL APPLICATIONS

Optical interferometry has been a boon for astronomy and astrophysics. The following subsections consider the astrophysical importance and the prospects of interferometry.

A. Results from single-aperture interferometry

Single-aperture interferometry has contributed to the study of the Sun and solar system and a variety of stellar astrophysical problems.

1. Sun and solar system

The existence of solar features with sizes of the order of 100 km or smaller was found by means of speckle imaging (Harvey, 1972; Harvey and Breckinridge, 1973). From observations of photospheric granulation from disk center to limb at $\lambda = 550 \pm 5$ nm, Wilken *et al.* (1997) found a decrease in the relative rms contrast of the center-to-limb granular intensity. A time series of high-spatial-resolution images has revealed the dynamical evolution of sunspot fine structure, namely, umbral dots, penumbral filaments, and facular points (Denker, 1998). Small-scale brightening in the vicinity of sunspots was also observed in the wings of strong chromospheric absorption lines. These structures, which are concomitant with strong magnetic fields, show brightness variations close to the diffraction limit of the Vacuum Tower Telescope (~ 0.16 arcsec at 550 nm), Observatorio del Teide (Tenerife). With the phase-diverse speckle method, Seldin *et al.* (1996) found that the photosphere at scales below 0.3 arcsec is highly dynamic.

Speckle imaging has been successful in resolving the heavenly dance of the Pluto-Charon system (Bonneau and Foy, 1980), as well as in determining shapes of asteroids (Drummond *et al.*, 1988). Reconstructions of Jupiter with subarcsecond resolution have also been carried out by Saha *et al.* (1997).

2. Stellar objects

Studies of close binary stars play a fundamental role in measuring stellar masses, providing a benchmark for stellar evolution calculations; a long-term benefit of interferometric imaging is a better calibration of the main-sequence mass-luminosity relationship. The procedure for obtaining masses involves combining the spectroscopic information with the astrometric orbit from the interferometric data. Continuous observations need to be carried out in order to sort out the orbital elements and their masses, luminosities, and distances. Radiative transfer in the expanding atmospheres of the component stars can be distorted by physical effects, such as rotation or tidal effects, and these can be modeled as well.

More than 8000 interferometric observations of stellar objects have been reported so far, of which 75% are of binary stars (Hartkopf *et al.*, 1997). The separation of most of the new components discovered is found to be less than 0.25 arcsec. From an inspection of the interferometric data, Mason *et al.* (1999) confirmed the binary nature of 848 objects discovered by the Hipparcos satellites; Prieur *et al.* (2001) reported high-angular-resolution astrometric data of 43 binary stars that were also observed with same satellite. Torres *et al.* (1997) derived individual masses for θ^1 Tau using the distance information from θ^2 Tau; they found the empirical mass-luminosity relation to be in good agreement with theoretical models. Gies *et al.* (1997) measured the radial velocity for the massive binary 15 Mon. With the speckle spectrograph, Baba, Kuwamura, Miura, and Norimoto (1994) observed a binary star, ϕ And ($\rho = 0.53$ arcsec) and found that the primary, a Be star, has Hα in emission while the companion has Hα in absorption. The high-angular-polarization measurements of the pre-main-sequence binary system Z CMa at 2.2 μm by Fischer *et al.* (1998) reveal that both components are polarized; the secondary showed an unexpectedly large degree of polarization.

Studies of multiple stars can also reveal mysteries. For instance, R136a was thought to be a very massive star with a mass of $\sim 2500 M_\odot$ (solar masses; Cassinelli *et al.*, 1981). Speckle imagery revealed that R136a was a dense cluster of stars (Weigelt and Baier, 1985; Pehlemann *et al.*, 1992). R64 (Schertl *et al.*, 1996), HD97950, and the central object of the giant HII-region starburst cluster NGC3603 (Hofmann *et al.*, 1995) have been observed as well. The starlike luminous blue variable Eta Carinae (η Car), an intriguing massive southern object, was found to be a multiple object (Weigelt and Ebersberger, 1986). The polarimetric reconstructed images with 0.11 arcsec resolution in the Hα line of η Car exhibit an elongated compact structure consistent with the presence of a circumstellar equatorial disk (Falcke *et al.*, 1996).

Many supergiants have an extended gaseous envelope, which can be imaged in their chromospheric lines. The diameter of a few such objects, e.g., α Ori and Mira, is found to be wavelength dependent (Bonneau and Labeyrie, 1973; Labeyrie *et al.*, 1977; Weigelt *et al.*, 1996). Recent studies have also confirmed the asymmetries on their surfaces and reported the presence of hotspots, as well (Wilson *et al.*, 1992; Haniff *et al.*, 1995; Bedding, Zijlstra, *et al.*, 1997; Tuthill *et al.*, 1997; Monnier *et al.*, 1999; Tuthill, Monnier, *et al.*, 1999). The surface imaging of long-period variable stars (Tuthill, Haniff, and Baldwin, 1999) such as VY CMa reveals a nonspherical circumstellar envelope (Wittkowski, Langer, and Weigelt, 1998). Monnier *et al.* (1999) found emission to be one-sided, inhomogeneous, and asymmetric in the IR and derived the line-of-sight optical depths of its circumstellar dust shell. The radiative transfer modeling of the supergiant NML Cyg reveals multiple dust-shell structures (Blöcker *et al.*, 2001).

High-resolution imagery may depict the spatial distribution of circumstellar matter surrounding objects that eject mass, particularly in young compact planetary nebulae or newly formed stars in addition to T Tauri

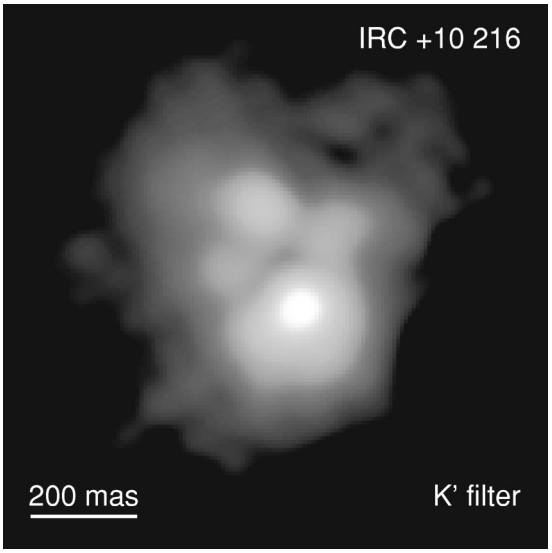

FIG. 17. Speckle masking reconstruction of IRC+10216; the resolution of the object was found to be 76 mas for the K' band. From Osterbart *et al.* (1996), courtesy of R. Osterbart.

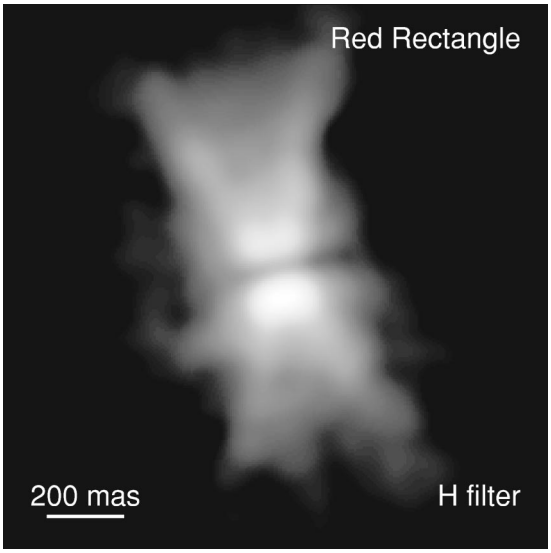

FIG. 18. Speckle masking reconstruction of the reflection nebula around the star HD44179 in the Red Rectangle (AFGL 915), exhibiting two lobes with $\rho \approx 0.15$ arcsec; the dark lane between the lobes might be due to an obscuring dust disk, and the central star is a close binary system. From Osterbart *et al.* (1996), courtesy R. Osterbart.

stars, late-type giants, or supergiants. The large, older, and evolved planetary nebulae show a great variety of structures (Balick, 1987), including (a) spherically symmetric (A39), (b) filamentary (NGC6543), (c) bipolar (NGC6302), and (d) peculiar (A35). The structure may form in the very early phases of the formation of the nebula itself, when it is very compact and unresolved. By making maps at many epochs, as well as by following the motion of specific structural features, one is able to understand the dynamical processes at work. The structures might be different in different spectral lines, e.g., ionization stratification in NGC6720 (Hawley and Miller, 1977), and hence maps should be made in various atomic and ionic emission lines too.

Major results of studies along these lines include (i) measuring the angular diameters of several young planetory neublae (Barlow *et al.*, 1986; Wood *et al.*, 1986), (ii) resolving five individual clouds around carbon star IRC+10216 (see Fig. 17) with a central peak surrounded by patchy circumstellar matter (Osterbart *et al.*, 1996; Weigelt *et al.*, 1998), (iii) exhibiting two lobes of the evolved object, the Red Rectangle (see Fig. 18; Osterbart *et al.*, 1996), (iv) revealing a spiral pinwheel in the dust around WR104 (Tuthill, Monnier, and Danchi, 1999), and (v) depicting the spherical dust shell around the oxygen-rich asymptotic giant branch (AGB) star AFGL 2290 (Gauger *et al.*, 1999). Images of the young star LkHα 101 in which the structure of the inner accretion disk is resolved have been reported, as well (Tuthill *et al.*, 2001). Detailed information can also be determined for the modeling of the 2D radiative transfer in stellar objects, especially concerning their symmetry—spherical, axial, or lack thereof—and any clouds, plumes, etc., associated with them (Men'shchikov and Henning, 1997; Gauger *et al.*, 1999).

The shells of both novae and supernovae have a complex nature, which can be multiple, stratified, or asymmetric. High-resolution mapping may depict the events near the star and the interaction zones between gas clouds with different velocities. Soon after the explosion of the supernova SN1987A, various observers monitored the expansion of the shell at different wavelengths (Nisenson *et al.*, 1987; Papaliolios *et al.*, 1989; Wood *et al.*, 1989). The increasing diameter of the supernova in several spectral lines and the continuum was measured (Karovska *et al.*, 1989). Nulsen *et al.* (1990) derived the velocity of the expansion and found that the size of this object was strongly wavelength dependent at the early-epoch–prenebular phase, indicating stratification in its envelope. A bright source at a distance of 0.06 arcsec away from SN1987A with $\Delta m = 2.7$ mag at Hα was also detected. Recently, Nisenson and Papaliolios (1999) detected a faint second spot with $\Delta m_v = 4.2$ mag on the opposite side of SN1987A with $\rho = 160$ mas.

Another important field of observational astronomy is the study of the physical processes temperature, density, and gas velocity in the active regions of active galactic nuclei. Optical imaging by emission lines on subarcsecond scales can reveal the structure of the narrow-line region. The scale of narrow-line regions is well resolved by the diffraction limit of a moderate-sized telescope. The time variability of active galactic nuclei ranging from minutes to decades can also be studied. NGC 1068 is an archetypeal Type-2 Seyfert galaxy. Observations of this object, corroborating theoretical modeling like radiative transfer calculations, have made significant contributions to our understanding of its structure. Ebstein *et al.* (1989) found this object to have a bipolar structure in the OIII emission line. Near-IR observations at the Keck Interferometer trace a very compact central core and extended emission with a size of the order of 10 pc on either side of an unresolved nucleus (Weinberger *et al.*, 1999). Wittkowski, Balega, *et al.* (1998) have re-

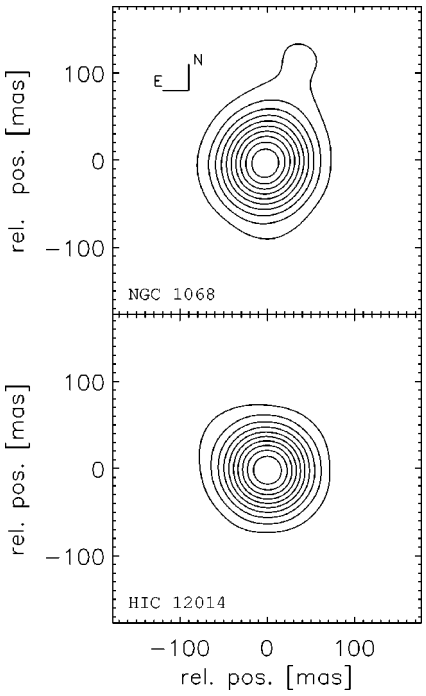

FIG. 19. Speckle masking reconstruction of (top) NGC1068 and (bottom) the unresolved star HIC12014. The contours are from 6% to 100% of peak intensity from Wittkowski, Balega, *et al.* (1998), courtesy of M. Wittkowski.

solved the central 2.2-μm core by bispectrum speckle interferometry at the diffraction limit of the Special Astrophysical Observatory (SAO) 6-m telescope, with a FWHM size of $\sim$2 pc for an assumed Gaussian intensity distribution. Figure 19 depicts the reconstructed image of the active galactic nucleus NGC1068. Subsequent observations by Wittkowski *et al.* (1999) indicate that this compact core is asymmetric, with a position angle of $\sim$20° and an additional, more extended structure in the north-south direction out to $\sim$25 pc.

Quasars may be gravitationally lensed by stellar objects such as stars, galaxies, and clusters of galaxies, located along the line of sight. The aim of the high angular imagery of these quasistellar objects is to determine their structure and components, which are clues to the distribution of mass in the Universe. The ability to resolve these objects in the range of 0.2–0.6 arcsec would very likely lead to the discovery of more lensing events. The gravitational image of the multiple-quasar object PG1115+08 was resolved by Foy *et al.* (1985); one of the bright components, discovered to be double (Hege *et al.*, 1981), was found to be elongated, which, according to them, might be due to a fifth component of the quasar.

3. Glimpses of AO observations

Most of the results obtained from ground-based telescopes equipped with AO systems are in the near-IR band, while results at visible wavelengths continue to be sparse. The contributions to date have been mainly in studies of

(i) planetary meteorology (Poulet and Sicardy, 1996; Marco *et al.*, 1997; Roddier *et al.*, 1997);
(ii) images of Neptune's ring arcs (Sicardy *et al.*, 1999), which are interpreted as gravitational effects by one or more moons;
(iii) the nucleus of M31 (Davidge, Rigaut, *et al.*, 1997);
(iv) young stars and multiple-star systems (Bouvier *et al.*, 1997);
(v) the galactic center (Davidge, Simons, *et al.*, 1997);
(vi) Seyfert galaxies and quasar host galaxies (Hutchings *et al.*, 1998, 1999), and
(vii) the circumstellar environment (Roddier *et al.*, 1996).

Images of other objects such as (a) the nuclear region of NGC3690 in the interacting galaxy Arp 299 (Lai *et al.*, 1999), (b) the starburst/active galactic nuclei NGC863, NGC7469, NGC1365, NGC1068, (c) the core of the globular cluster M13 (Lloyd-Hart *et al.*, 1998), and (d) R136 (Brandl *et al.*, 1996), etc., have also been obtained from moderate-sized telescopes. Adaptive optics images of the radio glaxy 3C294 with the highest-ever angular resolution in the near-IR bands were obtained at Keck Observatory (Quirrenbach *et al.*, 2001).

Adaptive optics systems can also be employed for studying young stars, multiple stars, natal disks and their related inward flows, jets and related outward flows, protoplanetary disks, brown dwarfs, and planets. Roddier *et al.* (1996) detected a binary system consisting of a K7-MO star with an M4 companion that rotates clockwise; they suggested that the system might be surrounded by a warm unresolved disk. The massive star Sanduleak-66°41 in the Large Magellanic Cloud was resolved into 12 components by Heydari and Beuzit (1994). Success in resolving companions of nearby dwarfs has been reported (Beuzit *et al.*, 2001; Kenworthy *et al.*, 2001). Macintosh *et al.* (2001) measured the position of the brown dwarf companion to TWA5 and resolved the primary into an 0.055-arcsec double.

The improved resolution of crowded fields like globular clusters would allow derivation of luminosity functions and spectral types, for the analysis of proper motions in their central areas. Simon *et al.* (1999) have detected 292 stars in the dense Trapezium star cluster of the Orion nebula and resolved pairs to the diffraction limit of a 2.2-m telescope. Optical and near-IR observations have been made of the close Herbig Ae/Be binary star NX Pup (Brandner *et al.*, 1995), associated with the cometary globular cluster I. Schöller *et al.* (1996) estimated the mass and age of both the components and suggested that circumstellar matter around the former could be described by a viscous accretion disk. Line and continuum fluxes as well as equivalent widths were also derived for the massive stars in the Arches cluster (Blum *et al.*, 2001).

Stellar populations in galaxies in the near-IR region provide the peak of the spectral energy distribution for old populations. Bedding, Minniti, *et al.* (1997) observed the Sgr A window at the galactic center of the Milky Way. They produced an IR luminosity function and

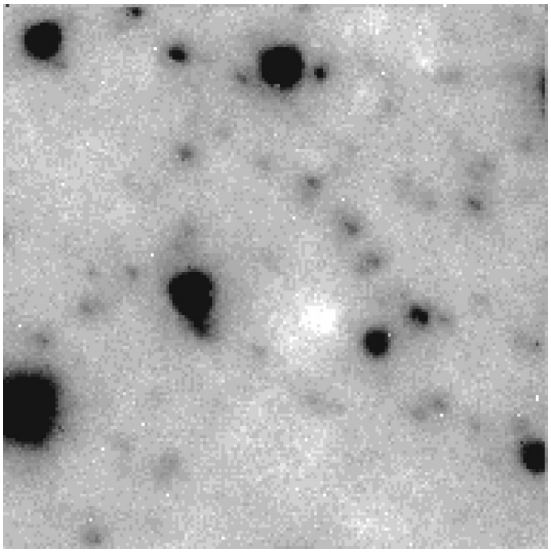

FIG. 20. The Adaptive Optics Near-Infrared System (ADONIS) K′ image of the Sgr A window in the bulge of the Milky Way. The image is 8×8 arcsec. From Bedding, Minniti, *et al.* (1997), courtesy of T. Bedding.

color-magnitude diagram for 70 stars down to $m_v \simeq 19.5$ mag. Figure 20 depicts the ADONIS K′ image of the Sgr A window.

Images have been obtained of several star-forming regions. Messier 16 and the reflection nebula NGC2023 were imaged by Currie *et al.* (1996), revealing small-scale structure in the associated molecular cloud close to the exciting star in Orion (Rouan *et al.*, 1997). Close *et al.* (1997) mapped near-IR polarimetric observations of the reflection nebula R Mon, resolving a faint source 0.69 arcsec away from R Mon, and identified it as a T Tauri star. Monnier *et al.* (1999) found a variety of dust condensations, which include a large scattering plume, and a bow-shaped dust feature, around the red supergiant VY CMa. A bright knot of emission 1 arcsec away from the star was also reported. They argued in favor of the presence of chaotic and violent dust formation processes around the star. Imaging of the protoplanetary nebulae Frosty Leo and the Red Rectangle by Roddier *et al.* (1995) revealed a binary star at their origins.

Imaging of extragalactic objects, particularly the central areas of active galaxies where cold molecular gas and star formation occur, is an important program. From images of the nucleus of NGC1068, Rouan *et al.* (1998) found several components, including an unresolved conspicuous core, an elongated structure, and large- and small-scale spiral structures. Lai *et al.* (1998) recorded images of Markarian 231, a galaxy 160 Mpc away, demonstrating the limits of achievement in terms of morphological structures of distant objects.

Aretxaga *et al.* (1998) reported the unambiguous detection of the host galaxy of a normal radio-quiet quasar at high redshift in the *K* band; detection of emission-line gas within the host galaxies of high-redshift quasistellar objects has been reported, as well (Hutchings *et al.*, 2001). Observations by Ledoux *et al.* (1998) of the broad-absorption-line quasar APM 08279+5255 at $z = 3.87$ show that the object consists of a double source ($\rho = 0.35 \pm 0.02$ arcsec; intensity ratio $= 1.21 \pm 0.25$ in the *H* band). They proposed a gravitational lensing hypothesis based on the uniformity of the quasar spectrum as a function of spatial position. A search for molecular gas in high-redshift normal galaxies in the foreground of the gravitationally lensed quasar Q1208+1011 has also been made (Sams *et al.*, 1996). Adaptive optics imaging of a few low- and intermediate-redshift quasars has been reported recently (Márquez *et al.*, 2001).

High-resolution stellar coronagraphy is of paramount importance in (i) detecting low-mass companions, e.g., both white and brown dwarfs, and dust shells around AGB and post-AGB stars, (ii) observing nebulosities leading to the formation of a planetary system, ejected envelopes, and accretion disks, and (iii) understanding of structure (torus, disk, jets, star-forming regions), and dynamical processes in the environment of active galactic nuclei and quasars. By means of coronagraphic techniques, the environs of a few interesting objects have been explored. They include (i) a very-low-mass companion to the astrometric binary Gliese 105 A (Golimowski *et al.*, 1995), (ii) a warp of the circumstellar disk around the star Beta Pictoris (β Pic; Mouillet *et al.*, 1997), (iii) highly asymmetric features in AG Carina's circumstellar environment (Nota *et al.*, 1992), (iv) the bipolar nebula around the luminous blue variable R127 (Clampin *et al.*, 1993), and (v) the remnant envelopes of star formation around pre-main-sequence stars (Nakajima and Golimowski, 1995).

B. Impact of long-baseline optical interferometry in astrophysics

The main objective of long-baseline optical interferometry is to measure the diameters, distances, masses, and luminosities of stars and to detect the morphological details, such as granulations, oblateness of giant stars, and the image features, i.e., spots and flares on their surfaces. Eclipsing binaries are also good candidates, for they provide information on circumstellar envelopes such as the diameter of the inner envelope, color, symmetry, radial profile, etc. As stated earlier (in Sec. VII.A.2), good spectroscopic and interferometric measurements are required to derive precise stellar masses since they depend on $\sin^3 i$. A small variation in the inclination i implies a large variation in the radial velocities. Most of the orbital calculations that are carried out with speckle observations are not precise enough to provide masses to within better than 10% (Pourbaix, 2000).

The results obtained so far with long-baseline optical interferometers are from stellar angular diameters with implications for emergent fluxes, effective temperatures, luminosities, and structure of stellar atmospheres, as well as for dust and gas envelopes, binary star orbits, stellar masses, relative sizes of emission-line stars and emission regions, stellar rotation, limb darkening, and astrometry (Saha, 1999; Saha and Morel, 2000; Quirrenbach, 2001, and references therein). The angular diam-

eters of more than 50 stars have been measured (DiBenedetto and Rabbia, 1987; Mozurkewich *et al.*, 1991; Dyck *et al.*, 1993; Perin *et al.*, 1999; Nordgren *et al.*, 2000; Kervella *et al.*, 2001; van Belle *et al.*, 2001) with accuracy better than 1% in some cases.

Interesting results that have been obtained using the I2T and the Mark III Interferometer are (i) measuring diameters and effective temperatures of giant stars (Faucherre *et al.*, 1983; DiBenedetto and Rabbia, 1987), (ii) resolving the gas envelope of the Be star Gamma Cassiopeia (γ Cas) in the Hα line (Thom *et al.*, 1986) and structure of circumstellar shells (Bester *et al.*, 1991), and (iii) determining orbits for spectroscopic and eclipsing binaries (Armstrong *et al.*, 1992; Shao and Colavita, 1994).

The GI2T is being used regularly to observe Be stars, luminous blue variables, spectroscopic and eclipsing binaries, wavelength-dependent objects, diameters of bright stars, and circumstellar envelopes. However, the scientific programs are restricted by the low limit of visible magnitude, only 5 (seeing and visibility dependent). The first successful effort to resolve the rotating envelope of the hot star γ Cas came out of this instrument in 1989. Mourard *et al.* (1989) observed this star with a spectral resolution of 1.5 Å centered on Hα. About 300 000 short-exposure images were recorded by a photon-counting camera, CP40 (Blazit, 1986). Each image, which contained $\sim$100 photons, was digitally processed using the correlation technique. The results were averaged to reduce the effect of atmospheric seeing and photon noise, according to the principle of speckle interferometry (Labeyrie, 1970). With the central star as a reference, Mourard *et al.* determined the relative phase of the shell visibility and clearly showed the rotation of the envelope. This result demonstrates the potential of observations that combine spectral and spatial resolution. Through subsequent observations on later dates, Stee *et al.* (1995, 1998) derived the radiative transfer model. Using the data obtained since 1988 with the G12T, Berio, Stee, *et al.* (1999) found evidence of a density pattern rotating slowly prograde in the said star's equatorial disk. Indeed γ Cas has been a favorite target of the GI2T; with further systematic monitoring of multiple emission lines, the formation, structure, and dynamics of other Be stars can be addressed. Other notable results obtained with this instrument include the mean angular diameter and accurate distance estimate of Delta Cephei (δ Cep; Mourard *et al.*, 1997), subtle structures such as jets in the circumstellar environment of the binary system Beta Lyrae (β Lyr; Harmanec *et al.*, 1996), clumpiness in the wind of P Cyg (Vakili *et al.*, 1997), and a prograde one-armed oscillation in the equatorial disk of the Be star Zeta Tauri (ζ Tau; Vakili *et al.*, 1998). With the SUSI instrument, Davis and co-workers (Davis *et al.*, 1998; Davis, Tango, Booth, Thorvaldson, *et al.*, 1999) determined the diameter of Delta Caris Majoris (δ CMa) with an accuracy of $\pm 1.8\%$.

From data obtained at the COAST, aperture-synthesis maps of the double-lined spectroscopic binary Alpha Aurigae (α Aur; Baldwin *et al.*, 1996) have been created

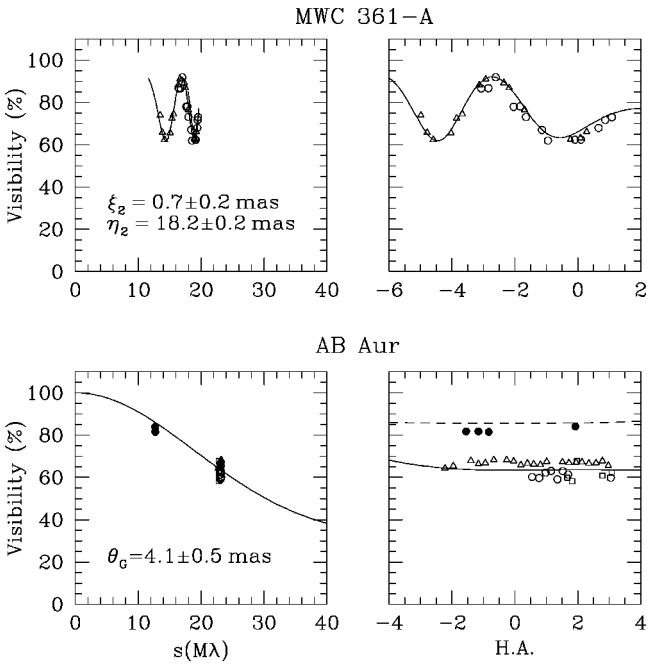

FIG. 21. Examples of *H*-band visibility data and models for two Herbig Ae/Be stars. The data and models are plotted as a function of baseline length (left panels), and hour angle (right panels), which determines the baseline position angles; different symbols correspond to data obtained on different nights. Solid symbols and dashed lines, 21-m baseline data and models; open symbols and solid lines, 38-m baseline data and models. The upper panels show the data and best-fit model for binary detection in MWC 361-A and displays the companion offsets in right ascension (ξ_2) and declination (η_2). The lower panels show the data and best-fit point source plus Gaussian model for AB Aur and displays the Gaussian FWHM (θ_G). From Millan-Gabet *et al.* (2001), courtesy of R. Millan-Gabet.

depicting the milliarcsecond orbital motion of the system over a 15-day interval. Images of α Ori reveal the presence of circularly symmetric data with an unusual flat-topped and limb-darkening profile (Burns *et al.*, 1997). Young *et al.* (2000) have found a strong variation in the apparent symmetry of the brightness distribution as function of wavelength. Variations in the cycle of pulsation of the Mira variable R Leo have been measured by Burns *et al.* (1998).

With IOTA, the angular diameters and effective temperatures were measured for carbon stars (Dyck *et al.*, 1996), Mira variables (van Belle *et al.*, 1996, 1997), cool giant stars (Perrin *et al.*, 1998, 1999), Cepheids (Kervella *et al.*, 2001), and the dust shell of CI Cam (Traub *et al.*, 1998). Millan-Gabet *et al.* (2001) resolved the circumstellar structure of young stars of intermediate mass (Herbig Ae/Be stars) in the near-IR. Figure 21 depicts examples of the H-band visibility data and models for two sources. The lower right panel in Fig. 21 shows the observed lack of visibility variation with baseline rotation, consistent with circumstellar emission from dust that is distributed either in a spherical envelope or in a disk viewed almost face-on.

Figure 22 summarizes the existing set of measurements of near-IR sizes of Herbig Ae/Be sources in the

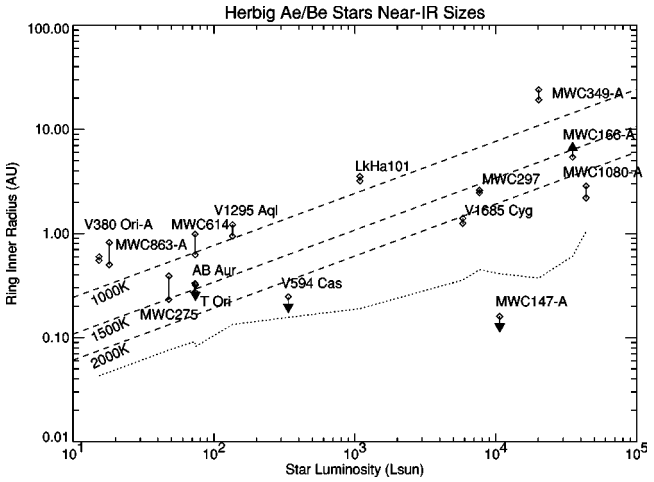

FIG. 22. Measurements of near-IR sizes of Herbig Ae/Be sources. The characteristic sizes plotted were derived from visibility data using a simple model consisting of a central point source plus a uniform ring. The sizes (ring inner radii) are plotted as a function of the luminosity of the central stars, so that they may be compared with the location of optically thin dust at typical sublimation temperatures (dashed lines). The dotted line traces the location of dust at 1500 K under the heating law traditionally assumed, corresponding to the oblique heating of a flat disk surface. It can be seen that the measured sizes are in approximate agreement (given the uncertainties in stellar luminosities and distances) with the first law, but not the second. Figures courtesy of R. Millan-Gabet and J. D. Monnier.

near-IR, using the data from Danchi *et al.* (2001), Millan-Gabet *et al.* (2001), and Tuthill *et al.* (2001). The characteristic sizes are plotted against the luminosities of the central stars, and the plot illustrates the strong correlation observed between the near-IR radii measured and the radii at which optically thin dust would be at typical sublimation temperatures. This observation has motivated in part a revision of disk physics in Herbig Ae/Be systems (Dullemond *et al.*, 2001; Natta *et al.*, 2001). In the new models, the gas inside the dust sublimation radius is assumed to be optically thin so that dust at the inner edge is irradiated frontally and expands, forming a "puffed-up" inner wall. Compared to the traditional model of irradiation of a flat disk, this model results in significantly larger near-IR sources due to the shallower temperature law and naturally explains the observed sizes. Monnier *et al.* (2001) have for the first time combined near-simultaneous observations from two distinct interferometers, IOTA and Keck, in aperture-masking mode. The power of combining the two different resolution regimes for cleanly decomposing the dust shell and underlying stellar components in mass-losing evolved stars is illustrated in Fig. 16 for two such systems (IK Tau and VY CMa).

With the PTI, Malbet *et al.* (1998) have resolved the young stellar object, FU Ori in the near-IR with a projected resolution better than 2 astronomical units (AU). Measurements of diameters and effective temperatures of cool stars and Cepheids have been reported (van Belle *et al.*, 1999; Lane *et al.*, 2000). The visual orbit for the spectroscopic binary Iota Pegasi (ι Peg) with interferometric visibility data has also been derived (Boden *et al.*, 1999). Direct observations of an oblate photosphere of a main-sequence star, Alpha Aquilae (α Aql; van Belle *et al.*, 2001), have been carried out. Ciardi *et al.* (2001) have resolved the stellar disk of Alpha Lyrae (α Lyr) in the near-IR. Employing NPOI, Hummel *et al.* (1998) have determined the orbital parameters of two spectroscopic binaries, Zeta Ursae Majoris (ζ UMa or Mizar A) and Eta Pegasi (η Peg or Matar), and derived masses and luminosities. The limb-darkened diameters have also been measured of late-type giant stars (Hajian *et al.*, 1998; Pauls *et al.*, 1998; Wittkowski *et al.*, 2001) and Cepheid variables (Nordgren *et al.*, 2000).

The observing programs of ISI have been aimed at determining the spatial structure and temporal evolution of dust shells around long-period variables. From the data obtained with this instrument at 11.15 μm, Danchi *et al.* (1994) showed that the radius of dust formation depends on the spectral type of the star. Lopez *et al.* (1997) found a strong dependence on the pulsation phase. Observations were made of NML Cyg, Alpha Scorpii (α Sco), as well as of changes in the dust shell around Mira and IK Tau (Hale *et al.*, 1997; Lopez *et al.*, 1997), and mid-IR molecular absorption features of ammonia and silane of IRC+10216 and VY CMa (Monnier *et al.*, 2000).

Recent observations with two of the VLT telescopes measured the angular diameter of the blue dwarf Alpha Eridani (α Eri), which was found to be 1.92 mas (Glindemann and Paresce, 2001). Subsequently they (i) derived the diameters of a few red dwarf stars, (ii) determined the variable diameters of a few pulsating Cepheid stars, and (iii) measured the core of η Car.

C. Prospects of interferometry

The future of high-resolution optical astronomy lies with the new-generation arrays. Numerous technical challenges for developing these systems will require careful attention. Nevertheless, steady progress has enabled scientists to expand their knowledge of astrophysical processes. With improved technology, interferometric arrays of large telescopes may provide snapshot images at their recombined focus and certainly will yield improved images, spectra of quasar host galaxies, and astrometric detection and characterization of extrasolar planets. The expected limiting magnitude of a hypertelescope imaging array is found numerically to be $8.3m_v$ if 10-cm apertures are used and $20m_v$ for 10-m apertures (Pedretti and Labeyrie, 1999). The limit is expected to increase with the CARLINA array (Labeyrie, 1999b), a 100-element hypertelescope with a diameter of 200 m, shaped like the Arecibo radio telescope in Puerto Rico.

High-precision astrometry also helps in establishing the cosmic distance scale; measurements of proper motion can confirm stars as members of a cluster (known distance), which may elucidate the dynamics of the galaxy. The quest for extrasolar planets (Wallace *et al.*,

1998) is a challenge for narrow-angle astrometry. Very valuable astrometric results from space have already been obtained by the Hipparcos satellite (Perryman, 1998). Hipparcos used phase-shift measurements of the temporal evolution of the photometric level of two stars seen drifting through a grid. The successor of Hipparcos, the Global Astrometric Interferometer for Astrophysics (GAIA; Lindengren and Perryman, 1996), will probably use the same technique with improvements, yielding more accurate results on a larger number of objects. However, only space-borne interferometers will achieve very-high-precision angular measurements.

1. Characterization of extrasolar planets

As many as 76 Jovian-size planets orbiting stars have been identified by the Doppler-Fizeau effect (Mayor and Queloz, 1995; Butler and Marcy, 1996; http://exoplanets.org). For one of them, an atmosphere containing sodium (observed in the sodium resonance doublet at 589.3 nm) has been detected in absorption as the planet transits its parent star HD209458 (Charbonneau *et al.*, 2001). It may also be possible to detect smaller planets by measuring the stellar photocenter motion or "wobble" in the position of a star caused by the transverse component of a companion's motion. A planet orbiting around a star causes a revolution of the star around the center of gravity defined by the two masses. Like galaxy velocity, this periodical short motion has a radial counterpart measurable from the ground by spectrometry. Measurements of the photocenter to detect wobble will require diffraction-limited imaging even for the best possible candidates.

The aim of space interferometers like Darwin and TPF is the discovery and characterization of terrestrial planets around nearby stars (closer than 15 pc) by direct detection (i.e., involving the detection of photons from the planet and not from the star as is done with Doppler-Fizeau effect detection or wobble detection). The difficulties of achieving Earthlike-planet detection come from (i) minimizing scattered light from the parent star and (ii) the presence of exozodiacal light (infrared emission from the dust surrounding the parent star). The interferometric nulling technique will be useful for addressing the first issue.

2. Astrobiology

A knowledge of the chemical composition of any planetary atmosphere gives hints about the likelihood of finding carbon-based life. Lovelock (1965) suggested that the simultaneous presence on Earth of a highly oxidizing gas like O_2 and highly reduced gases like CH_4 and N_2O is the result of the biochemical activity. However, finding spectral signatures of these gases on an extrasolar planet would be very difficult. An alternative life indicator would be ozone (O_3), detectable as an absorption feature at 9.6 μm. On Earth, ozone is photochemically produced from O_2 and, as a component of the stratosphere, is not masked by other gases. Finding ozone would therefore indicate a significant quantity of O_2 that could have been produced by photosynthesis (Léger *et al.*, 1993). Moreover, for a star like the Sun, ozone can be detected 1000 times faster than O_2 at 0.76 μm: estimates made by Angel and Woolf (1997) show that the requirements for planet detection in the visible cannot be met with an 8-m telescope using current technology.

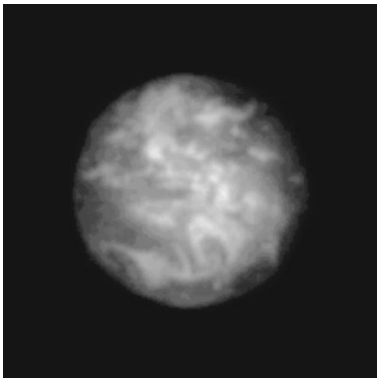

FIG. 23. Simulated image of an Earthlike planet as it might look when detected by a hypertelescope. An image of the Earth was convolved with the spread function from 150 point apertures arrayed in three circles; it was multiplied by the hypertelescope envelope, i.e., the spread function of the subpupils and the contrast was then pushed somewhat to attenuate the diffractive halo. From Labeyrie (2000), courtesy of A. Labeyrie.

3. Long-term perspective

Space-borne interferometry projects for the years spanning 2020 to 2050 already exist; such projects must be regarded as drafts for future instruments. For the post-TPF era, NASA has imagined an enhanced version featuring four 25-m telescopes and a spectrometer with $R \geqslant 1000$. This interferometer would be able to detect from an extra-solar planet lines of gases directly produced by biochemical activity. The next step proposed by NASA is an array of 25 telescopes, of 40 m diameter each, that would yield 25×25-pixel images of an Earthlike planet at 10 pc, revealing its geography and eventually oceans or chlorophyll zones.

A comparable project was proposed by Labeyrie (1999a). It consists of 150 telescopes, of 3 m diameter each, forming an interferometer with a 150-km maximum baseline. Such an instrument equipped with a highly efficient coronagraph would give a 40×40 pixel image of an Earthlike planet at 3 pc. Figure 23 depicts a simulated image of such a detected Earthlike planet (Labeyrie, 1999b). Developing long-baseline interferometry for lunar operation consisting of 20–27 off-axis parabolic segments carried by robotic hexapodes that are movable during an observing run has also been suggested by Arnold *et al.* (1996).

VIII. CONCLUSIONS

Earth-bound astronomical observations are strongly affected by atmospheric turbulence, which severely con-

strains the angular resolution, in the optical domain rarely better than ~0.5 arcsec. Speckle interferometry offers a way around these constraints. A basic understanding of interference phenomena is of paramount importance to other branches of physics and engineering as well. In recent years, a wide variety of applications of speckle patterns have been found in many areas. Though the statistical properties of speckle patterns are complicated, a detailed analysis of such patterns is useful in information processing.

Image processing offers phase retrieval of a degraded image. A second-order moment analysis (power spectrum) provides only the modulus of the object's Fourier transform, whereas a third-order moment (bispectrum) analysis yields the phase, allowing the object to be fully reconstructed. A more recent attempt to go beyond the third order, using a fourth-order moment (trispectrum), shows promise for finding optimal quadratic statistics through the weak gravitational lensing effect (Hu, 2001). This algorithm provides a far more sensitive test than the bispectrum for some possible sources of non-Gaussianity (Kunz *et al.*, 2001); however, its implementation in optical imaging is a difficult computational task. The deconvolution method is another approach to imaging, which covers methods spanning from simple linear deconvolution algorithms to complex nonlinear algorithms.

In astronomy, the field of research that has probably benefited the most from high-angular-resolution techniques using single telescopes, and that will still benefit in the future, is undoubtedly the origin and evolution of stellar systems. This evolution starts with star formation, including multiplicity, and ends with the mass-loss process, which recycles heavier elements into the interstellar medium. Large-scale star formation provides a link between small-scale and large-scale processes. Stellar chemical evolution or nucleosynthesis that is a result of star formation activity further influences the evolutionary process. High-resolution observations are fruitful for the detection of protoplanetary disks and possibly planets (either astrometrically, through their influence on the disk, or directly). The technique is also being applied to studies of starburst and Seyfert galaxies, active galactic nuclei, and quasars. Studies of the morphology of stellar atmospheres, the circumstellar environment of novae or supernovae, young planetary nebulae, long-period variables, the rapid variability of active galactic nuclei, etc., are also essential.

In spite of our limited ability to retrieve fully diffraction-limited images of the objects we observe, AO systems are now available to users of large telescopes. Adaptive optics observations have contributed to the study of the solar system and enhanced the results of space-borne instruments, for example, monitoring of the volcanic activity on Io or of the cloud cover on Neptune, the detection of Neptune's dark satellites and arcs, and the ongoing discovery of companions to asteroids; the same AO techniques are now greatly contributing to the study of the Sun itself (Antoshkin *et al.*, 2000; Rimmele, 2000). Combining AO systems with speckle imaging will offer improvements not accessible by either approach alone (Dayton *et al.*, 1998). By the end of the next decade (post 2010), observations using AO systems on a new-generation telescope like OWL will revolutionize the mapping of ultrafaint objects like extrasolar planets and blazars, which exhibit the most rapid and the largest-amplitude variations of all active galactic nuclei (Ulrich *et al.*, 1997). Certain aspects of galactic evolution like chemical evolution in the Virgo cluster of galaxies can be studied as well.

A host of basic problems require a very high angular resolution for their solution. Among others, an important fundamental problem that can be addressed with interferometry and AO is the origin and evolution of galaxies. The upcoming large facilities with phased arrays of multiple 8–10-m subapertures will provide larger collecting areas and higher spatial resolution than the current interferometers. These instruments fitted with complete AO systems should be able to provide imaging and morphological information on faint extragalactic sources such as galactic centers in the young universe, deep fields, and host galaxies. Measurement of such objects may be made feasible by instruments with fairly complete (u,v) coverage and a large field of view. The derivation of motions and parallaxes of galactic centers seems to be feasible with phase reference techniques. The origin of faint structures close to nonobscured central sources can also be studied in detail with interferometric polarization measurements.

The capabilities of the proposed large arrays offer a revolution in the study of compact astronomical sources from the solar neighborhood to cosmological distances. The list of possible uses ranges from detecting other planetary systems to imaging the black-hole-driven central engines of quasars and active galaxies; gamma-ray bursters may be another candidate, along with the recording of spectra to derive velocity and to determine black hole masses as a function of redshift. At the beginning of the present millennium, several such arrays will be in operation both on the ground and in space. Space-borne interferometers are currently planned to detect planets either astrometrically (SIM) or directly (TPF). Projects like *Darwin* and other ambitious imaging instruments may also come to fruition.

ACKNOWLEDGMENTS

The author expresses his gratitude to A. Labeyrie, S. T. Ridgway, and P. A. Wehinger for comments on the review, and to V. Coudé du Foresto, P. R. Lawson, and S. Morel for valuable communications. Thanks are also due to T. R. Bedding, A. Boccaletti, P. M. Hinz, R. Millan-Gabet, J. D. Monnier, R. Osterbart, and M. Wittkowski for providing images and figures, and granting permission for their reproduction, as well as to H. Bradt and P. Hickson for reading the manuscript. The services rendered by V. Chinnappan, K. R. Subramanian, and B. A. Varghese are gratefully acknowledged.

REFERENCES

Ables, J. G., 1974, Astron. Astrophys., Suppl. Ser. **15**, 383.

Aime, C., 2000, J. Opt. A, Pure Appl. Opt. **2**, 411.

Akeson, R., M. Swain, and M. Colavita, 2000, in *Interferometry in Optical Astronomy*, Proceedings of SPIE No. 4006, edited by P. J. Lena and A. Quirrenbach (SPIE, Bellingham), p. 321.

Anderson, J. A., 1920, Astrophys. J. **51**, 263.

Angel, J. R. P., 1994, Nature (London) **368**, 203.

Angel, J. R. P., 2001, Nature (London) **409**, 427.

Angel, J. R. P., A. Cheng, and N. Woolf, 1986, Nature (London) **322**, 341.

Angel, J. R., and N. J. Woolf, 1997, Astrophys. J. **475**, 373.

Antoshkin, L. V., *et al.*, 2000, in *Adaptive Optical Systems Technology*, Proceedings of SPIE No. 4007, edited by P. L. Wizinowich (SPIE, Bellingham), p. 232.

Aretxaga, I., D. Mignant, J. Melnick, R. Terlevich, and B. Boyle, 1998, Mon. Not. R. Astron. Soc. **298**, L13.

Armstrong, J., *et al.*, 1998, Astrophys. J. **496**, 550.

Armstrong, J. T., C. A. Hummel, and D. Mozurkewich, 1992, in *High-Resolution Imaging by Interferometry II*, ESO Conference and Workshop Proceedings No. 39, edited by J. M. Beckers and F. Merkle (ESO, Garching, Germany), p. 673.

Arnold, L., A. Labeyrie, and D. Mourard, 1996, Adv. Space Res. **18**, 1148.

Ayers, G. R., and J. C. Dainty, 1988, Opt. Lett. **13**, 547.

Baba, N., S. Kuwamura, N. Miura, and Y. Norimoto, 1994, Astrophys. J. Lett. **431**, L111.

Baba, N., S. Kuwamura, and Y. Norimoto, 1994, Appl. Opt. **33**, 6662.

Baba, N., H. Tomita, and N. Miura, 1994, Appl. Opt. **33**, 4428.

Babcock, H. W., 1953, Publ. Astron. Soc. Pac. **65**, 229.

Babcock, H. W., 1990, Science **249**, 253.

Bagnuolo, W. G., Jr., B. D. Mason, D. J. Barry, W. I. Hartkopf, and H. A. McAlister, 1992, Astron. J. **103**, 1399.

Baldwin, J., R. Boysen, C. Haniff, P. Lawson, C. Mackay, J. Rogers, D. St-Jacques, P. Warner, D. Wilson, and J. Young, 1998, in *Astronomical Interferometry*, Proceedings of SPIE No. 3350, edited by R. D. Reasenberg (SPIE, Bellingham), p. 736.

Baldwin, J., *et al.*, 1996, Astron. Astrophys. **306**, L13.

Baldwin, J., R. Tubbs, G. Cox, C. Mackay, R. Wilson, and M. Andersen, 2001, Astron. Astrophys. **368**, L1.

Baldwin, J. E., C. A. Haniff, C. D. Mackay, and P. J. Warner, 1986, Nature (London) **320**, 595.

Baldwin, J. E., and P. J. Warner, 1978, Mon. Not. R. Astron. Soc. **182**, 411.

Balick, B., 1987, Astron. J. **94**, 671.

Barlow, M. J., B. L. Morgan, C. Standley, and H. Vine, 1986, Mon. Not. R. Astron. Soc. **223**, 151.

Barnaby, D., E. Spillar, J. Christou, and J. Drummond, 2000, Astron. J. **119**, 378.

Bates, R., and M. McDonnell, 1986, *Image Restoration and Reconstruction* (Clarendon, Oxford).

Beckers, J. M., 1982, Opt. Acta **29**, 361.

Bedding, T., A. Zijlstra, O. Von der Lühe, J. Robertson, R. Marson, J. Barton, and B. Carter, 1997, Mon. Not. R. Astron. Soc. **286**, 957.

Bedding, T. R., D. Minniti, F. Courbin, and B. Sams, 1997, Astron. Astrophys. **326**, 936.

Beichman, C., 1998, in *Astronomical Interferometry*, Proceedings of SPIE No. 3350, edited by R. D. Reasenberg (SPIE, Bellingham), p. 719.

Benson, J., D. Mozurkewich, and S. Jefferies, 1998, in *Astronomical Interferometry*, Proceedings of SPIE No. 3350, edited by R. D. Reasenberg (SPIE, Bellingham), p. 493.

Berger, J., P. Haguenauer, P. Kern, K. Perraut, F. Malbet, I. Schanen, M. Severi, R. Millan-Gabet, and W. Traub, 2001, Astron. Astrophys. **376**, L31.

Berio, P., D. Mourard, D. Bonneau, O. Chesneau, P. Stee, N. Thureau, and F. Vakili, 1999, J. Opt. Soc. Am. A **16**, 872.

Berio, P., P. Stee, F. Vakili, D. Mourard, D. Bonneau, O. Chesneau, N. Thureau, D. Le Mignant, and R. Hirata, 1999, Astron. Astrophys. **345**, 203.

Bester, M., W. C. Danchi, C. G. Degiacomi, and C. H. Townes, 1991, Astrophys. J. Lett. **367**, L27.

Beuzit, J., *et al.*, 2001, e-print astro-ph/0106277.

Blazit, A., 1986, in *Image Detection and Quality*, Proceedings of SPIE No. 702, edited by L. F. Guyot (SPIE, Bellingham), p. 259.

Blöcker, T., Y. Balega, K.-H. Hofmann, and G. Weigelt, 2001, Astron. Astrophys. **369**, 142.

Blum, R., D. Schaerer, A. Pasquali, M. Heydari-Malayeri, P. Conti, and W. Schmutz, 2001, Astron. J. (in press).

Boccaletti, A., 2001, private communication.

Boccaletti, A., C. Moutou, D. Mouillet, A. Lagrange, and J. Augereau, 2001, Astron. Astrophys. **367**, 371.

Boccaletti, A., P. Riaud, C. Moutou, and A. Labeyrie, 2000, Icarus **145**, 628.

Boden, A., *et al.*, 1999, Astrophys. J. **515**, 356.

Bonneau, D., and R. Foy, 1980, Astron. Astrophys. **92**, L1.

Bonneau, D., and A. Labeyrie, 1973, Astrophys. J. **181**, L1.

Born, M., and E. Wolf, 1984, *Principles of Optics* (Pergamon, New York).

Bouvier, J., F. Rigaut, and D. Nadeau, 1997, Astron. Astrophys. **323**, 139.

Bracewell, R. N., 1978, Nature (London) **274**, 780.

Brandl, B., B. J. Sams, F. Bertoldi, A. Eckart, R. Genzel, S. Drapatz, R. Hofmann, M. Lowe, and A. Quirrenbach, 1996, Astrophys. J. **466**, 254.

Brandner, W., J. Bouvier, E. Grebel, E. Tessier, D. de Winter, and J. L. Beuzit, 1995, Astron. Astrophys. **298**, 816.

Briggs, D. S., 1995, Ph.D. thesis (New Mexico Institute of Mining and Technology).

Bruns, D., T. Barnett, and D. Sandler, 1997, in *Optical Telescopes of Today and Tomorrow*, Proceedings of SPIE No. 2871, edited by A. L. Ardeberg (SPIE, Bellingham), p. 890.

Burge, J. H., B. Cuerdem, and J. R. P. Angel, 2000, in *UV, Optical, and IR Telescopes and Instrumentation*, Proceedings of SPIE No. 4013, edited by J. B. Breckinridge and P. Jakobsen (SPIE, Bellingham), p. 640.

Burns, D., *et al.*, 1997, Mon. Not. R. Astron. Soc. **290**, L11.

Burns, D., *et al.*, 1998, Mon. Not. R. Astron. Soc. **297**, 467.

Butler, R., and G. Marcy, 1996, Astrophys. J. Lett. **464**, L153.

Cadot, O., Y. Couder, A. Daerr, S. Douady, and A. Tsinocber, 1997, Phys. Rev. E **56**, 427.

Callados, M., and M. Vàzquez, 1987, Astron. Astrophys. **180**, 223.

Carleton, N., *et al.*, 1994, in *Amplitude and Intensity Spatial Interferometry II*, Proceedings of SPIE No. 2200, edited by J. B. Breckinridge (SPIE, Bellingham), p. 152.

Cassinelli, J., J. Mathis, and B. Savage, 1981, Science **212**, 1497.

Charbonneau, D., T. Brown, R. Noyes, and R. Gilfiland, 2001, Astrophys. J. **568**, 377.

Ciardi, D., G. van Belle, R. Akeson, R. Thompson, E. A. Lada, and S. Howell, 2001, Astrophys. J. (in press).

Clampin, M., J. Croker, F. Paresce, and M. Rafal, 1988, Rev. Sci. Instrum. **59**, 1269.
Clampin, M., A. Nota, D. A. Golimowski, C. Leitherer, and A. Ferrari, 1993, Astrophys. J. Lett. **410**, L35.
Close, L., F. Roddier, J. Hora, J. Graves, M. Northcott, C. Roddier, W. Hoffman, A. Doyal, G. Fazio, and L. Deutsch, 1997, Astrophys. J. **489**, 210.
Colavita, M., 1999, Publ. Astron. Soc. Pac. **111**, 111.
Colavita, M., *et al.*, 1998, in *Astronomical Interferometry*, Proceedings of SPIE No. 3350, edited by R. D. Reasenberg (SPIE, Bellingham), p. 776.
Colavita, M., *et al.*, 1999, Astrophys. J. **510**, 505.
Conan, J.-M., L. M. Mugnier, T. Fusco, V. Michau, and G. Rousset, 1998, Appl. Opt. **37**, 4614.
Conan, R., A. Ziad, J. Borgnino, F. Martin, and A. Tokovinin, 2000, in *Interferometry in Optical Astronomy*, Proceedings of SPIE No. 4006, edited by P. J. Lena and A. Quirrenbach (SPIE, Bellingham), p. 963.
Cooper, D., D. Bui, R. Bailey, L. Kozlowski, and K. Vural, 1993, in *Infrared Detectors and Instrumentation*, Proceedings of SPIE No. 1946, edited by A. M. Fowler (SPIE, Bellingham), p. 170.
Cornwell, T. J., and P. N. Wilkinson, 1981, Mon. Not. R. Astron. Soc. **196**, 1067.
Coudé du Foresto, V., G. Perrin, and M. Boccas, 1995, Astron. Astrophys. **293**, 278.
Coulman, C. E., 1974, Sol. Phys. **34**, 491.
Coulman, C. E., 1985, Annu. Rev. Astron. Astrophys. **23**, 19.
Currie, D., K. Kissel, E. Shaya, P. Avizonis, D. Dowling, and D. Bonnacini, 1996, ESO Messenger **86**, 31.
Danchi, W. C., M. Bester, C. Degiacomi, I. Greenhill, and C. Townes, 1994, Astron. J. **107**, 1469.
Danchi, W. C., P. G. Tuthill, and J. D. Monnier, 2001, Astrophys. J. **562**, 440.
Dantowitz, R., S. Teare, and M. Kozubal, 2000, Astron. J. **119**, 2455.
Davidge, T. J., F. Rigaut, R. Doyon, and D. Crampton, 1997, Astron. J. **113**, 2094.
Davidge, T. J., D. A. Simons, F. Rigaut, R. Doyon, E. E. Becklin, and D. Crampton, 1997, Astron. J. **114**, 2586.
Davis, J., and W. J. Tango, 1996, Publ. Astron. Soc. Pac. **108**, 456.
Davis, J., W. Tango, A. Booth, and J. O'Byrne, 1998, in *Astronomical Interferometry*, Proceedings of SPIE No. 3350, edited by R. D. Reasenberg (SPIE, Bellingham), p. 726.
Davis, J., W. Tango, A. Booth, T. ten Brummelaar, R. Minard, and S. Owens, 1999, Mon. Not. R. Astron. Soc. **303**, 773.
Davis, J., W. J. Tango, A. J. Booth, E. D. Thorvaldson, and J. Giovannis, 1999, Mon. Not. R. Astron. Soc. **303**, 783.
Dayton, D., S. Sandven, J. Gonglewski, S. Rogers, S. McDermott, and S. Browne, 1998, in *Adaptive Optical System Technologies*, Proceedings of SPIE No. 3353, edited by D. Bonaccini and R. K. Tyson (SPIE, Bellingham), p. 139.
Dejonghe, J., L. Arnold, O. Lardière, J.-P Berger, C. Cazalé, S. Dutertre, D. Kohler, and D. Vernet, 1998, in *Advanced Technology Optical/IR Telescopes VI*, Proceedings of SPIE No. 3352, edited by L. M. Stepp (SPIE, Bellingham), p. 603.
Denker, C., 1998, Sol. Phys. **81**, 108.
Derie, F., M. Ferrai, E. Brunetto, M. Duchateau, R. Amestica, and P. Aniol, 2000, in *Interferometry in Optical Astronomy*, Proceedings of SPIE No. 4006, edited by P. J. Lena and A. Quirrenbach (SPIE, Bellingham), p. 99.
DiBenedetto, G. P., and Y. Rabbia, 1987, Astron. Astrophys. **188**, 114.
Diericks, P., and R. Gilmozzi, 1999, in *Proceedings of Bäckaskog Workshop on Extremely Large Telescopes*, ESO Conference and Workshop Proceedings No. 57, edited by T. Andersen, A. Ardeberg, and R. Gilmozzi (ESO, Garching, Germany), p. 43.
Drummond, J., A. Eckart, and E. Hege, 1988, Icarus **73**, 1.
Dullemond, C. P., C. Dominick, and A. Natta, 2001, Astrophys. J. **560**, 957.
Dyck, H., J. Benson, and S. Ridgway, 1993, Publ. Astron. Soc. Pac. **105**, 610.
Dyck, H., G. van Belle, and J. Benson, 1996, Astron. J. **112**, 294.
Ebstein, S., N. P. Carleton, and C. Papaliolios, 1989, Astrophys. J. **336**, 103.
Eke, V., 2001, Mon. Not. R. Astron. Soc. **320**, 106.
Elias, N. M., 2001, Astrophys. J. **549**, 647.
Falcke, H., K. Davidson, K.-H. Hofmann, and G. Weigelt, 1996, Astron. Astrophys. **306**, L17.
Faucherre, M., D. Bonneau, L. Koechlin, and F. Vakili, 1983, Astron. Astrophys. **120**, 263.
Fienup, J. R., 1978, Opt. Lett. **3**, 27.
Fischer, O., B. Stecklum, and C. Leinert, 1998, Astron. Astrophys. **334**, 969.
Fizeau, H., 1868, C. R. Hebd. Seances Acad. Sci. **66**, 934.
Fomalont, E. B., and M. C. H. Wright, 1974, in *Galactic and Extragalactic Radio Astronomy*, edited by G. L. Verschuur and K. I. Kellerman (Springer, New York), p. 256.
Foy, R., D. Bonneau, and A. Blazit, 1985, Astron. Astrophys. **149**, L13.
Foy, R., and A. Labeyrie, 1985, Astron. Astrophys. **152**, L29.
Fried, D. L., 1966, J. Opt. Soc. Am. **56**, 1372.
Fugate, R., *et al.*, 1994, J. Opt. Soc. Am. A **11**, 310.
Gauger, A., Y. Y. Balega, P. Irrgang, R. Osterbart, and G. Weigelt, 1999, Astron. Astrophys. **346**, 505.
Gay, J., and D. Mekarnia, 1988, in *High-Resolution Imaging by Interferometry*, ESO Conference and Workshop Proceedings No. 29, edited by J. M. Beckers and F. Merkle (ESO, Garching, Germany), p. 811.
Gerchberg, R. W., and W. O. Saxton, 1972, Optik (Stuttgart) **35**, 237.
Gies, R., B. Mason, W. Bagnuolo, M. Haula, W. I. Hartkopf, H. McAlister, M. Thaller, W. McKibben, and L. Penny, 1997, Astrophys. J. Lett. **475**, L49.
Glindemann, A., 1997, Publ. Astron. Soc. Pac. **109**, 682.
Glindemann, A., R. G. Lane, and J. C. Dainty, 1991, in *Proceedings of the 9th International Conference on Digital Signal Processing*, Florence, edited by V. Cappellini and A. G. Constantinides (Elsevier, Amsterdam), p. 59.
Glindemann, A., and F. Paresce, 2001, http://www.eso.org/outreach.
Golimowski, D. A., T. Nakajima, S. R. Kulkarni, and B. R. Oppenheimer, 1995, Astrophys. J. Lett. **444**, L101.
Gonsalves, S. A., 1982, Opt. Eng. (Bellingham) **21**, 829.
Goodman, J. W., 1975, in *Laser Speckle and Related Phenomena*, edited by J. C. Dainty, Topics in Applied Physics No. 9 (Springer, Berlin), p. 9.
Goodman, J. W., 1985, *Statistical Optics* (Wiley, New York).
Gorham, P. W., 1998, in *Astronomical Interferometry*, Proceedings of SPIE No. 3350, edited by R. D. Reasenberg (SPIE, Bellingham), p. 116.

Gorham, P., W. Folkner, and G. Blackwood, 1999, in *Working on the Fringe: Optical and IR Interferometry from Ground and Space*, ASP Conference Proceedings No. 194, edited by S. Unwin and R. Stachnik (ASP, Provo), p. 359.
Greenwood, D. P., 1977, J. Opt. Soc. Am. **67**, 390.
Grieger, F., F. Fleischman, and G. Weigelt, 1988, in *High-Resolution Imaging by Interferometry*, ESO Conference and Workshop Proceedings No. 29, edited by J. M. Beckers and F. Merkle (ESO, Garching, Germany), p. 225.
Haguenauer, P., M. Sevei, I. Schanen-Duport, K. Rousselet-Perraut, J. Berger, Y. Duchéne, M. Lacolle, P. Kern, F. Melbet, and P. Benech, 2000, in *Interferometry in Optical Astronomy*, Proceedings of SPIE No. 4006, edited by P. J. Lena and A. Quirrenbach (SPIE, Bellingham) p. 1107.
Hajian, A., *et al.*, 1998, Astrophys. J. **496**, 484.
Hale, D., M. Bester, W. Danchi, W. Fitelson, S. Hoss, E. Lipman, J. Monnier, P. Tuthill, and C. Townes, 2000, Astrophys. J. **537**, 998.
Hale, D., *et al.*, 1997, Astrophys. J. **490**, 826.
Hanbury Brown, R., 1974, *The Intensity Interferometer: Its Applications to Astronomy* (Taylor & Francis, London).
Hanbury Brown, R., R. C. Jennison, and M. K. Das Gupta, 1952, Nature (London) **170**, 1061.
Hanbury Brown, R., and R. Twiss, 1958, Proc. R. Soc. London, Ser. A **248**, 222.
Haniff, C., M. Scholz, and P. Tuthill, 1995, Mon. Not. R. Astron. Soc. **276**, 640.
Harmanec, P., *et al.*, 1996, Astron. Astrophys. **312**, 879.
Hartkopf, W. I., H. A. McAlister, and B. D. Mason, 1997, "Third Catalog of Interferometric Measurements of Binary Stars" CHARA Contrib. No. 4, http://ad.usno.navy.mil/wds/int3.html
Hartley, M., B. McInnes, and F. Smith, 1981, Q. J. R. Astron. Soc. **22**, 272.
Harvey, J. W., 1972, Nature (London) **235**, 90.
Harvey, J. W., and J. B. Breckinridge, 1973, Astrophys. J. **182**, L137.
Hawley, S. A., and J. S. Miller, 1977, Astrophys. J. **212**, 94.
Hege, E., E. Hubbard, P. Strittmatter, and S. Worden, 1981, Astrophys. J. **248**, 1.
Hestroffer, D., 1997, Astron. Astrophys. **327**, 199.
Heydari, M., and J. Beuzit, 1994, Astron. Astrophys. **287**, L17.
Hickson, P., 2001, private communication.
Hill, J. M., 2000, in *Telescope Structures, Enclosures, Controls, Assembly/Integration/Validation, and Commissioning*, Proceedings of SPIE No. 4004, edited by T. A. Sebring and T. Andersen (SPIE, Bellingham), p. 36.
Hinz, P., R. Angel, W. Hoffmann, D. Mccarthy, P. Mcguire, M. Cheselka, J. Hora, and N. Woolf, 1998, Nature (London) **395**, 251.
Hinz, P., W. Hoffmann, and J. Hora, 2001, Astrophys. J. Lett. (in press).
The Hipparcos and Tycho Catalogue, 1997, ESA SP-1200.
Hofmann, K.-H., W. Seggewiss, and G. Weigelt, 1995, Astron. Astrophys. **300**, 403.
Högbom, J., 1974, Astron. Astrophys., Suppl. Ser. **15**, 417.
Hu, W., 2001, e-print astro-ph/0105117.
Hummel, C., D. Mozurkevich, J. Armstrong, A. Hajian, N. Elias, and D. Hutter, 1998, Astron. J. **116**, 2536.
Hutchings, J., D. Crampton, S. Morris, D. Durand, and E. Steinbring, 1999, Astron. J. **117**, 1109.
Hutchings, J., D. Crampton, S. Morris, and E. Steinbring, 1998, Publ. Astron. Soc. Pac. **110**, 374.
Hutchings, J., S. Morris, and D. Crampton, 2001, Astron. J. **121**, 80.
Ishimaru, A., 1978, *Wave Propagation and Scattering in Random Media* (Academic, New York).
Jefferies, S., and J. Christou, 1993, Astrophys. J. **415**, 862.
Jennison, R. C., 1958, Mon. Not. R. Astron. Soc. **118**, 276.
Karovska, M., L. Koechlin, P. Nisenson, C. Papaliolios, and C. Standley, 1989, Astrophys. J. **340**, 435.
Kenworthy, M., *et al.*, 2001, Astrophys. J. Lett. **554**, 67.
Kervella, P., V. Coudé du Foresto, G. Perrin, M. Schöller, W. Traub, and M. Lacasse, 2001, Astron. Astrophys. **367**, 876.
Knox, K., and B. Thompson, 1974, Astrophys. J. **193**, L45.
Koechlin, L., P. R. Lawson, D. Mourard, A. Blazit, D. Bonneau, F. Morand, P. Stee, I. Tallon-Bosc, and F. Vakili, 1996, Appl. Opt. **35**, 3002.
Kolmogorov, A., 1941a, in *Turbulence*, edited by S. K. Friedlander and L. Topper (Wiley-Interscience, New York), p. 151.
Kolmogorov, A., 1941b, in *Turbulence*, edited by S. K. Friedlander and L. Topper (Wiley-Interscience, New York), p. 156.
Kolmogorov, A., 1941c, in *Turbulence*, edited by S. K. Friedlander and L. Topper (Wiley-Interscience, New York), p. 159.
Korff, D., 1973, J. Opt. Soc. Am. **63**, 971.
Kunz, M., A. Banday, P. Castro, P. Ferreira, and K. Górski, 2001, Astrophys. J. Lett. **563**, 99.
Labeyrie, A., 1970, Astron. Astrophys. **6**, 85.
Labeyrie, A., 1975, Astrophys. J. Lett. **196**, L71.
Labeyrie, A., 1995, Astron. Astrophys. **298**, 544.
Labeyrie, A., 1996, Astron. Astrophys., Suppl. Ser. **118**, 517.
Labeyrie, A., 1998, in *Astronomical Interferometry*, Proceedings of SPIE No. 3350, edited by R. D. Reasenberg (SPIE, Bellingham), p. 960.
Labeyrie, A., 1999a, in *Working on the Fringe: Optical and IR Interferometry from Ground and Space*, ASP Conference Proceedings No. 194, edited by S. Unwin and R. Stachnik (ASP, Provo) p. 350.
Labeyrie, A., 1999b, Science **285**, 1864.
Labeyrie, A., 2000, private communication.
Labeyrie, A., 2001, private communication.
Labeyrie, A., L. Koechlin, D. Bonneau, A. Blazit, and R. Foy, 1977, Astrophys. J. Lett. **218**, L75.
Labeyrie, A., G. Lamaitre, and L. Koechlin, 1986, in *Advanced Optical Technology Telescopes III*, Proceedings of SPIE No. 628, edited by L. D. Barr (SPIE, Bellingham), p. 323.
Labeyrie, A., G. Schumacher, M. Dugué, C. Thom, P. Bourlon, F. Foy, D. Bonneau, and R. Foy, 1986, Astron. Astrophys. **162**, 359.
Lai, O., D. Rouan, F. Rigaut, R. Arsenault, and E. Gendron, 1998, Astron. Astrophys. **334**, 783.
Lai, O., D. Rouan, F. Rigaut, F. Doyon, and F. Lacombe, 1999, Astron. Astrophys. **351**, 834.
Lane, B., M. Kuchner, A. Boden, M. Crooch-Eakman, and S. R. Kulkarni, 2000, Nature (London) **407**, 485.
Lannes, A., E. Anterrieu, and K. Bouyoucef, 1994, J. Mod. Opt. **41**, 1537.
Lawson, P. R., 1994, Publ. Astron. Soc. Pac. **106**, 917.
Lawson, P. R., 1995, J. Opt. Soc. Am. A **12**, 366.
Lawson, P., J. Baldwin, P. Warner, R. Boysen, C. Haniff, J. Rogers, D. Saint-Jacques, D. Wilson, and J. Young, 1998, in *Astronomical Interferometry*, Proceedings of SPIE No. 3350, edited by R. D. Reasenberg (SPIE, Bellingham), p. 753.
Lawson, P., M. Colavita, P. Dumont, and B. Lane, 2000, in *Interferometry in Optical Astronomy*, Proceedings of SPIE No. 4006, edited by P. J. Lena and A. Quirrenbach (SPIE, Bellingham), p. 397.

Ledoux, C., B. Théodore, P. Petitjean, M. N. Bremer, G. F. Lewis, R. A. Ibata, M. J. Irwin, and E. J. Totten, 1998, Astron. Astrophys. **339**, L77.
Lee, J., B. Bigelow, D. Walker, A. Doel, and R. Bingham, 2000, Publ. Astron. Soc. Pac. **112**, 97.
Lefèvre, H. C., 1980, Electron. Lett. **16**, 778.
Léger, A., M. Pirre, and F. J. Marceau, 1993, Astron. Astrophys. **277**, 309.
Liang, J., D. R. Williams, and D. T. Miller, 1997, J. Opt. Soc. Am. A **14**, 2884.
Lindengren, L., and M. A. C. Perryman, 1996, Astron. Astrophys., Suppl. Ser. **116**, 579.
Linfield, R., and P. Gorham, 1999, in *Working on the Fringe: Optical and IR Interferometry from Ground and Space*, ASP Conference Proceedings No. 194, edited by S. Unwin and R. Stachnik (ASP, Provo), p. 224.
Lloyd-Hart, M., 2000, Publ. Astron. Soc. Pac. **112**, 264.
Lloyd-Hart, M., J. R. Angel, T. Groesbeck, T. Martinez, B. Jacobsen, B. McLeod, D. McCarthy, E. Hooper, E. Hege, and D. Sandler, 1998, Astrophys. J. **493**, 950.
Lipman, E., M. Bester, W. Danchi, and C. Townes, 1998, in *Astronomical Interferometry*, Proceedings of SPIE No. 3350, edited by R. D. Reasenberg (SPIE, Bellingham), p. 933.
Liu, Y. C., and A. W. Lohmann, 1973, Opt. Commun. **8**, 372.
Lohmann, A., G. Weigelt, and B. Wirnitzer, 1983, Appl. Opt. **22**, 4028.
Lopez, B., 1991, "Last Mission at La Silla, April 19–May 8, on the Measure of the Wavefront Evolution Velocity," ESO Internal Report.
Lopez, B., *et al.*, 1997, Astrophys. J. **488**, 807.
Lovelock, J. E., 1965, Nature (London) **207**, 568.
Lucy, L., 1974, Astron. J. **79**, 745.
Lynds, C., S. Worden, and J. Harvey, 1976, Astrophys. J. **207**, 174.
Machida, Y., *et al.*, 1998, in *Astronomical Interferometry*, Proceedings of SPIE No. 3350, edited by R. D. Reasenberg (SPIE, Bellingham), p. 202.
Macintosh, B., C. B. Max, B. Zuckerman, E. Becklin, D. Kaisler, P. Lowrence, A. Weinberger, J. Christou, G. Schneider, and S. Acton, 2001, *Young Stars near Earth: Progress and Prospects*, edited by R. Jayawardhare and J. Green.
Mackay, C. D., R. N. Tubbs, R. Bell, D. Burt, P. Jerram, and I. Moody, 2001, in *Sensors and Camera Systems for Scientific, Industrial, and Digital Photography Applications II*, Proceedings of SPIE No. 4306, edited by M. M. Blouke, J. Canosa, and N. Sampat (SPIE, Bellingham), p. 289.
Magain, P., F. Courbin, and S. Sohy, 1998, Astrophys. J. **494**, 472.
Malbet, F., *et al.*, 1998, Astrophys. J. Lett. **507**, L149.
Marco, O., T. Encrenaz, and E. Gendron, 1997, Planet. Space Sci. **46**, 547.
Márquez, I., P. Petitjean, B. Théodore, M. Bremer, G. Monnet, and J. Beuzit, 2001, Astron. Astrophys. **371**, 97.
Masciadri, E., J. Vernin, and P. Bougeault, 1999, Astron. Astrophys., Suppl. Ser. **137**, 203.
Mason, B. D., 1996, Astron. J. **112**, 2260.
Mason, B., C. Martin, W. I. Hartkopf, D. Barry, M. Germain, G. Douglass, C. Worley, G. Wycoff, T. ten Brummelaar, and O. Franz, 1999, Astron. J. **117**, 1890.
Mayor, M., and D. Queloz, 1995, Nature (London) **378**, 355.
McAlister, H., W. Bagnuolo, T. ten Brummelaar, W. I. Hartkopf, M. Shure, L. Sturmann, N. Turner, and S. Ridgway, 1998, in *Astronomical Interferometry*, Proceedings of SPIE No. 3350, edited by R. D. Reasenberg (SPIE, Bellingham), p. 947.
Mendel, L., and E. Wolf, 1995, *Optical Coherence and Quantum Optics* (Cambridge University, Cambridge).
Mennesson, B., J.-M. Mariotti, V. Coudé du Foresto, G. Perrin, S. Ridgway, C. Ruilier, W. Traub, M. Lacasse, and G. Mazé, 1999, Astron. Astrophys. **346**, 181.
Men'shchikov, A., and T. Henning, 1997, Astron. Astrophys. **318**, 879.
Michelson, A. A., 1891, Nature (London) **45**, 160.
Michelson, A. A., and F. G. Pease, 1921, Astrophys. J. **53**, 249.
Millan-Gabet, R., P. Schloerb, and W. Traub, 2001, Astrophys. J. **546**, 358.
Monnier, J., W. Danchi, D. Hale, P. Tuthill, and C. Townes, 2000, Astrophys. J. **543**, 868.
Monnier, J., *et al.*, 2001, Bull. Am. Astron. Soc. **33**, 63.02.
Monnier, J., P. Tuthill, B. Lopez, P. Cruzalébes, W. Danchi, C. Haniff, 1999, Astrophys. J. **512**, 351.
Morel, S., 2000, private communication.
Morel, S., and L. Koechlin, 1998, in *Astronomical Interferometry*, Proceedings of SPIE No. 3350, edited by R. D. Reasenberg (SPIE, Bellingham), p. 257.
Morel, S., W. Traub, J. Bregman, R. Mah, and C. Wilson, 2000, in *Interferometry in Optical Astronomy*, Proceedings of SPIE No. 4006, edited by P. J. Lena and A. Quirrenbach (SPIE, Bellingham), p. 506.
Mouillet, D., J. D. Larwood, J. C. Papaloizou, and A. M. Lagrange, 1997, Mon. Not. R. Astron. Soc. **292**, 896.
Mourard, D., D. Bonneau, L. Koechlin, A. Labeyrie, F. Morand, P. Stee, I. Tallon-Bosc, and F. Vakili, 1997, Astron. Astrophys. **317**, 789.
Mourard, D., I. Bosc, A. Labeyrie, L. Koechlin, and S. Saha, 1989, Nature (London) **342**, 520.
Mozurkewich, D., K. Johnston, R. Simon, D. Hutter, M. Colavita, M. Shao, and X. Pan, 1991, Astron. J. **101**, 2207.
Nakajima, T., 1994, Astrophys. J. **425**, 348.
Nakajima, T., and D. Golimowski, 1995, Astron. J. **109**, 1181.
Natta, A., T. Prusti, R. Neri, D. Wooden, and V. Grinin, 2001, Astron. Astrophys. **371**, 186.
Nelkin, M., 2000, Am. J. Phys. **68**, 310.
Nisenson, P., and C. Papaliolios, 1999, Astrophys. J. Lett. **518**, L29.
Nisenson, P., C. Papaliolios, M. Karovska, and R. Noyes, 1987, Astrophys. J. Lett. **320**, L15.
Nordgren, T., J. Armstrong, M. Gierman, R. Hindsley, A. Hajian, J. Sudol, and C. Hummel, 2000, Astrophys. J. **543**, 972.
Northcott, M. J., G. R. Ayers, and J. C. Dainty, 1988, J. Opt. Soc. Am. A **5**, 986.
Nota, A., C. Leitherer, M. Clampin, P. Greenfield, and D. A. Golimowski, 1992, Astron. J. **398**, 621.
Nulsen, P., P. Wood, P. Gillingham, M. Bessel, M. Dopita, and C. McCowage, 1990, Astrophys. J. **358**, 266.
Osterbart, R., Y. Balega, G. Weigelt, and N. Langer, 1997, in *Planetary Nebulae*, Proceedings of the 180th Symposium of the International Astronomical Union, Groningen, The Netherlands, edited by H. J. Habing and H. J. G. L. M. Lamers (Kluwer, Dordrecht, The Netherlands), p. 362.
Padilla, C., V. Karlov, L. Matson, K. Soosaar, and T. ten Brummelaar, 1998, in *Astronomical Interferometry*, Proceedings of SPIE No. 3350, edited by R. D. Reasenberg (SPIE, Bellingham), p. 1045.

Papaliolios, C., M. Karovska, L. Koechlin, P. Nisenson, C. Standley, and S. Heathcote, 1989, Nature (London) **338**, 565.

Papaliolios, C., P. Nisenson, and S. Ebstein, 1985, Appl. Opt. **24**, 287.

Pauls, T., D. Mozurkewich, J. Armstrong, C. Hummel, J. Benson, and A. Hajian, 1998, in *Astronomical Interferometry*, Proceedings of SPIE No. 3350, edited by R. D. Reasenberg (SPIE, Bellingham), p. 467.

Paxman, R., T. Schulz, and J. Fienup, 1992, J. Opt. Soc. Am. A **9**, 1072.

Pedretti, E., and A. Labeyrie, 1999, Astron. Astrophys., Suppl. Ser. **137**, 543.

Pedretti, E., A. Labeyrie, L. Arnold, N. Thureau, O. Lardiére, A. Boccaletti, and P. Riaud, 2000, Astron. Astrophys., Suppl. Ser. **147**, 285.

Pehlemann, E., K.-H. Hofmann, and G. Weigelt, 1992, Astron. Astrophys. **256**, 701.

Penny, A., A. Léger, J. Mariotti, C. Schalinski, C. Eiora, R. Laurance, and M. Fridlund, 1998, in *Astronomical Interferometry*, Proceedings of SPIE No. 3350, edited by R. D. Reasenberg (SPIE, Bellingham), p. 666.

Perrin, G., 1997, Astron. Astrophys., Suppl. Ser. **121**, 553.

Perrin, G., V. Coudé du Foresto, S. Ridgway, J.-M. Marrioti, W. Traub, N. Carleton, M. Lacasse, 1998, Astron. Astrophys. **331**, 619.

Perrin, G., V. Coudé du Foresto, S. Ridgway, B. Mennesson, C. Ruilier, J.-M. Marrioti, W. Traub, and M. Lacasse, 1999, Astron. Astrophys. **345**, 221.

Perryman, M. A. C., 1998, Nature (London) **340**, 111.

Poulet, F., and B. Sicardy, 1996, Bull. Am. Astron. Soc. **28**, 1124.

Pourbaix, D., 2000, Astron. Astrophys., Suppl. Ser. **145**, 215.

Prieur, J., E. Oblak, P. Lampens, M. Kurpinska-Winiarska, E. Aristidi, L. Koechlin, and G. Ruymaekers, 2001, Astron. Astrophys. **367**, 865.

Puetter, R., and A. Yahil, 1999, in *Astronomical Data Analysis Software and Systems VIII*, edited by D. Mehringer, R. Plante, and D. Roberts.

Quirrenbach, A., 2001, Annu. Rev. Astron. Astrophys. **39**, 353.

Quirrenbach, A., D. Mozurkewich, D. Buscher, C. Hummel, and J. Armstrong, 1996, Astron. Astrophys. **312**, 160.

Quirrenbach, A., J. Roberts, K. Fidkowski, W. de Vries, and W. van Breugel, 2001, Astrophys. J. **556**, 108.

Rabbia, Y., D. Mekarnia, and J. Gay, 1990, in *Infrared Technology XVI*, Proceedings of SPIE No. 1341, edited by I. J. Spiro (SPIE, Bellingham), p. 172.

Racine, R., 1984, in *Very Large Telescopes, Their Instrumentation and Programs*, IAU Colloquium No. 79, edited by M.-H. Ulrich and K. Kjar (ESO, Garching, Germany), p. 235.

Racine, R., G. Herriot, and R. McClure, 1996, in *Adaptive Optics*, ESO Conference and Workshop Proceedings No. 54, edited by M. Cullum (ESO, Garching, Germany), p. 35.

Ragazzoni, R., and D. Bonaccini, 1996, in *Adaptive Optics*, ESO Conference and Workshop Proceedings No. 54, edited by M. Cullum (ESO, Garching, Germany), p. 17.

Ragazzoni, R., E. Marchetti, and G. Valente, 2000, Nature (London) **403**, 54.

Reinheimer, T., and G. Weigelt, 1987, Astron. Astrophys. **176**, L17.

Richardson, W. H., 1972, J. Opt. Soc. Am. **62**, 55.

Ridgway, S. T., and F. Roddier, 2000, in *Interferometry in Optical Astronomy*, Proceedings of SPIE No. 4006, edited by P. J. Lena and A. Quirrenbach (SPIE, Bellingham), p. 940.

Rimmele, T. R., 2000, in *Interferometry in Optical Astronomy*, Proceedings of SPIE No. 4006, edited by P. J. Lena and A. Quirrenbach (SPIE, Bellingham), p. 218.

Robbe, S., B. Sorrente, F. Cassaing, Y. Rabbia, and G. Rousset, 1997, Astron. Astrophys., Suppl. Ser. **125**, 367.

Robertson, N. A., 2000, Class. Quantum Grav. **17**, 19.

Roddier, F., 1981, Prog. Opt. **XIX**, 281.

Roddier, F., 1988, Phys. Rep. **170**, 97.

Roddier, F., 1999, Ed., *Adaptive Optics in Astronomy* (Cambridge University, Cambridge).

Roddier, C., and F. Roddier, 1988, in *Diffraction-Limited Imaging with Very Large Telescopes*, Proceedings of the *NATO Advanced Study Institute*, Cargèse, Corsica, edited by D. M. Alloin and J.-M. Mariotti (Kluwer, Dordrecht, The Netherlands), p. 221.

Roddier, C., F. Roddier, M. J. Northcott, J. E. Graves, and K. Jim, 1996, Astrophys. J. **463**, 326.

Roddier, F., C. Roddier, A. Brahic, C. Dumas, J. Graves, M. Northcott, and T. Owen, 1997, Planet. Space Sci. **45**, 1031.

Roddier, F., C. Roddier, J. E. Graves, and M. J. Northcott, 1995, Astrophys. J. **443**, 249.

Roggemann, M. C., B. M. Welsh, and R. Q. Fugate, 1997, Rev. Mod. Phys. **69**, 437.

Rouan, D., D. Field, J.-L. Lemaire, O. Lai, G. P. Forëts, E. Falgarone, and J.-M. Deltorn, 1997, Mon. Not. R. Astron. Soc. **284**, 395.

Rouan, D., P. Riaud, A. Boccaletti, Y. Clénet, and A. Labeyrie, 2000, Publ. Astron. Soc. Pac. **112**, 1479.

Rouan, D., F. Rigaut, D. Alloin, R. Doyon, O. Lai, D. Crampton, E. Gendron, and R. Arsenault, 1998, Astron. Astrophys. **339**, 687.

Rousselet-Perraut, K., F. Vakili, and D. Mourard, 1996, Opt. Eng. (Bellingham) **35**, 2943.

Rousset, G., 1999, in *Adaptive Optics in Astronomy*, edited by F. Roddier (Cambridge University, Cambridge), p. 91.

Rousset, G., J. C. Fontanella, P. Kem, P. Gigan, F. Rigaut, P. Léna, P. Boyer, P. Jagourel, J. P. Gaffard, and F. Merkle, 1990, Astron. Astrophys. **230**, L29.

Ryan, S., and P. Wood, 1995, Publ.-Astron. Soc. Aust. **12**, 89.

Saha, S. K., 1999, Bull. Astron. Soc. India **27**, 443.

Saha, S. K., and V. Chinnappan, 1999, Bull. Astron. Soc. India **27**, 327.

Saha, S. K., and D. Maitra, 2001, Indian J. Phys., B **75B**, 391.

Saha, S. K., and S. Morel, 2000, Bull. Astron. Soc. India **28**, 175.

Saha, S. K., R. Rajamohan, P. Vivekananda Rao, G. Som Sunder, R. Swaminathan, and B. Lokanadham, 1997, Bull. Astron. Soc. India **25**, 563.

Saha, S. K., R. Sridharan, and K. Sankarasubramanian, 1999, "Speckle image reconstruction of binary stars," presented at the 19th Meeting of the Astronomical Society of India, Bangalore.

Saha, S. K., and P. Venkatakrishnan, 1997, Bull. Astron. Soc. India **25**, 329.

Sams, B. J., K. Schuster, and B. Brandl, 1996, Astrophys. J. **459**, 491.

Sato, K., *et al.*, 1998, in *Astronomical Interferometry*, Proceedings of SPIE No. 3350, edited by R. D. Reasenberg (SPIE, Bellingham), p. 212.
Schertl, D., K.-H. Hofmann, W. Seggewiss, and G. Weigelt, 1996, Astron. Astrophys. **302**, 327.
Schöller, M., W. Brandner, T. Lehmann, G. Weigelt, and H. Zinnecker, 1996, Astron. Astrophys. **315**, 445.
Seldin, J., and R. Paxman, 1994, in *Image Reconstruction and Restoration*, Proceedings of SPIE No. 2302, edited by T. J. Schulz and D. L. Snyder (SPIE, Bellingham), p. 268.
Seldin, J., R. Paxman, and C. Keller, 1996, in *Missions to the Sun*, Proceedings of SPIE No. 2804, edited by D. M. Rust (SPIE, Bellingham), p. 166.
Serabyn, E., 2000, in *Interferometry in Optical Astronomy*, Proceedings of SPIE No. 4006, edited by P. J. Lena and A. Quirrenbach (SPIE, Bellingham), p. 328.
Shannon, C. J., 1949, Proc. IRE **37**, 10.
Shao, M., and M. M. Colavita, 1992, Astron. Astrophys. **262**, 353.
Shao, M., and M. M. Colavita, 1994, in *Very High Angular Resolution Imaging*, Proceedings of the 158th Symposium of the International Astronomical Union, Sydney, Australia, edited by J. G. Robertson and W. J. Tango (Kluwer, Dordrecht, The Netherlands), p. 413.
Shao, M., *et al.*, 1988, Astron. Astrophys. **193**, 357.
Shao, M., and D. Staelin, 1977, J. Opt. Soc. Am. **67**, 81.
Sicardy, B., F. Roddier, C. Roddier, E. Perozzi, J. E. Graves, O. Guyon, and M. J. Northcott, 1999, Nature (London) **400**, 731.
Simon, M., L. Close, and T. Beck, 1999, Astron. J. **117**, 1375.
Stee, P., F. de Araújo, F. Vakili, D. Mourard, I. Arnold, D. Bonneau, F. Morand, and I. Tallon-Bosc, 1995, Astron. Astrophys. **300**, 219.
Stee, P., F. Vakili, D. Bonneau, and D. Mourard, 1998, Astron. Astrophys. **332**, 268.
Tallon, M., R. Foy, and A. Blazit, 1988, in *Very Large Telescopes and Their Instrumentation*, ESO Conference and Workshop Proceedings No. 30, edited by M.-H. Ulrich (Kluwer, Dordrecht, The Netherlands), p. 743.
Tango, W. J., and R. Q. Twiss, 1980, Prog. Opt. **17**, 239.
Tatarski, V. I., 1967, *Wave Propagation in a Turbulent Medium* (Dover, New York).
Tatarski, V. I., 1993, J. Opt. Soc. Am. A **56**, 1380.
Taylor, G. L., 1921, in *Turbulence*, edited by S. K. Friedlander and L. Topper, 1961 (Wiley-Interscience, New York), p. 1.
Thom, C., P. Granes, and F. Vakili, 1986, Astron. Astrophys. **165**, L13.
Thompson, L. A., and C. S. Gardner, 1988, Nature (London) **328**, 229.
Timothy, J. G., 1993, in *Photoelectronic Detection and Imaging: Technology and Applications '93*, Proceedings of SPIE No. 1982, edited by L. Zhou (SPIE, Bellingham), p. 4.
Torres, G., R. Stefanik, and D. Latham, 1997, Astrophys. J. **485**, 167.
Townes, C. H., M. Bester, W. Danchi, D. Hale, J. Monnier, E. Lipman, A. Everett, P. Tuthill, M. Johnson, and D. Walters, 1998, in *Astronomical Interferometry*, Proceedings of SPIE No. 3350, edited by R. D. Reasenberg (SPIE, Bellingham), p. 908.
Traub, W. A., 1986, Appl. Opt. **25**, 528.
Traub, W. A., 2000, in *Principles of Long Baseline Interferometry*, Course Notes from the 1999 Michelson Summer School, Pasadena, edited by P. R. Lawson (JPL, Pasadena), p. 31. Also available at http://sim.jpl.nasa.gov/library/coursenotes/chapt3.pdf
Traub, W. A., *et al.*, 2000, in *Interferometry in Optical Astronomy*, Proceedings of SPIE No. 4006, edited by P. J. Lena and A. Quirrenbach (SPIE, Bellingham), p. 715.
Traub, W. A., R. Millan-Gabet, and M. Garcia, 1998, Bull. Am. Astron. Soc. **30**, 52.06.
Troxel, S. E., B. M. Welsh, and M. C. Roggemann, 1994, J. Opt. Soc. Am. A **11**, 2100.
Tuthill, P., C. Haniff, and J. Baldwin, 1997, Mon. Not. R. Astron. Soc. **285**, 529.
Tuthill, P., C. Haniff, and J. Baldwin, 1999, Mon. Not. R. Astron. Soc. **306**, 353.
Tuthill, P. G., J. D. Monnier, and W. C. Danchi, 1999, Nature (London) **398**, 487.
Tuthill, P. G., J. D. Monnier, and W. C. Danchi, 2001, Nature (London) **409**, 1012.
Tuthill, P. G., J. D. Monnier, W. C. Danchi, and E. H. Wishnow, 2000, Publ. Astron. Soc. Pac. **116**, 2536.
Ulrich, M., L. Maraschi, and C. Urry, 1997, Annu. Rev. Astron. Astrophys. **35**, 445.
Unwin, S., S. Turyshev, and M. Shao, 1998, in *Astronomical Interferometry*, Proceedings of SPIE No. 3350, edited by R. D. Reasenberg (SPIE, Bellingham), p. 551.
Vakili, F., D. Mourard, D. Bonneau, F. Morand, and P. Stee, 1997, Astron. Astrophys. **323**, 183.
Vakili, F., D. Mourard, P. Stee, D. Bonneau, P. Berio, O. Chesneau, N. Thureau, F. Morand, A. Labeyrie, and I. Tallon-Bosc, 1998, Astron. Astrophys. **335**, 261.
van Belle, G., D. Ciardi, R. Thompson, R. Akeson, and E. A. Lada, 2001, Astrophys. J. (in press).
van Belle, G., H. Dyck, J. Benson, and M. Lacasse, 1996, Astron. J. **112**, 2147.
van Belle, G., H. Dyck, R. Thomson, J. Benson, and S. Kannappan, 1997, Astron. J. **114**, 2150.
van Belle, G., *et al.*, 1999, Astron. J. **117**, 521.
Von der Lühe, O., 1984, J. Opt. Soc. Am. A **1**, 510.
Walkup, J. F., and J. W. Goodman, 1973, J. Opt. Soc. Am. **63**, 399.
Wallace, J., *et al.*, 1998, in *Astronomical Interferometry*, Proceedings of SPIE No. 3350, edited by R. D. Reasenberg (SPIE, Bellingham), p. 864.
Wehinger, P. A., 2001, private communication.
Weigelt, G., 1977, Opt. Commun. **21**, 55.
Weigelt, G., and G. Bair, 1985, Astron. Astrophys. **150**, L18.
Weigelt, G., Y. Balega, T. Blöcker, A. Fleischer, R. Osterbart, and J. Winters, 1998, Astron. Astrophys. **333**, L51.
Weigelt, G., Y. Balega, K.-H. Hofmann, and M. Scholz, 1996, Astron. Astrophys. **316**, L21.
Weigelt, G., and J. Ebersberger, 1986, Astron. Astrophys. **163**, L5.
Weinberger, A., G. Neugebauer, and K. Matthews, 1999, Astron. J. **117**, 2748.
Wilken, V., C. R. de Boer, C. Denker, and F. Kneer, 1997, Astron. Astrophys. **325**, 819.
Wilson, R., J. Baldwin, D. Busher, and P. Warner, 1992, Mon. Not. R. Astron. Soc. **257**, 369.
Wittkowski, M., Y. Balega, T. Beckert, W. Duschi, K. Hofmann, and G. Weigelt, 1998, Astron. Astrophys. **329**, L45.
Wittkowski, M., Y. Balega, K. Hofmann, and G. Weigelt, 1999, Mitt. Astron. Ges. **15**, 83.

Wittkowski, M., C. Hummel, K. Johnston, D. Mozurkewich, A. Hajian, and N. White, 2001, Astron. Astrophys. **377**, 981.
Wittkowski, M., N. Langer, and G. Weigelt, 1998, Astron. Astrophys. **340**, L39.
Wood, P., M. Bessel, and M. Dopita, 1986, Astrophys. J. **311**, 632.
Wood, P., P. Nulsen, P. Gillingham, M. Bessel, M. Dopita, and C. McCowage, 1989, Astrophys. J. **339**, 1073.
Worden, S. P., C. R. Lynds, and J. W. Harvey, 1976, J. Opt. Soc. Am. **66**, 1243.
Wyngaard, J. C., Y. Izumi, and S. A. Collins, 1971, J. Opt. Soc. Am. **60**, 1495.
Young, A. T., 1974, Astrophys. J. **189**, 587.
Young, J., *et al.*, 2000, Mon. Not. R. Astron. Soc. **315**, 635.
Zago, L., 1995, Ph.D. thesis (Ecole Polytechnique Fédérale de Lausanne). Also available at http://www.eso.org/gen-fac/pubs/astclim/papers/lz-thesis/h_thesis.html